



**POLITECNICO**  
MILANO 1863

SCUOLA DI INGEGNERIA INDUSTRIALE  
E DELL'INFORMAZIONE

# Metastable Ti FCC films produced by PLD: synthesis and characterization

TESI DI LAUREA MAGISTRALE IN  
MATERIALS ENGINEERING AND NANOTECHNOLOGY-  
INGEGNERIA DEI MATERIALI E DELLE NANOTECNOLOGIE

Author: **Pierluigi Marrazzo**

Student ID: 993536

Advisor: Prof. David Dellasega

Co-advisor: Dr. Andrea Macrelli

Academic Year: 2022-23



## Abstract

Titanium is a transition metal that finds lots of application both as a bulk material and as a thin film due to the excellent and unique properties such as high specific strength, corrosion resistance and intrinsic biocompatibility. It is a polymorphic material that exhibits both a temperature and pressure induced phase variation with relative different properties. At room temperature and atmospheric pressure, the stable crystal structure is the HCP one, but at higher temperature and pressure the stable phases are respectively the BCC and the  $\omega$ . Recent studies revealed also the presence of a face-centered cubic (FCC) titanium phase, not predicted by the usual temperature-pressure phase diagram. This phase is characterized by different mechanical and electronic properties such as conductivity, magnetic susceptibility, and specific heat. The following phase has been attempted to be stabilized both in bulk and in thin films. The metastable FCC phase results to be formed in presence of strong plastic deformation for bulk titanium, while for thin films it has been observed to be stable thanks to high energetic deposition techniques (HiPIMS, vacuum arc discharge) and only until a limited thickness. In both cases, some studies also report the stabilizing effect of impurities, such as oxygen, hydrogen, and nitrogen.

In this context, the aim of this thesis is to produce thin films of metastable FCC phase by Pulsed Laser Deposition (PLD) at different working conditions of initial background pressure, fluence rate, deposition time, gas atmosphere. Thanks to SEM, EDXS, Raman, XRD (both in grazing and  $\theta/2\theta$  configuration) it has been possible to study the effect of PLD, thickness of the sample, impurities (oxygen) in the films, and gas (Ar) on the stabilization of non-thermodynamic phase. The PLD, thanks to its both pulsed and high energetic regime, seems to stabilize with a certain reproducibility a mixture of FCC and HCP phase until 2  $\mu\text{m}$ . The effect of the gas (1 Pa of Ar) results to be relevant only at small fluences ( $2\text{J}/\text{cm}^2$ ), because slows the energetic regime of PLD and tends to form the thermodynamic favoured HCP crystal structure. In this experiment, the strong affinity of Ti to interact with impurities, known as getter function, plays an important role in the decrease of the initial background pressure, in the formation of films with high quantity of oxygen, greater than 30%, and in the relative stabilization of the FCC phase. Furthermore, the high quantity of oxygen leads also to an expansion of the lattice cell with respect to that calculated from theoretical results, obtaining a value of 4.22-4.30  $\text{\AA}$ . The very last part of this work is devoted to the analysis of Ti-O vibrations in the film by Raman.

**Key-words:** PLD, titanium FCC, oxygen stabilizing effect, getter, metastable.

## Abstract in italiano

Il titanio è un metallo di transizione, esso trova numerosi impieghi sia in forma bulk, sia in forma di film sottili, per via delle notevoli proprietà meccaniche, di resistenza a corrosione e un'intrinseca biocompatibilità. Esso è un materiale polimorfico che presenta transizione di fase indotta sia dalla temperatura, sia dalla pressione. In condizioni standard la struttura cristallina stabile è HCP, mentre ad alte temperature e pressioni sono favorite rispettivamente la fase BCC e quella  $\omega$ . Tuttavia, oltre alle fasi ormai note, recenti studi hanno evidenziato la presenza di una fase metastabile FCC non prevista dal consueto diagramma di stato temperatura-pressione. La nuova fase presenta proprietà meccaniche ed elettroniche, come la conducibilità, la suscettibilità magnetica ed il calore specifico, diverse dalle consuete fasi del titanio.

La stabilizzazione della seguente fase è stata oggetto di studi sia per il materiale bulk sia in forma di rivestimenti sottili. Nel primo caso la formazione della fase metastabile è stata riscontrata per via di un'elevata deformazione plastica del materiale, che generando difetti, permette una variazione della struttura cristallina rispetto a quella di equilibrio. Nel secondo caso la fase FCC risulta essere stabilizzata grazie a deposizioni PVD caratterizzate da un elevato regime energetico e da una dinamica di fuori equilibrio, ma solo fino ad un certo spessore. In entrambi i casi, alcuni studi riportano anche l'effetto stabilizzante di impurezze, quali H, N, O.

In questo contesto, l'obiettivo di questa tesi è di produrre nanofilms caratterizzati da una fase metastabile FCC mediante uso di Deposizione Laser Pulsata (PLD) a diverse condizioni operative di pressione iniziale in camera, tempo di deposizione, fluensa e atmosfera di gas (Ar). Una caratterizzazione al SEM, EDXS, Raman ed XRD (in configurazione grazing e  $\theta/2\theta$ ) ha permesso di studiare l'effetto della PLD, dello spessore dei campioni, delle impurezze nel film (solo ossigeno è presente nel nostro caso) e del gas nella stabilizzazione della seguente fase. La PLD, grazie al suo regime sia pulsato che altamente energetico, sembra stabilizzare con una certa riproducibilità una contemporanea presenza di fase FCC ed HCP fino ad uno spessore di  $2\mu\text{m}$ . L'effetto del gas (1Pa di Ar) risulta essere rilevante solo a basse fluense ( $2\text{J}/\text{cm}^2$ ), poiché rallentando il regime energetico della PLD la trasforma in una tecnica di deposizione più tendente all'equilibrio, favorendo così la presenza di una singola fase HCP. Durante le deposizioni, la forte tendenza del titanio ad interagire con le impurezze, svolge un ruolo di rilievo nella diminuzione della pressione iniziale in camera, nella formazione di un film ad alto tasso di ossigeno (la concentrazione atomica di ossigeno nel film è maggiore del 30%) e nella relativa stabilizzazione della fase desiderata.

L'elevata presenza di ossigeno comporta anche un aumento delle dimensioni della cella cristallina rispetto a quanto calcolato in letterature da calcoli teorici. Il valore calcolato in questo lavoro presenta con una certa riproducibilità un valore compreso tra 4.22-4.30 Å.

L'ultima parte di questo lavoro è stata dedicata ad analizzare le vibrazioni Ti-O al Raman.

**Parole chiave:** PLD, titanio FCC, ossigeno, getter, metastabile





# Contents

<b>Abstract</b> .....	<b>i</b>
<b>Abstract in italiano</b> .....	<b>iii</b>
<b>Contents</b> .....	<b>vii</b>
<b>1 Introduction</b> .....	<b>3</b>
1.1. Titanium: phase, properties and applications.....	3
1.2. Metastable phases .....	7
1.2.1. Metastable phases in titanium films .....	7
1.2.2. Metastable phases in bulk titanium .....	10
1.3. Titanium getter function .....	13
1.3.1. TSP .....	13
1.3.2. NEG .....	16
1.4. Aim of the thesis.....	19
<b>2 Materials and methods</b> .....	<b>21</b>
2.1. Pulsed laser deposition (PLD) .....	21
2.1.1. PLD set-up .....	24
2.2. SEM and EDXS .....	25
2.2.1. Scanning electron microscope (SEM) .....	25
2.2.2. EDXS.....	27
2.3. Raman .....	29
2.4. XRD .....	31
2.5. Annealing .....	33
<b>3 Synthesis and morphological and chemical characterization</b> .....	<b>35</b>
3.1. Titanium getter function and cleaning.....	36
3.2. Morphological and thickness analysis .....	43
3.2.1. Fluence threshold .....	43
3.2.2. Thickness profile analysis .....	45
3.2.3. Morphology of Ti films.....	46
3.3. Chemical and compositional analysis.....	50
3.3.1. Influence of process parameters on oxygen concentration .....	50
<b>4 Investigation on crystal phase stability</b> .....	<b>54</b>

4.1.	GIXRD analysis.....	54
4.1.1.	Peak assignment .....	54
4.1.2.	Influence of process parameters on the stabilization of FCC phase..	60
4.1.3.	Influence of process parameters in the cell dimensions .....	62
4.1.4.	Williamson-Hall analysis.....	65
4.2.	XRD in $\theta/2\theta$ configuration analysis .....	69
4.2.1.	Influence of Ti/O ratio on stability of FCC phase .....	71
4.2.2.	Influence of parameters in the cell dimension and Scherrer .....	72
4.3.	Crystal structure investigation post annealing .....	74
4.4.	Raman analysis .....	75
<b>5</b>	<b>Conclusions and future developments .....</b>	<b>79</b>
	<b>Bibliography .....</b>	<b>83</b>
	<b>List of Figures .....</b>	<b>91</b>
	<b>List of Tables .....</b>	<b>95</b>
	<b>Acknowledgments.....</b>	<b>99</b>





# 1 Introduction

## 1.1. Titanium: phase, properties and applications

Titanium is a transition metal of the four group that is employed in all the sector thanks to its excellent and unique properties.

The high specific strength, excellent corrosion resistance in harsh conditions and intrinsic biocompatibility make it very attractive for aerospace sector, chemical industry, biomedical applications and also the leisure sector. At higher temperatures the specific strength of titanium alloys is particularly appealing, but the main drawback is the extreme tendency of Ti to interact with impurities, such as oxygen and hydrogen; in particular the favoured interaction with oxygen can cause oxidation at a temperature relatively low, around 500°C; on the other hand the tendency to interact with H can cause embrittlement of the alloy, that's why welding operation of Ti alloys occurs in vacuum or in an inert atmosphere. [1]

Titanium (Ti) and the metals of the four group (Zr, Hf) share the same arrangement of the outer electrons, contributing significantly to the similarities observed in certain chemical and physical characteristics such as crystal structure and metallurgical properties. Ti, as the other elements of its group previously cited, is an allotropic element: it doesn't present a unique thermodynamic phase, but different ones according to the specific range of temperature and pressure; it exhibits both a temperature and pressure induced polymorphism. [2]

Since the properties of the material strongly depend on composition and on microstructure, the existence of different crystal structures is of crucial importance because they allow a large variety of applications for Ti alloys [1].

At room temperature and atmospheric pressure Ti shows an HCP crystal structure called  $\alpha$ -titanium. On raising the temperature above  $882 \pm 2^\circ\text{C}$  while keeping the pressure constant, the HCP structure shift to a BCC one, called  $\beta$  titanium.[1]

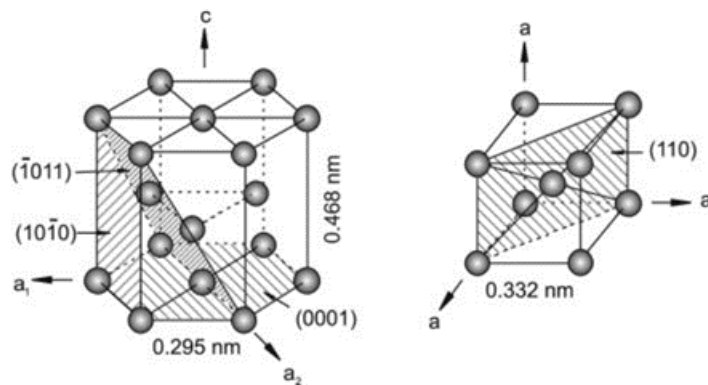


Figure 1.1: Titanium's HCP  $\alpha$  phase (left) and BCC  $\beta$  phase (right). Highlighted the most densely packed planes and directions. [1]

$\alpha$  alloys possess an HCP unit cell, characterized by a denser and anisotropic structure, that is translated in anisotropic mechanical behaviour. It stands out for excellent corrosion resistance, reduced ductility, high creep resistance, while high specific strength ranks second. In view of this properties, these specific alloys find application mostly in chemical and process engineering industry, where excellent corrosion behaviour and deformability are required. [1]

The temperature at which occurs the allotropic transformation is called  $\beta$ -transus, during which the hexagonal cell distorts leading to a slight contraction leading to the formation of a cubic structure. [1]

Depending on the composition alloy is possible to tune properly the  $\beta$ -transus transformation through the addition of opportune alloying elements. Those can be divided in neutrals,  $\beta$ -stabilizers and  $\alpha$ -stabilizers. The former are elements that have a negligible influence on transition temperature. The  $\beta$  elements are elements that stabilize  $\beta$  phase decreasing the transition temperature, such as V, Mo, Nb [3]. The  $\alpha$  ones are elements that extend the stability of  $\alpha$  phase at higher temperatures. Among those ones, aluminium is the most used in the case of titanium but is important also to highlight the  $\alpha$  stabilizing effect of some impurities that have a strong affinity with titanium like oxygen, nitrogen, and carbon. [1]

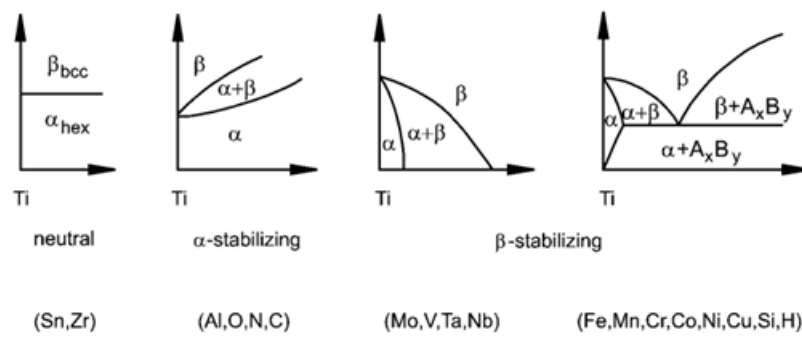


Figure 1.2: influence of alloying elements on phase diagrams [1]

In general, depending on the percentage of  $\alpha$  and  $\beta$  phase, it is possible to divide the Ti alloys in three categories:  $\alpha$  alloys,  $\beta$  alloys and  $\alpha+\beta$  alloys.  $\alpha$  alloys comprise commercially pure titanium and alloys that have only  $\alpha$ -stabilizers.  $\alpha+\beta$  alloys have a fraction of  $\beta$  stabilizers, resulting in 10-30% of the  $\beta$  phase in their microstructure. Metastable  $\beta$  alloys contain even greater amount of  $\beta$  stabilizers, allowing the retention of the beta phase through rapid cooling, but they eventually decompose into the  $\alpha+\beta$  alloys with aging [3]. Table 1.1 shows the different properties of different titanium phases.

Table 1.1: properties of  $\alpha$ ,  $\alpha+\beta$ ,  $\beta$  Ti alloys [1].

	$\alpha$	$\alpha+\beta$	$\beta$
<b>Density</b>	+	+	-
<b>Strength</b>	-	+	++
<b>Ductility</b>	-/+	+	+/-
<b>Fracture toughness</b>	+	-/+	+/-
<b>Creep strength</b>	+	+/-	-
<b>Corrosion behaviour</b>	++	+	+/-
<b>Oxidation behaviour</b>	++	+/-	-
<b>Weldability</b>	+	+/-	-
<b>Cold formability</b>	--	-	-/+

$\beta$  alloys, even if have remained a small segment of the industry, due to the cubic crystal structure, offer the highest strength-to-weight ratios of all titanium alloys and an enhanced ductility respect the  $\alpha$  one. They are characterized by a cubic cell competing for a variety of aerospace applications in which good fatigue strength and high tensile test are required [1].

A sector in which both metastable  $\beta$  and  $\alpha+\beta$  alloys are becoming always more attractive is the biomedical one. Titanium can be considered as a biomaterial because of its corrosion resistance, biocompatibility, osseointegration and of its mechanical properties [1]. The following alloys exhibit a low Young's modulus that allow to use them as hard tissue replacements [4]. The Young modulus desired must be low and very close to that of bones. To reach the proper value of it, the titanium alloys must be carefully designed in the composition and in the microstructure. The latter is primarily described by the size and the mutual arrangement of the two phases  $\alpha$  and  $\beta$  in the alloy. Generally, different microstructures are related to different thermomechanical treatments, considered as a complex sequence of solution heat treatment, deformation, recrystallization, aging, and annealing for stress relief [1]. In this way is possible to develop a biomedical alloy with desired properties that will increase the longevity and the performance of the implant [3]. The Ti-6Al-4V (Ti64) is today the most used as  $\alpha+\beta$  titanium alloy for biomedical aim, due to its enhanced strength, ductility, and high low cycle fatigue. In general, to further increase the strength of the alloy is necessary increasing the  $\beta$  stabilizer content [3].

According instead to the pressure induced transformation Ti can show one more phase called  $\omega$ , Figure 1.3. It is a hexagonal cell with three atoms per unit cell that gets formed when the pressure is increased between 2 and 7 GPa [5]. It is a metastable phase, formed both in zirconium and titanium, in presence of  $\beta$  stabilizers element, during quenching from  $\beta$  phase region or during ageing of quenched material [6]. The  $\omega$  phase, thanks to its different structure, has been revealed to have a marked effect on both mechanical and superconducting properties [5]. Regarding the mechanical properties, it has been observed an evident increase in strength, large reduction in ductility and a strong increase in the Young's modulus [6], [7]. This is the prove that under proper condition the  $\alpha$  Titanium can turn in a metastable phase. Increasing more the pressure it has been demonstrated the presence of two more phases:  $\gamma$ -Ti (distorted HCP) and  $\delta$ -Ti (distorted BCC). It has been proven that at room temperature, the phase transition from  $\omega$ -Ti to  $\gamma$ -Ti occurs at 116 GPa, and into  $\delta$  phase at 140 GPa [8].

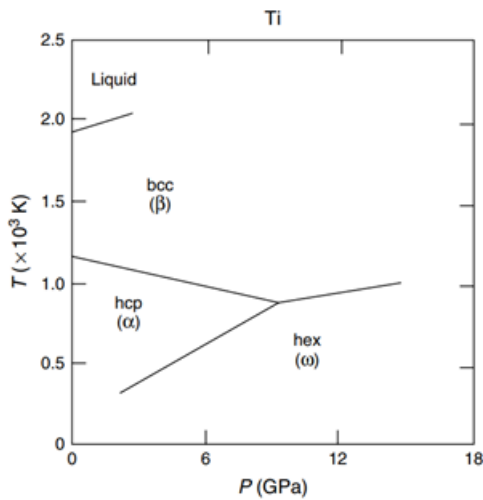


Figure 1.3: experimentally determined temperature-pressure phase diagram for Ti[9].

## 1.2. Metastable phases

### 1.2.1. Metastable phases in titanium films

In addition to the uses of Ti as a bulk material, also Ti films are already being explored in many different applications such as transistors [10] and MEMS [11]. According to the specific application the phase control of the film becomes of crucial importance to achieve the suited properties, especially at high temperature or pressure. A method to control the crystalline phase is to exploit the affinity with the substrate and induce an epitaxial growth. This has been made for the first time in 1969 by Wawner Jr. and Lawless [12] in which has been demonstrated the presence of new phase of Ti below the 35nm of film thickness. The following discovered phase is an FCC crystal structure that is not predicted by the usual temperature-pressure phase diagram; it shows different mechanical and electronic properties respect that of tradition titanium such as conductivity, magnetic susceptibility, and specific heat [2], [13]. For this reason, it is also known as exotic crystal structure of titanium.

The experiment of Wawner Jr. and Lawless [12], that lead to the discovery of the new phase below a critical thickness, consisted of a vacuum evaporation on NaCl substrate along three different orientations: (001), (110), (111). The system was maintained at a pressure of  $10^{-8}$  torr and in a range of temperature between room temperature and  $500^{\circ}\text{C}$ . The result has shown that the film growing on (1,1,1) and (001) show an FCC phase, that transforms in HCP one for thickness greater than 20-30nm. The deposit on (110) shows instead a superposition of hexagonal and face centre cubic pattern at any thickness. There are multiple plausible explanations for the presence of a two-mixture phase. The first can be related to the presence of impurities (O, N, C) that can form respectively TiO, TiN, TiC, which all possess FCC structure. The other assumption is

that the substrate lattice, that is FCC, influence the growth of Ti. Through the analysis with a spark-source mass spectrometer, it has been concluded that FCC patterns are not influenced by the presence of impurities, because the quantity of impurities is not sufficient to produce a strong change in the crystal structure. Furthermore, if the FCC structure would be related to impurities, it should have been present in the deposits on all three substrates irrespectively of the specific orientation. In view of this result, it was decided to investigate the growing film with an electron micrograph from the early stages of growth. During the nucleation of particles of titanium, it has been evident the formation of individual island typical of that of FCC metals; but increasing the thickness the FCC pattern decrease and HCP one becomes always more predominant [12].

After the discovery during epitaxial growth experiment on NaCl [12], the same experiment has been successfully extended on metallic [14], on ceramic substrates [15] and on multilayer Ti/Ni [16] and Ti/Al [17].

The presence of the FCC phase and the dependence on the sample thickness has been confirmed also with other depositions techniques by Chakraborty et al. [18] and Fazio et al. [8].

Chakraborty et al. [18] reports about a deposition of Ti thin film on top of Si (100) by DC magnetron sputtering. In the following experiment the film transforms from an FCC crystal structure to an HCP one by increasing the thickness. If below the 144 nm the metastable crystal structure can be stabilized, in the range of 144-720nm there is the formation of a mixture phase. Above the 720nm it is visible only the traditional  $\alpha$  phase. It's important to point out that the critical thickness of FCC titanium film is ten times higher than that of epitaxially grown films and thus the following phase exist irrespectively of the affinity with the substrate. The presence of this anomalous phase transformation is influenced by the intrinsic stress and the grain structure of the film. Examination of the structure and stress analysis, using XRD, indicates that FCC Ti remains stable within a highly compressive stress of the HCP Ti matrix, when the film thickness is relatively low. As the film thickness increases, the development of texture is mainly driven by presence of a tensile stress that led to the formation of an  $\alpha$  phase only [18].

Fazio et al. [8] has also proved the presence of FCC phase by deposition of Ti on top of Si (100) by vacuum arc discharge. The non thermodynamic phase is evident still with a different deposition technique and it does not depend on the deposition process. This means that the FCC structure of titanium exists and can be also stabilized in proper condition. Nevertheless, significant differences emerge between the two techniques. While in the first case the critical thickness was around 144nm, in the second one it doubles, around 300nm. Another important difference emerges from the different XRD intensity peaks. While film grown by sputtering present a more intense [002] peak for  $\alpha$ -titanium, film grown by arc discharge show a more intense [100] peak. This

results in a greater tendency for Ti film, obtained by arc discharge, to grow preferentially along [100], instead of the [002], typical of film by DCMS. [8]

A successive step has been made by Dellasega et al [7] trying to stabilize the exotic structure of titanium with HiPIMS and DCMS, making a comparison with the previous cited work of Chakraborty. Differently from the last, in this work the FCC phase is reported to exist only in the HiPIMS samples, and until a maximum thickness of 370 nm. Moreover, in this work has been highlighted the crucial effect of the ion energy in tuning the crystal structure of titanium. This one, together with epitaxy deposition, is another strategy to control the crystal phase of titanium. The choice of HiPIMS is related due to the high versatility among all the PVD techniques; it permits to explore a large energy ion regime, from 10-15eV to 200-300eV. In the first regime (smaller one) the penetration depth of ion is much lower than the native oxide thickness of SiO<sub>2</sub> and the system is more inclined to build an FCC structure. In the second regime the effect of the substrate is more predominant and there is the formation of an omega-phase in a non-epitaxial regime. [7]

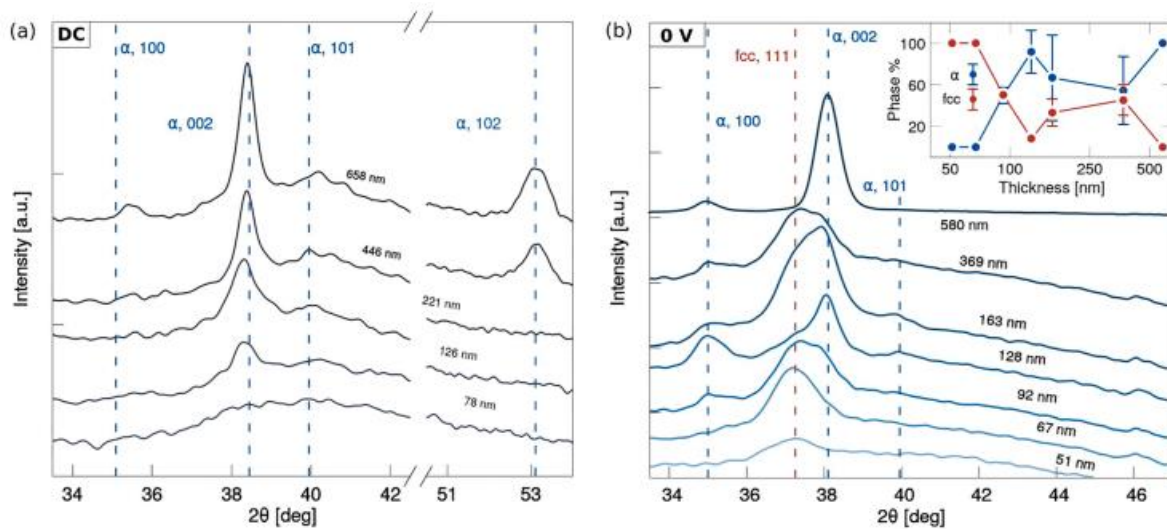


Figure 1.4: XRD spectra of titanium films deposited in (a) DCMS regime, (b) HiPIMS in the condition of 0V [7].

Despite the emerged differences, however, it can be concluded from all the experiments that the crystalline phase of the films depends on the thickness. The films initially grow as FCC to best compact the atoms and reduce the surface energy at the film-substrate interface. Subsequently, during film growth, defects form allowing the phase transformation to HCP. Therefore, the growth of the initial layer is influenced by the substrate, favouring an FCC phase, while the usual  $\alpha$  phase of titanium is associated with the deposition of successive layers. To analyse the problem from a thermodynamic perspective, it is necessary to calculate the total Gibbs free energy  $\Delta G$ . This can be considered as the sum of three components: the change in bulk free energy, the change in the elastic deformation, and the change in surface free energy (interface film-substrate). In the analysis of the process, the first one is an order of magnitude

higher than the other two, so the contribution of the others can be considered negligible. Calculations show that the total  $\Delta G$  is positive, indicating that HCP  $\rightarrow$  FCC transformation is thermodynamically unfavourable. However, the following thermodynamics-based approach cannot be applied to this problem since film growth is a dynamic process that doesn't respond to thermodynamic. [8], [18].

### 1.2.2. Metastable phases in bulk titanium

Recent studies have also confirmed the presence of the exotic FCC crystal structure in bulk titanium obtained by severe plastic deformation. It has been observed after water quenching (WQ) of thinly cold-pressed titanium discs [19], tensile testing (TT) of thin films [20], compression testing (CT) [21], cold rolling (CR) [22], laser shock peening [23] and ball milling (BM) [24], [25]. All those processes have in common the capability to deform titanium with different techniques, generating defects (twin, dislocation, and impurities), grains refinement and a compressive state of stress that stabilize the FCC structure. This structure, according to the type of process exploited, shows a lattice parameter between 4.1 and 4.42 Å in conformity with the values reported in literature for the deposition of thin films [2], [8]. The difference in the lattice parameter depends on the process adopted to process titanium and on the concentration of impurities. A higher quantity of impurities is related to a larger increase in the volume of the cell. This is proved by the fact that first principle calculation possess a much lower lattice parameter [2], [26], because they don't take into account the presence of impurities in the cell.

Table 1.2: values of the lattice parameter of FCC titanium [27].

Lattice parameter (Å)	Process	Material	Reference
4.33	BM	Ti	[24]
4.24	BM	Ti	[25]
4.20	BM	Ti	[28]
4.29-4.10	BM + annealing	Ti + stearic acid	[29]
4.10	BM (TEM observation)	Ti	[30]
4.16	BM	Ti	[31]
4.40	Thin layer deposition	Ti/Ni	[16]
4.42	Thin layer deposition	Ti/Al	[17]
4.30	Thin foil/uniaxial tensile	Ti	[32]
4.31-4.33	Thin foil	Ti	[20]
4.30	Hot rolled/compression	Ti	[21]
4.15	Compression	Ti	[33]
4.11	First principle calculations	Ti	[2]
4.10	First principle calculations	Ti	[26]
4.16	Molecular dynamics	Ti	[34]
4.10	Sintered + WQ	Ti	[19]
4.09	Rolling	Ti	[35]
4.16	Thin film	Ti	[18]
4.20	Thin film/calculated	Ti	[8]
4.29	Thin film	Ti	[36]
4.12	Thin film	Ti	[37]
4.10	High-pressure torsion	Ti-6Al-4V	[38]
4.14	Repeated impact	Ti	[27]

Among the different process of plastic deformation, the most common in the analysis of FCC titanium is the ball milling. According to Manna [24] ball-milling has a twofold effect: particle deformation and crystalline refinement. The decrease in the grain size and the increase in lattice parameter during milling is the cause of the formation of many crystal defects such as dislocations, twins, and impurities. The phase change from HCP to FCC is gradual and accompanied by about 16% increase in volume per atom. In view of this result, the cell feels a negative hydrostatic pressure that stabilize FCC phase of titanium, otherwise not present. The milling intensity and duration are crucial to analyse the phase transformation, clearly observable at XRD spectra. As observed in the Figure 1.5, the typical XRD pattern of HCP tend to vanish and the FCC

one become always more predominant increasing the milling time. Furthermore, the peaks position tends to shift to lower  $2\theta$  values, proving the lattice expansion and the presence of a stabilizing negative hydrostatic pressure. This process results more evident at higher ball milling intensity and at higher ball milling time. But, to let the process start it must be overcome a threshold value of time, intensity, and the crystallite size. [24]

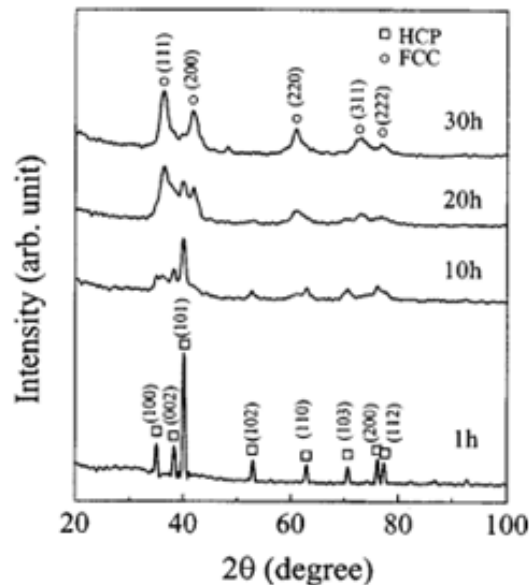


Figure 1.5: XRD spectra of titanium, showing evolution of FCC and HCP phase with milling time [24].

The critical size for the crystallite must be lower than 20nm, while the threshold time to overcome is of 16h. Before 16h of ball milling no transformation occurs, irrespectively of the intensity and of the starting dimension of grains. After 24h most of the Ti transform and just 15% remains HCP. During this process the alpha titanium remains in almost amorphous state, while FCC lattice parameter  $a$  tend to decrease with milling time toward the value of ideal FCC: 4.11 Å. Once the transformation has started, milling reduces the crystal lattice, determining a strain relief and the stabilization of new phase. [25] But it is important to point out that eventual post heat treatment of the milled Ti powder can remove the presence of the FCC phase, confirming its instability [27].

Analysing the state of the art related to both bulk titanium and thin film, it is possible to conclude that titanium exhibits a thermodynamically unstable phase. The reason for its presence can be attributed to the substrate influence, which can induce epitaxial growth, the presence of a strong compression state induced by the HCP matrix, and the presence of defects obtained through plastic deformation, the presence of impurities due to high tendency of titanium to interact with them.

### 1.3. Titanium getter function

As observed from Table 1.2, FCC Ti phase obtained by ball milling presents a lattice parameter between 4.10 Å and 4.33 Å. The reason for a non-unique value of the cell dimension can be related both to the intensity and duration of the process, as largely described in the previous paragraph. But some scientist revealed that the increase in dimension of the cell can be related also to the presence of contamination of interstitial elements. In view of this results, some studies report about the stability of FCC phase induced by H, O and N. [27], [39], [40].

From the following results, it emerges clearly that Ti has a strong affinity with impurities. The strong tendency of titanium to interact with impurities is called getter function and it can be exploited also in vacuum technology, since it works as an ultrahigh vacuum pump both at the gas phase and at solid one, known respectively as TSP and NEG.

#### 1.3.1. TSP

TSP consists in the sublimation or evaporation of titanium films to adsorb active gases such as H<sub>2</sub>, N<sub>2</sub>, O<sub>2</sub> and thus reducing the chamber vacuum pressure. This is the same working principle that occurs during the deposition of our titanium films: titanium atoms are vaporized, they react with oxygen leading a pressure drop in the chamber and then they deposit on top of Si (100). The pumping speed of a TSP depends on several factors: gas species, pressure, getter film temperature, getter film area, sublimation rate, sticking coefficient, time and conductance between the getter film and the chamber to be evacuated [41]. The pressure drop inside the chamber is also related to the speed of evacuation  $S$ . It can be considered as dependent only on sticking coefficient, getter film area and in second approximation on the ratio of temperature and molar mass of the gas to adsorb [42], as expressed in the following equation:

$$S = \left( \frac{T_g}{M_g} \right)^{0.5} sF \quad [42] \quad (1)$$

In view of this dependence, the parameter that results to have a predominant behaviour is the sticking coefficient  $s$  of the pumped gas with titanium. It is defined as the ratio between the absorbed and incident flow of gas particles. It depends both on the type of gas, on the roughness of evaporated particles, temperature and on step coverage [42]. To make a good comparison between the different active gas, it is important to define the same operation conditions. Let assume to consider having the same morphology and the same roughness of the evaporated particles of titanium, the same temperature in the system and to be in the condition of zero coverage. Under these conditions, some studies [41], [42] list the different sticking coefficient of common active gases on titanium films:

Table 1.3: initial sticking coefficient for different active gas at room temperature[41], [42]

Ts(K)	N2	H2	O2	CO	CO2	Reference
300K	0.22	0.012	0.9	0.9	0.44	[42]
300K	0.3	0.06	0.8	0.7	0.50	[41]

As reported in Table 1.3 [41], [42] the highest initial sticking coefficient  $s_0$  at room temperature of the oxygen is much higher than the other gas, explaining why titanium film are prone to interact with oxygen more than nitrogen and hydrogen. It's important to highlight that the sticking coefficient of an active gas on Ti is not constant. During the deposition, the step coverage increases until the titanium film will be no more directly exposed to the gas and so the getter function will decrease. In the case of continuously deposited films, we express the step coverage as the sorption ratio  $\gamma$ , defined as the fraction of adsorbed particles respect the incident ones [43].

$$\gamma = c s \quad [43] \quad (2)$$

In the figure below is observed that increasing the relative concentration of incident particles and the sorption ratio the sticking coefficient decrease rapidly after a threshold value.

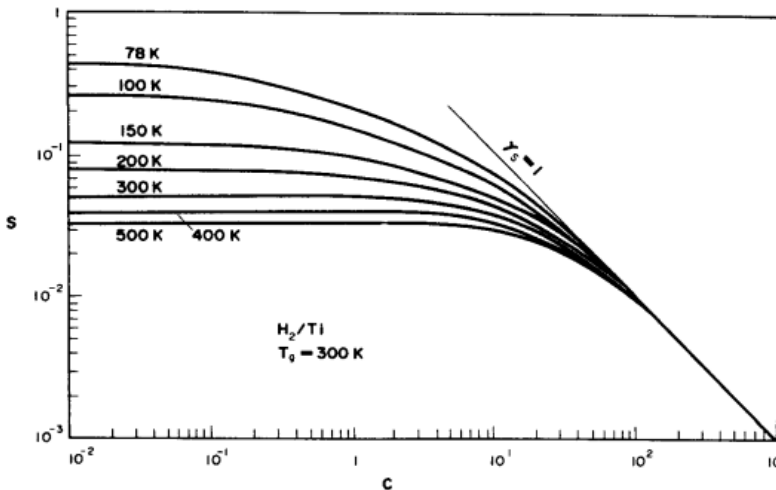


Figure 1.6: The sticking coefficient  $s$  for  $H_2$  on Ti as a function of relative concentration of incident particles  $c$  [43].

To avoid the decrease of the sticking coefficient and the loss of performances of TSP it's necessary to impose a periodic film renovation. In this way, it is possible to induce the adsorption on continuously deposited getter film, obtaining the needed value of  $s$  [43].

The second important parameter that influences the sticking coefficient is the surface temperature  $T_s$  of the getter area; in general, the temperature profile is not constant

[43], but according to the level of vacuum in the chamber and the size of the film it can be considered as uniform in first approximation. According to different studies the trend of sticking coefficient with surface temperature can be observed in the plot:

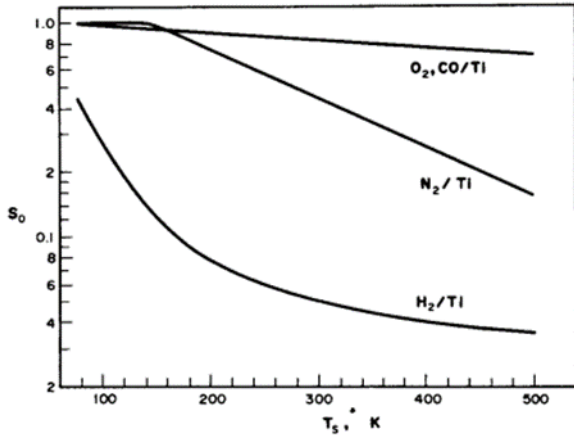


Figure 1.7: Initial sticking coefficient of following active gas as a function of the surface temperature  $T_s$  [43].

The last factor that influences the initial sticking coefficient of the active gas on titanium is the morphology of the surface: roughness and porosity. The roughness factor represents the ratio of real film area and the geometrical one [42]. Some studies of B Singh [44] have correlated this factor with the film thickness of the getter elements as shown in the figure below [42], [44].

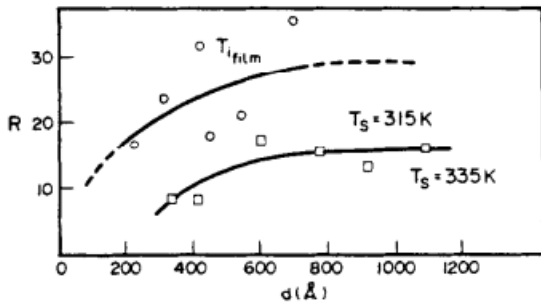


Figure 1.8: Roughness factor  $R$  dependence on film thickness [42], [44].

Thicker films are often associated with higher roughness. In the literature there are consistent data for sorption of  $N_2$  and  $H_2$  at zero coverage, in which emerge clearly the relation between the thickness and the sticking coefficient at room temperature [42]. Table 1.4 shows the initial sticking coefficient variation with the thickness of getter film.

Table 1.4: Initial sticking coefficient for N<sub>2</sub> at T=300K and variation with thickness. [42]

S <sub>0</sub>	Film thickness	T <sub>s</sub> (K)	R
0.12	60	296	9
0.15	170	296	15
0.25	750	283	28.4

All those influencing factors can be condensate in the following equation:

$$s = s_0(T_s, T_g)\phi(\theta, T_s) \quad [43] \quad (3)$$

The sticking coefficient is the product of the initial sticking coefficient  $s_0$  and the probability  $\phi$  for each gas-particle to find an appropriate adsorption site where it can be chemisorbed. The former depends on the temperature of the surface of the getter film, on the temperature of the gas to be adsorbed and on the roughness [42], [43]. The calculation of  $\phi$  results from very complicated mechanism of adsorption kinetics. Hence, in general, to define an accurate value for  $\phi$  it is adopted a semi-empirical approach [43].

### 1.3.2. NEG

Non evaporable getter (NEG) are films or more massive layers of getter material that are used to reach extreme levels of vacuum. They are of crucial importance to reach pressure below 10<sup>-13</sup> torr inside pipes with a low conductance, characterized by high length and small diameter [45]. Hydrogen outgassing from the walls of the chamber is the main obstacle to extreme vacuum. To increase the pumping efficiency and reduce the ultimate pressure, a solution could be to coat the chamber surface with a NEG film. After reaching the activation temperature, the NEG aims to transform the chamber walls from a gas source to a pump, thus preventing any eventual outgassing [45]. The non evaporable getter film to work as a pumping system needs to reach an activation temperature, to favour the high diffusion of gas in the bulk. The oxygen present in the surface oxides diffuse toward the inner part of the getter film when heated, leaving the surface exposed to absorb new gas. During NEG activation, the oxygen surface content decrease with time and temperature, reaching a minimum value when activation is completed. For this reason, surface elemental analysis is a suitable technique to monitor the process. The activation temperature can vary from 200°C to 1000°C [46] according to the type of alloy used and to its porosity. A low activation temperature usually implies high oxygen diffusivity in the getter and better performances. However, a low activation temperature is not the only requirement that must be

fulfilled for a material to be employed as a NEG film. At the activation temperature the alloy and the construction materials must require mechanical stability [45]. Since materials with high porosity (50-60%) are often employed, due to the enhanced capability of absorb gas, it becomes crucial to tune it in relation with mechanical properties[46]. A second requirement is the high solubility of oxygen to allow it to be easily incorporated in the bulk and thus to let the material undergo to many activation air exposure cycles; it must be at least of 10% [45]. To increase the capacity of accommodate more oxygen usually is exploited an increase of the film thickness, usually around  $1.5\mu\text{m}$  [45]. In addition to these properties related to the pumping performances, the selected materials should have good adhesion to the substrate, high melting point, high mechanical resistance and be non-toxic [45]. All these requirements are fulfilled by the element of the fourth group of periodic table of elements: Ti, Hf, Zr. They all display an activation temperature lower than  $400^\circ\text{C}$  [47]. For this reason, Benvenuti [47] reported the analysis of the different coating and the calculation of activation temperature by electron stimulated desorption technique (ESD), pumping speed measurements and Auger spectroscopy [47]. The Figure 1.9 shows the total pressure variation, induced by electron bombardment, according to the material of the coating and to the baking temperature. As clear in the plot titanium follows the same behaviour of the stainless steel up to  $300^\circ\text{C}$ , but then quickly drops by two orders of magnitude at  $400^\circ\text{C}$ . Thus, if the temperature cannot exceed  $300^\circ\text{C}$  for mechanical reasons, as in the case of aluminium and copper alloys, the deposition of a titanium film will yield no benefit respect the stainless steel. Overcome the heating temperature of  $300^\circ\text{C}$ , the chamber pressure feels a strong reduction in the pressure [47].

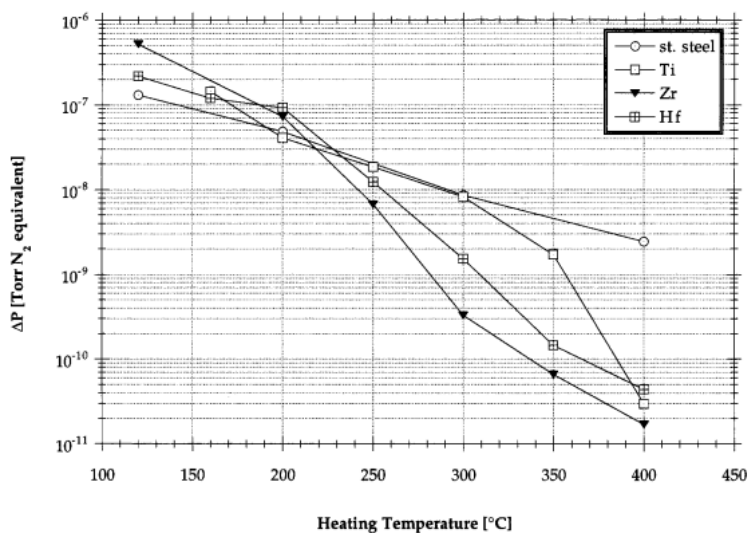


Figure 1.9: Pressure drop according to the heating temperature and material used [47].

To conclude titanium vacuum chamber can help in the reducing of the pressure acting as a getter. But to reach the desired performances, the surface oxide naturally formed on Ti must be properly removed. To clean from the natural surface oxide, it exists two methods: baking and sputtering. The former has been described until now and consists in the diffusion of surface oxide into the bulk by just raising the temperature of the titanium surface chamber. The latter consist in the remotion of oxide film by use of sputtering [48].

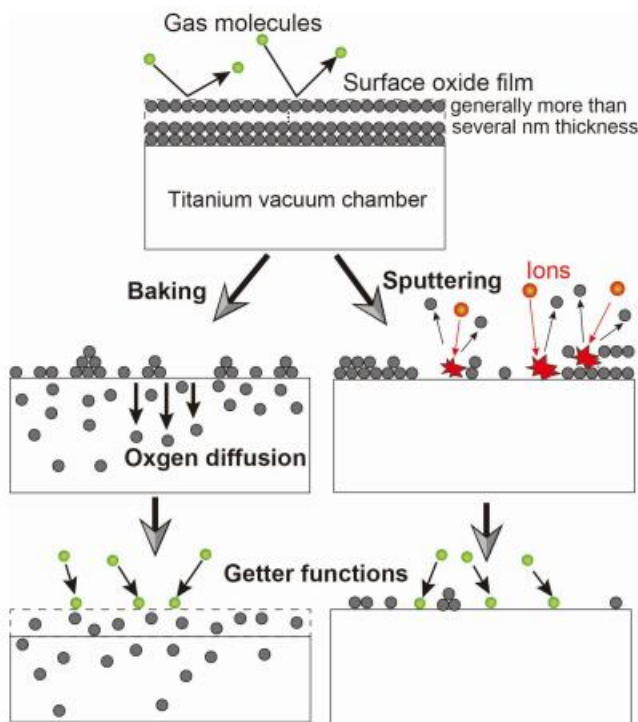


Figure 1.10: diagram of the two methods for removing surface titanium oxide [48]

Sputtering can be considered an alternative and effective technique when the material can't sustain high temperatures for mechanical issue; for example, the baking of the beam pipe at high temperature can lead to possible leak and breakage of components due to heat expansion [49]. In Figure 1.11 has been observed the different effectiveness of different pumping system in systems 1 and 2. In both the systems the pressure has decreased thanks to turbomolecular pump in the first 100h and then at  $t=100h$  has been heated the surface to promote the baking effect. After around 20h in the system 1, that undergoes sputtering of surface oxide, there is an increase the pumping speed respect the system 2, in which no sputtering effect is exploited. This is an ulterior proof that the sputtering of oxide is very efficient as a pump [49].

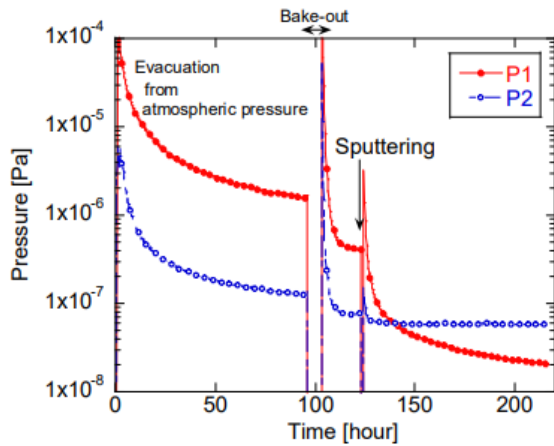


Figure 1.11: comparison of sputtering, baking and turbomolecular pump performances in the reduction of pressure with time [49].

The only problem that arises in the Ti NEG pump is the reduction of pumping performance once the film is exposed to air. When the surface of NEG film enters in touch with atmosphere the film tends to form again the stable oxide previously removed. This will lead a strong decrease of the sticking coefficient of active gas, losing its getter function. A possible solution is to cover the titanium chamber surface with a more efficient NEG alloy such as Ti-Zr-V. First the titanium oxide formed in titanium film is sputtered and later the new NEG coating is applied. In this way the oxide that can form on top of the new alloy may easily diffuse to the underlying titanium bulk because there's no oxide film to hinder the diffusion [49].

## 1.4. Aim of the thesis

Regarding the literature of thin titanium films, it comes out clearly that the FCC phase is not stable for any condition, but it strongly depends on the process condition. FCC phase has been stabilised only by epitaxial and by high energy deposition techniques. The energy regime of the species during deposition is a parameter of crucial importance to favour the growth of FCC phase. DCMS [7], [18] technique revealed the quasi-impossibility to deposit FCC titanium film on Si (100) because of the small energy regime (few eV) of the species involved. Conversely, high-power techniques such as HiPIMS [7] and vacuum arc technology [8] represent an ideal tool to explore high energy regimes of the species. HiPIMS has a regime deposition energy of 20-300eV [7] and the vacuum arc techniques can permit to obtain until 200eV [65].

In this context, it is placed this thesis work that aims to investigate the stability of FCC phase by Pulsed Laser Deposition (PLD) at the varying of process conditions.

The main reason for the adoption of this deposition technique is related to extreme versatility, due to a wide range energy of the species explorable (10s eV to 100s eV). Thanks to its both pulsed and high energy regime, PLD establishes an out of equilibrium regime, that may seem the ideal tool to favour the stabilization of complex stoichiometry and metastable phases, such as the FCC one for Ti [50]. The second point to highlight is to see if the getter function of titanium has any influence on the quantity of oxygen present in the film and if there is any correlation with the stabilization of FCC phase, as proposed by some studies [27], [39], [40].

Summarizing, the objectives of this thesis are:

1. Investigation of metastable FCC phase of thin titanium films at different working conditions, focusing on the role of thickness films and oxygen concentrations.
2. In case of stabilization of FCC phase, calculate the cell parameters and compare with that of Table 1.2.
3. Comparing the morphological, chemical, and structural analyses of the films obtained with that of other techniques.

## 2 Materials and methods

In the previous chapter has been presented an overview of the state of art regarding titanium bulk and films, focusing on the FCC metastable phase, not predicted by thermodynamic. The aim of this chapter is to present the different experimental techniques exploited to obtain and characterize titanium films, providing a basic knowledge about the working principle of the instruments adopted in this thesis work.

### 2.1. Pulsed laser deposition (PLD)

Pulsed Laser Deposition (PLD) is a versatile PVD technique that permits the deposition of thin films exploiting the ablation of a target material thanks to a laser source [50]. The extreme versatility process is related to the great number of parameters that can be modified during the deposition. Thus, PLD can be adopted for the deposition of metal, metal oxide, ceramic, semiconductor, and organic compound too. In Figure 2.1 is shown the typical apparatus of PLD.

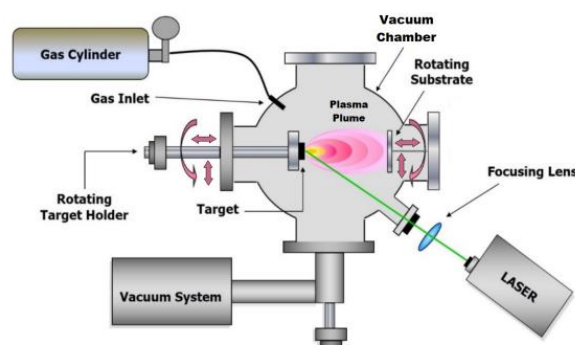


Figure 2.1: experimental set-up for Pulsed Laser Deposition (PLD) experiments [53].

It is made of a laser source and a stainless-steel vacuum chamber, hosting target and substrate, in which the vacuum pressure can reach until  $10^{-4}$  Pa, thanks to the combined action of a scroll and a turbomolecular pumping system. The laser source has a pulsed behaviour in the order of ns, but exist instruments in which is exploited also shorter pulsation period, around fs. The most used systems for material deposition are nanosecond lasers because the ablation can be considered as a thermal process. [50] According to the energy regime required it is possible to properly tune the laser

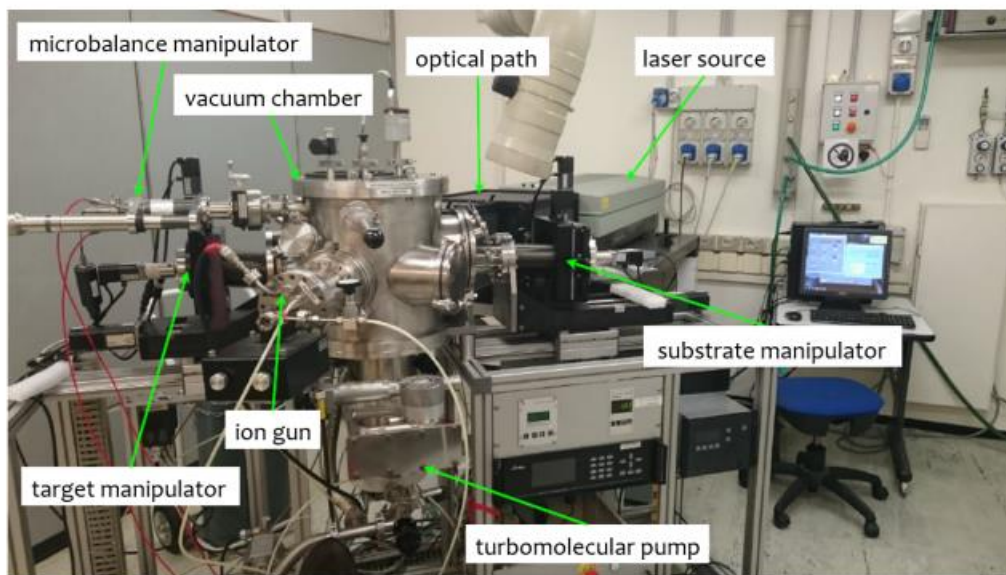


Figure 2.2: picture of the PLD used for this work thesis [77].

fluence, acting on wavelength, the delay of the laser and the position of the lens, that permit to obtain a more focused spot. The laser fluence is the ratio of the energy perceived by the target and the spot size. Since the laser power is typically at the order of 10-100MW and the size of the spot of the order of millimetres, the laser fluence values will be of several  $\text{J}/\text{cm}^2$ . [51] In our experiment we fixed the value of the lens at 35mm and the wavelength to 532 nm, modifying just the delay of the laser, obtaining fluence values between 2 - 10  $\text{J}/\text{cm}^2$ . After passing through the focal lens, the laser goes through a window with a note transmittance and hit the target with an incidence angle of  $40^\circ$ - $50^\circ$ . The target, as the substrate, are connected electrically to different motors that permit the translation and the rotation of the components. Thanks to a specific program, it is possible to set up a speed translation profile for the target. In this way it is possible to set properly the motion of the components during deposition to maintain a uniform ablation of the target surface and avoid the surface roughening [50]. When the laser hit the target with a fluence higher than threshold one, characteristic of target material, each laser pulse vaporizes small amounts of materials from the target, generating an intensely forward-directed plasma plume that supplies the film growth [52]. Thus, the PLD deposition are affected by many different factors such as the

geometry and motion of substrate and target, the temperature of the substrate, the laser parameters, and the pressure inside the chamber. According to the last parameter we can distinguish deposition in vacuum and in presence of an inert or reactive gas. [50], [53]

1. In vacuum, the deposition consists in the vaporization and successive emission of particles from the target in presence of a very small chamber pressure ( $10^{-3}$ - $10^{-4}$ Pa). The plasma plume is forward directed toward the substrate without any collision and with a very weak light emission. The morphology of the film obtained results very compact, due to the higher adhesion of the high energy of the species hitting the substrate.
2. In an inert background gas, such as Ar, with a sufficient high pressure, there forms a compression zone between the ablated species and the pressure present in the chamber. The kinetic deposition occurs slower since the gas shield the particle ejected from the target resulting in a lower energy deposition and in a higher porosity of the film. Furthermore, in this case, respect the previous one, the plume luminescence become more evident, because a higher number of particles can collide producing radiative de-excitation of ablated species.
3. In a reactive gas the chemical interactions between the gas and the ablated species occurs to permit to deposit clusters with controlled composition. For instance, to obtain the deposition of titanium oxide, it is possible to ablate a target of pure titanium and let flux oxygen.

Another important parameter to be considered regarding the vacuum pressure is the dimensionless parameter  $L$ . It is defined as the ration between the target-to-substrate distance  $d_{T-S}$  and the maximum extension of the plasma plume from the target surface  $l_b$ . According to the value of  $L$ , it is possible to distinguish three deposition regimes with different morphologies:

1.  $L > 1$ : the substrate is positioned outside the plume. Since the substrate is placed at high distance respect the target, the particles ablated interacts during flight forming cluster and their kinetic energy is reduced. It occurs the formation of cluster-assembled nanostructured and nanoporous film.
2.  $L < 1$ : the substrate is inside the plume. As the substrate is near the target, during the deposition the particles will possess high energy and impact directly, resulting in a well-adhered and compact film.
3.  $L \approx 1$ : substrate positioned at the plume edge. This condition represents a middle ground between the two previously mentioned cases.

PLD is a very versatile technique, that permit to explore a wide range of energy regimes, from 10s eV to 100s eV, according to different process parameters. In particular, the possibility to deposit particles at high energy regime, makes PLD an out of equilibrium technique that permits to obtain complex stoichiometries and metastable phase such as the FCC of Ti [50]. Despite the extreme versatility, simplicity and feasibility, there are also some drawbacks that make PLD not suitable for industrial process, such as:

- presence of droplets. Due to the high power of laser, sometimes occurs the ejection of larger particles that hinder the homogeneity of the film.
- low reproducibility due to the high versatility of the technique.
- the presence of defect in the film crystal lattice due to the high kinetic energy ablation particles.
- presence of impurities in the material. For this reason, usually the target is cleaned with the laser, before to start depositing.
- inhomogeneous distributions of deposited particles. Since ablated particles tend to deposit in the centre of the substrate following a gaussian profile. This is the reason why at the SEM can be observed a non-uniform thickness and there is the need to plot a thickness profile. To overcome this issue misaligning and roto-translation of target and substrate is exploited.
- planar substrates are preferred due to shadowing effect.

### 2.1.1. PLD set-up

In the following thesis work the deposition are carried out only on Si (100) and glass modifying just the fluence, initial base pressure (the pressure revealed in the chamber before the deposition), deposition time and gas atmosphere. All the other parameters regarding the configuration of PLD haven't been modified. The laser adopted consist of a Nd YAG with a wavelength  $\lambda=532\text{nm}$ , repetition rate  $f = 10 \text{ Hz}$  and pulse duration around 6 ns. The target to substrate distance has been fixed around  $d_{\text{TS}} = 7\text{cm}$ . The target used is in titanium with a purity of 99.995%. The dimension of the focal lens is of 500 mm and it is placed at a 35 mm. The substrate has no misalignment ( $M3 = 0$ ), and it undergoes rotation with a fixed value of 11rpm. The target instead is subjected to vertical translation with a constant rotation. The vertical translation is limited by  $\pm 20\text{mm}$  respect the centred position, to hinder the ablation of ferrule. The vertical motion is controlled thanks to an opportune software that permits to control the velocity profile during the deposition, to prevent the laser ablation of the target centre, where critical ablation condition occurs. The rotation of the target is fixed to  $495^\circ/\text{s}$  to guarantee a uniform deposition. All the deposited films have been obtained in vacuum condition, except for the last two that have been realised in 1Pa of Ar with a respective fluence rate of  $2.25 \text{ J}/\text{cm}^2$  and  $7.7 \text{ J}/\text{cm}^2$ .

The deposition parameters have been chosen in order to obtain a variety of thickness and oxygen concentrations with the aim to compare the results with that obtained in literature with other deposition techniques.

## 2.2. SEM and EDXS

### 2.2.1. Scanning electron microscope (SEM)

Scanning Electron Microscope is non-destructive technique that permits the investigation on the microstructure and on the morphology of the material, thanks to a high focus electron beam. The interaction of the electron beam with the sample allows to obtain images with high magnification (10x-300 000x), high spatial resolution (2nm) and high depth of focus (4mm-0.4um)[54]. For this reason, in this work, it has been exploited both to study the morphology of titanium film and to measure their thickness.

Since the working principle of the microscope exploits the interaction of electrons with the sample, there must be present a vacuum atmosphere and the material must be conductive. If the samples are not electrically conductive it will occur an overcharging of the surface and no image can be formed. Regarding the level of vacuum, the gun, that is where the electron beam is generated and focused, reach a vacuum level of  $10^{-9}$  mbar; the chamber in which the sample is placed need a lower vacuum level, of the order of  $10^{-5}$  mbar. The vacuum permits to avoid interaction of electrons with gas molecules and obtaining a high resolution.

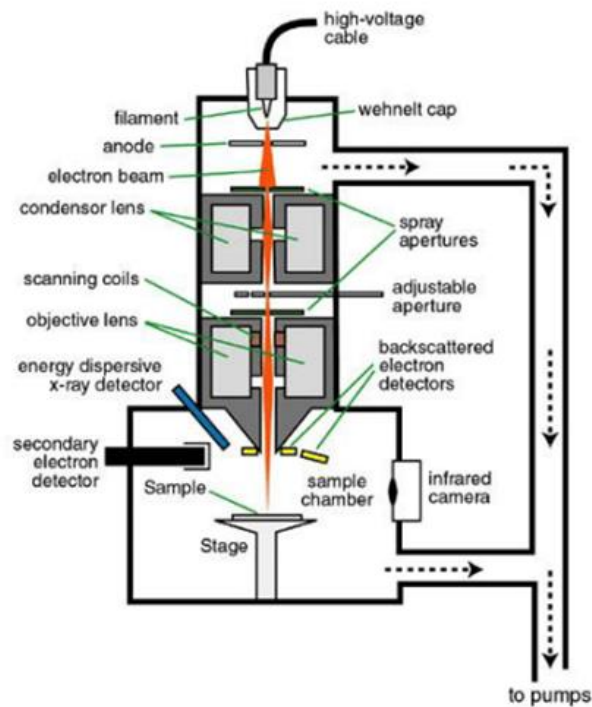


Figure 2.3: SEM apparatus [53].

As shown in the figure above the electrons are generated by thermoionic effect or by field emission inside a gun, where they are accelerated by an applied voltage (0.2-30kV), collimated and deflected thanks to electromagnetic fields and in the end are focused on the sample to be analysed [55], [56]. Incident electron beam partially penetrate in the sample and is subjected to elastic, inelastic scattering or induce photon emission producing signals of backscattered electrons, secondary electrons and X-rays waves [57]. The emitted signals are detected, collected and thanks to a complex acquisition software converted into electrical signal producing a grey scale image. SEM enables the capture of three distinct image types: 3D secondary electron images, 2D backscattered electron images and X-ray maps achievable through EDXS that will be better discussed in the next subchapter.

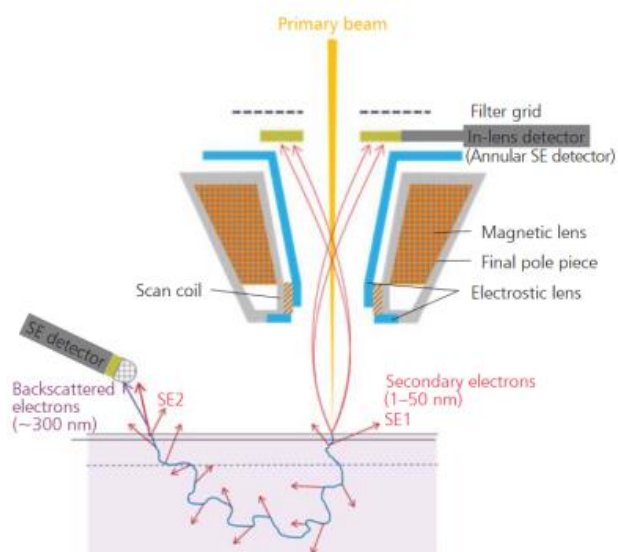


Figure 2.4: Principle of SE signal detection[58].

According to the detected signal, it is possible to obtain different information regarding the sample. In this work we have exploited just the secondary electron, providing information regarding the morphology and the topography of the film. As observed in the upper image there are two types of detectors for secondary electrons: Inlens SE and SE (Everhart-Thornley (ET)). The former is placed in the upper part of the electromagnetic collimator and detect electrons from the upper part of the interaction volume (SE1), leading to high resolution image and containing direct information on the surface of the film. The latter is placed outside the focusing lens and picks up also the electrons emitted at lower angle. Thus, it carries more information regarding the three dimensionality of the surface, but with a much lower resolution. [58]

In this work a Field Emission Zeiss SEM SUPRA 40 based on a GEMINI column has been used to obtain the cross section and the top surface images. The parameters adopted for the cross-section images are the working distance of  $\approx 4\text{mm}$ , a potential for the acceleration of electrons of 5-6kV and an aperture of  $30\mu\text{m}$ .

### 2.2.2. EDXS

EDXS is non-destructive technique that exploits the electron beam of the SEM (previously described) to calculate the chemical composition of the sample. The incoming electron beam cause an ionization in the inner shell of an atom. To return at

a more stable configuration, an electron from external shell fills the vacancy leaved by the removed one, producing X-ray. The X-ray produced are unique and characteristic for each element.[54]

The X-ray emitted by the sample must be detected and collected by a proper detector and then transformed in electrical signal. For this purpose, the detector of EDXS is made of several components [59]:

- a collimator, to ensure that only X-ray of the excited material are detected.
- an electron trap, it is based on a magnet that deflects the electrons to hinder the passage inside the detector.
- a window, that guarantees the vacuum in the detector; it is usually made of Beryllium, because it must be robust and transparent to X-rays emitted; since for low X-rays and for light element Be windows are not completely transparent, nowadays are used also polymer-based material window.
- a sensor, it is a semiconductor that converts the X-rays in electrical signals.
- a field effect transistor (FET), that being connected to the sensor, it measures the charges liberated in the crystal.
- a cooling system to maintain the detector at a temperature around  $-10^{\circ}\text{C}$ .

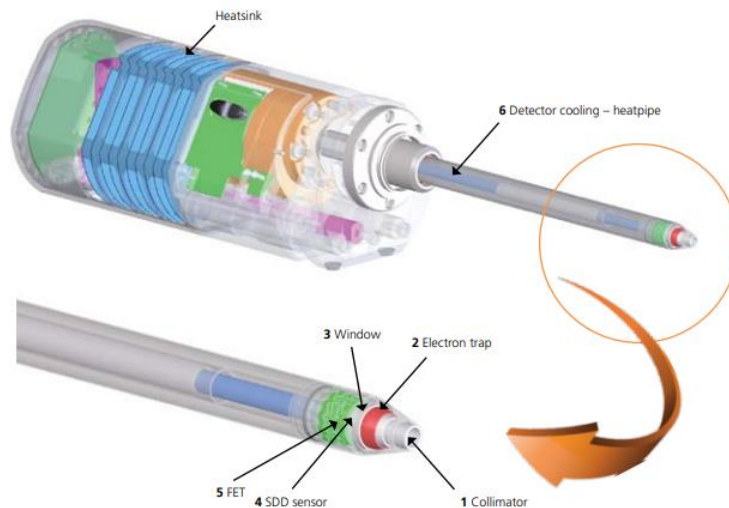


Figure 2.5: Schematic representation of a Silicon Drift Detector [59].

In this work is used an Xplore EDS detector (Oxford instruments) and the Aztec live software to make respectively:

- spectrum acquisition
- mapping

The measures have been performed with an EHT of 6 kV at a working distance around 8 mm with a magnification of 1000x and maximum aperture 120 $\mu$ m. The detection measurements are repeated for three different sites and then is calculated the average value and the standard deviation to obtain a more accurate result.

### 2.3. Raman

Raman is a non-destructive characterization technique that allows to obtain information about the crystallinity, the phase, the chemical structure of a sample, thanks to the inelastic scattering of light. [60]

When a monochromatic beam interacts with the sample, most of the light (99%) is elastically scattered. It means that the incident photon after the interaction with the sample can change its direction of propagation, but not its energy respects the emitted one. This is usually known as Rayleigh scattering. The remaining 1% of the scattered light present a different wavelength, frequency and intensity respect the incident one and is usually known as inelastic scattering. This small amount of energy is acquired through the process of inelastic scattering, where photons interact with phonons. Consequently, this energy is affected by the vibrational states within the crystal, making it dependent on the material's structural composition; the inelastic energy is the responsible for Raman characterization. [61], [62].

In the inelastic case the energy of the emitted photon can possess energy higher or lower respect the incident one, due to its specific interaction with the vibrations of the crystal, called phonons. The difference in energy between the incident and observed radiation is called Raman shift, it is expressed in  $\text{cm}^{-1}$  and represents the abscissa of the Raman spectra. It is independent of the wavelength adopted by the laser and for this it can be considered as the footprint of the chemical and molecular structure of the sample.[60]

According to the value of energy of the observed photon, if higher or lower than the incident one, the inelastic scattering can be divided into:

- stokes inelastic scattering: the resulting scattered photon loses a part of its energy due to interaction with vibrational phonon.
- antistokes: the resulting scattered phonon acquires a part of its energy due to interaction with vibrational phonon.

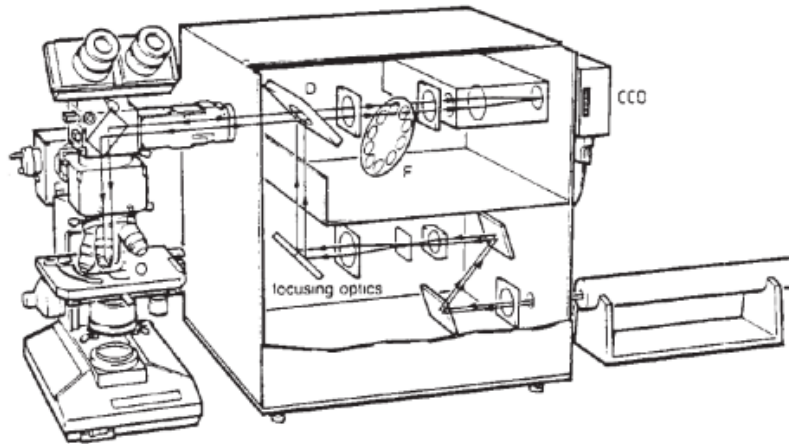


Figure 2.6: Raman spectroscopy setup with the highlighting of the beam path [78].

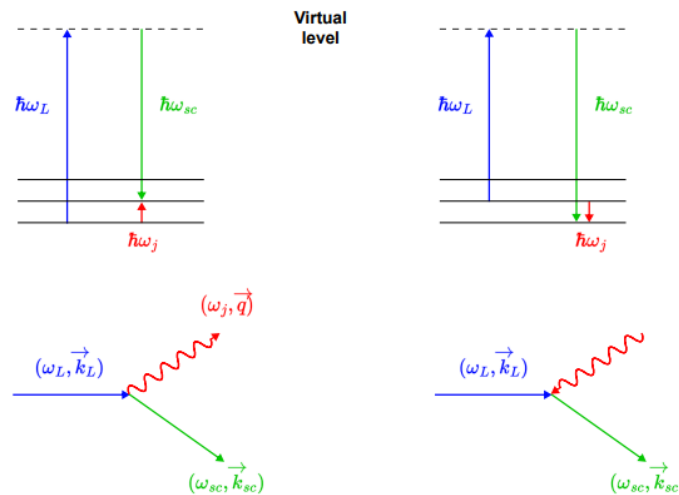


Figure 2.7: stokes (left) and anti-stokes process (right) scheme [53].

A scheme of the process is presented in Figure 2.7. As it can be observed from the following scheme, to occur anti-stokes the molecules or the crystal must be in an excited vibrational state. But according to the Bose-Einstein the vibrational ground state is always more populated respect the others and this condition is not favoured. This

means that the Stokes inelastic scattering occurs more frequently, and the relative intensity of the line is higher respect the anti-stokes one [61]. All those processes presume the interaction of the photon with the electrons, causing a perturbation of the system. In the metals this process doesn't occur because they reflect completely the light beam.

The reason why in this work has been analysed titanium films is related to the presence of possible oxide.

The Raman used in this work is a Renishaw InVia micro-Raman spectrometer, equipped with optical microscope. The laser is an argon ion source that emits in the green (514nm).

## 2.4. XRD

X-ray diffraction is a non-destructive technique employed to verify the atomic positions within a crystal, particularly for identifying the crystalline phase of the material and obtaining information about its unit cell parameters, average grain size, and preferential orientation. This technique relies on the elastic scattering of X-rays due to the periodic arrangement of atoms in the crystal. X-rays are generated through collisions with high-speed electrons. A tungsten filament emits electrons through thermionic emission, and these electrons strike a metallic target, leading to the production of X-rays. The choice of the metallic target affects the wavelength of the X-rays. [63]

X-rays possess energies in the tens of keV range [54] , which results in weak interactions with matter, rendering scattering effects negligible. X-rays easily penetrate the specimen, and due to interactions with atoms, diffraction processes occur. Each atom acts as a source of spherical waves, which, at specific angles, generate constructive interference phenomena detectable by a detector.

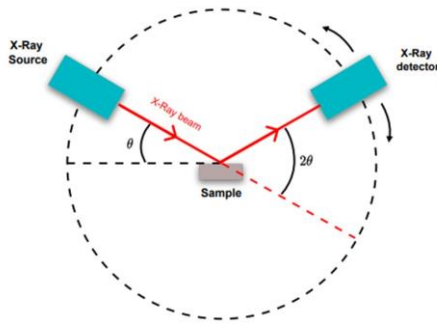


Figure 2.8: Scheme of XRD in  $\theta/2\theta$  configuration [53].

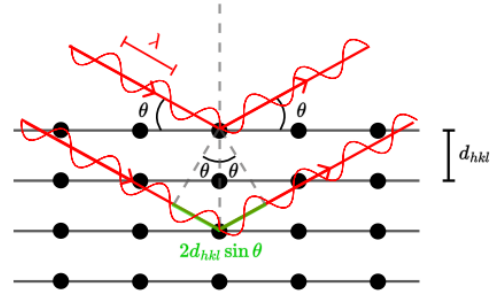


Figure 2.9: scheme of diffraction process[53].

Figure 2.8 and Figure 2.9 illustrate the configuration of a  $\theta/2\theta$  diffraction test. The X-ray beam hit the specimen, undergoes diffraction, generate constructive interference, and the signal is elaborated by a detector. For all this to occur, Bragg's law must hold. Here, "n" is a natural integer known as the order of reflection, "lambda" represents the wavelength of incident radiation (dependent on the target used), and "d" signifies the distance between crystallographic planes of the same family.

$$2d\sin\theta = n\lambda \quad (4)$$

The spectrum obtained from a material is unique for that specific element with its crystalline structure and must be compared with theoretical diffraction patterns to determine the specific phase of the given material. The presence and position of peaks are primarily associated with the crystal structure, cell parameters, and symmetry. Peak intensities are linked to the amount of radiation diffracted at that angle, and hence, to the preferred growth direction.

X-rays, according to the material under analysis, can penetrate below the surface of the crystal providing not only superficial information. It allows for high-resolution microscopic structural information, averaged over a large ensemble of atoms. The significant penetration capability and the ability to fully define phase and crystallographic properties represent an advantage, but it can also be a drawback in XRD analysis of thin films, as the substrate may influence the film measurements. In view of this issue, there is an alternative X-ray diffraction configuration to  $\theta/2\theta$ : grazing incidence X-ray diffraction (GIXRD).

GIXRD is performed at low angles, grazing the surface to avoid interference with the substrate. At X-ray energies, the refractive index of most materials is slightly less than one. Therefore, if the angle of incidence is sufficiently small, total external reflection

occurs at the surface. X-ray intensity is notably high when interacting with the film and diminishes evanescently when interacting with the substrate, rendering the substrate invisible to the radiation. [64]

Another reason for which GIXRD can be a useful technique in the analysis of polycrystalline thin film is related to the possibility of detecting not only the crystallographic planes parallel to the surface as in  $\theta/2\theta$ , but also that in any possible orientation. This occurs because, differently from traditional Bragg-Brentano configuration, the incidence angle is fixed while the scattered one varies permitting to identify all the possible orientation of crystallographic planes.

In this work, to guarantee a proper analysis of titanium nanofilm we exploited both XRD and GIXRD measurement. Those have been carried out by Alessio Lamperti in the laboratory of IMM Agrate UNIT belonging to the Physics and Matter technologies department of CNR (National research council of Italy).

The grazing incidence measurements have been performed with an incident angle of  $\omega = 2^\circ$  and exposure time of 2 hours thanks to a radiation source made of  $\text{CuK}\alpha$  ( $\lambda = 0.1541 \text{ nm}$ ). Data were acquired by a curved position-sensitive multichannel gas-filled detector ( $2\theta = 0^\circ\text{-}120^\circ$ , resolution  $0.029^\circ$ , Inel CPS-120). Unfortunately, one of the channels does not work properly and may lead to some problem for a high resolution analysis for values of  $2\theta$  around  $31^\circ$ .

For what regard the  $\theta/2\theta$  spectra, those have been obtained from previous sample not deposited by me. They share the same radiation source of grazing incidence experiments  $\text{CuK}\alpha$  ( $\lambda = 0.1541 \text{ nm}$ ).

## 2.5. Annealing

After the deposition of thin films, a part of the samples has been subjected to thermal treatment under vacuum to observe if appear any differences respect the non-annealed. Annealing measures have been carried out at  $400^\circ\text{C}$  and  $550^\circ\text{C}$  for roughly 1h in a high vacuum chamber; the base pressure of chamber in each experiment is kept between  $5 \cdot 10^{-5} \text{ Pa}$  and  $7 \cdot 10^{-5} \text{ Pa}$ ; the heating ramp is fixed to  $10^\circ\text{C}/\text{min}$ . The furnace here described is represented in the figure below.

The following measured have been performed by previous students.



Figure 2.10: furnace for annealing in vacuum.

### 3 Synthesis and morphological and chemical characterization

After the description of the experimental technique adopted, in this chapter it will be discussed first the strategy adopted to analyse the data post deposition, highlighting the role of the process parameters, and then it will be analysed in the detail the results of the characterization at the SEM and EDXS. In the next chapter the characterization of titanium films will be completed with Raman and XRD analysis.

Among the extensive set of samples analysed in this work, I personally handled the deposition and characterization of a portion, while for the remaining part, I just carried out the analysis of data and of results.

The conditions of deposition are defined by the following parameters:

- Initial background pressure or base pressure
- Deposition time
- Fluence

Table 3.1: process condition of work thesis samples.

Process condition of the samples	
Initial background pressure [Pa] <sup>1</sup>	$5.93 \cdot 10^{-4} - 1.20 \cdot 10^{-2}$
Fluence [J/cm <sup>2</sup> ]	2 - 10
Deposition time [seconds]	100 - 7200

The following table resumes the different working conditions adopted. According to the variation of each single parameter the film may be subjected to substantial differences. To understand the role of each of those, the best strategy is to keep fixed the working conditions with the variation of only one parameter. Thanks to this strategy it has been possible to understand its relative effect.

---

<sup>1</sup> The initial background pressure or base pressure is the pressure relieved in the chamber before to start the deposition.

A parameter that has not been mentioned, but, according to literature, shows a relevant impact in the stabilization of the metastable FCC phase of Ti films is thickness. It will be considered as the first result of our samples characterization and then it will be analysed its effect on the morphology, XRD and Raman spectra. Thickness is not a process parameter because it depends on fluence rate and deposition time.

Before to start the characterization, it is important to highlight two phenomena that occurs during the synthesis of our films.

The first is that the background pressure is not a constant parameter, but it decreases during the ablation of titanium target. The following process is a peculiar feature of titanium deposition, consequence of its getter function; it will be analysed into the detail in the subchapter 3.1.

The second anomaly that became evident during the depositions was a noticeable decrease in the window transmittance after certain deposition time. This led to a variation of fluence for different depositions and to a non-constant fluence rate for excessively long depositions. Unfortunately, this issue has affected a portion of our samples. To address the problem, it has been considered necessary to clean the window after each individual deposition.

### 3.1. Titanium getter function and cleaning

The experimental evidence that titanium is a getter element comes out during the ablation of the target. When the deposition starts, it has been observed a net decrease of chamber pressure.

The aim of this paragraph is to provide a comparison between the pumping speed due to titanium ablation and that of turbomolecular pump highlighting which of the two is more performant according to different values of background pressure, fluence.

When the turbomolecular pump is on, the air present in the chamber evacuate with an exponential decay trend, represented below:

$$P = 0.00085 + 0.02 e^{-\frac{x}{8.43}} + 0.008 e^{-\frac{x}{41.6}} \quad (5)$$

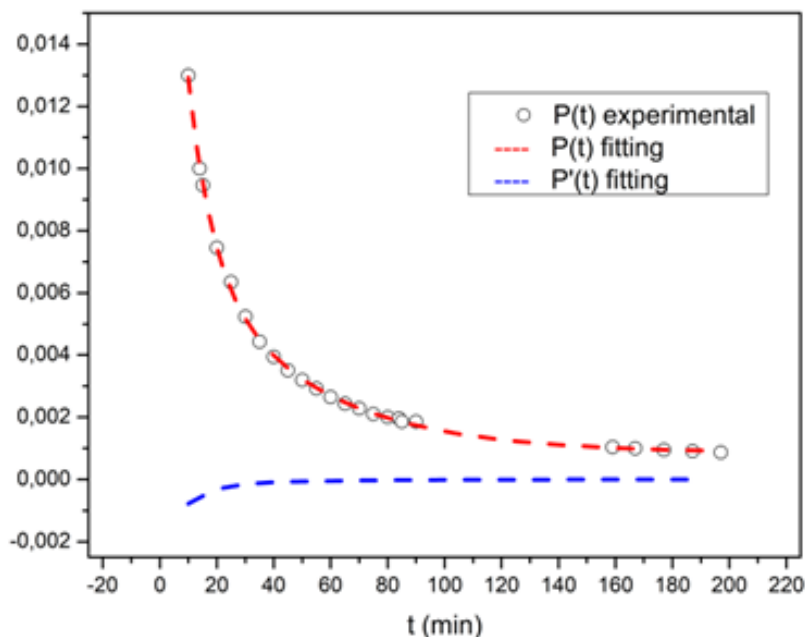


Figure 3.1: variation with time of pressure (in red) and first derivative (in blue) of turbomolecular pump when active.

In the Figure 3.1 it has been observed that at higher background pressure the turbomolecular pump will have higher pumping rate<sup>2</sup> and better performances. After circa 80 minutes the pressure reaches a plateau and the pumping speed, described by the first derivative of the pressure respect to time, tend to zero. It means that after a threshold value of background pressure, the pumping efficiency tend to vanish. To overcome this issue, it can be thought to exploit the getter function of Ti, making it work as TSP. To make that happen, the substrate is placed at the highest possible distance from the target, the shutter has been lowered and it has been started the ablation of titanium target. The reason for this procedure is to reduce quicker the pressure in the chamber without depositing the ablated particles. The following process is known as cleaning.

The cleaning process has been studied under different conditions of background pressure, and fluence to understand if those parameters influence the performance of "TSP".

---

<sup>2</sup> The pumping rate or pumping speed is considered as the first derivative of the pressure respect to time.

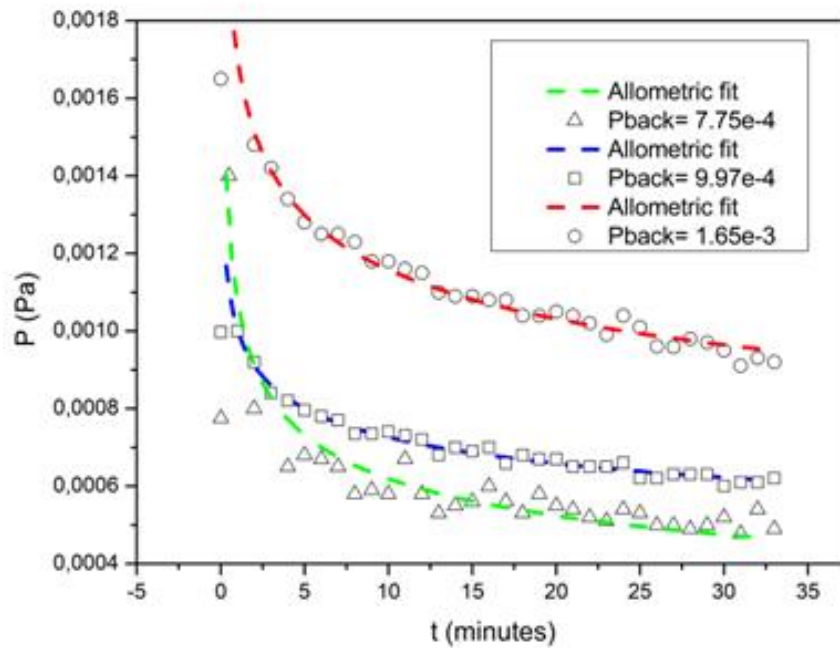


Figure 3.2: Chamber pressure variation with time during ablation of the target at different background pressure. Trend fitted with allometric function.

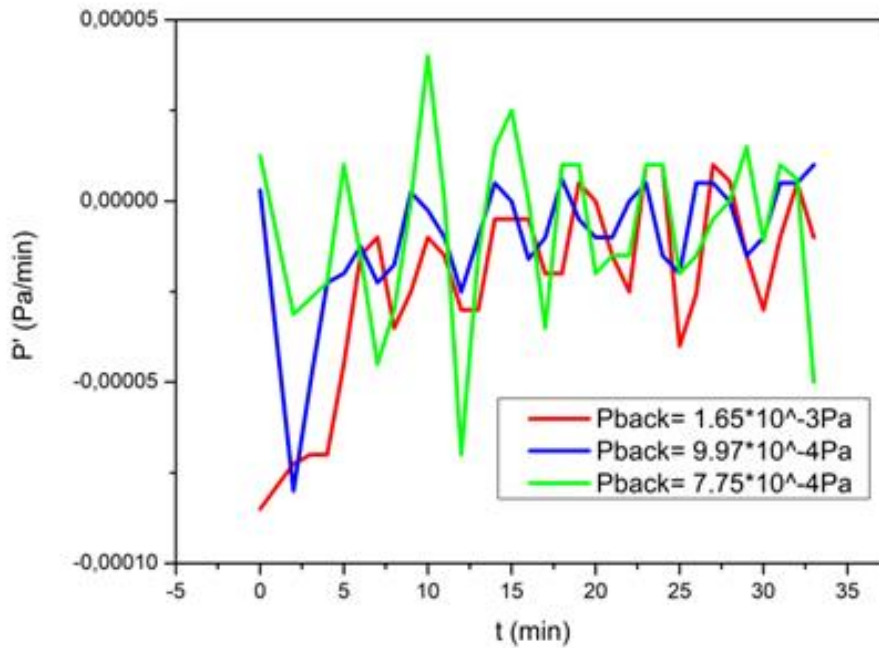


Figure 3.3: First derivative of the chamber pressure variation with time during the ablation of target at different background pressure.

To see the trend variation of “TSP” according to modification of background pressure, fluence must be keep fixed. Fixed the fluence to a value of 4J/cm<sup>2</sup>, it is possible to observe the variation of pressure and pumping rate at different background pressure.

The functions above have been fitted with an allometric function  $y = a x^b$ , because interpolate the experimental data better than exponential functions.

Table 3.2: different values of parameters of allometric functions according to different initial background pressure values.

Initial background pressure [Pa]	a	b
$7.75 * 10^{-4}$	0.001	-0.24
$9.97 * 10^{-4}$	0.001	-0.14
$1.65 * 10^{-3}$	0.0017	-0.17

This is a proof that the pumping of “TSP” follows a different physics process respect that of turbomolecular one.

From the plots clearly emerges that the ablation of titanium lead to a strong decrease of pressure. However, the trend of the pressure is not monotonic, but follows small oscillation of the order of 10<sup>-5</sup>Pa, that becomes more evident at lower pressure. This is confirmed by the plot of first derivative respect to time. Since the oscillations emerge only during the ablation of the target and not during the turbomolecular action, we can be sure that the oscillations are not related to the sensibility of the vacuum gauge but only to the process of ablation. It is interesting to investigate on the possible causes. The starting point of our analysis is that the periodic oscillation must be related to a periodic process that occurs during deposition. During the deposition it can be identified two cyclic processes: the motion of the target, the pulsing of laser. To establish which of these can better explain the oscillating trend, it is important to compare the values of oscillation period with that of target and laser. Since the period of the oscillation in the pressure rate is of the order of two minutes it cannot be related neither to the laser, where the period between each pulse is of 6ns, nor to the motion of the target that takes 1 minutes to return to initial position. Despite this remains almost an open question, it is possible to conclude that the following oscillations are

symptom of a different dynamics of pumping. In fact, TSP behaviour cannot be fitted with the same functions that correctly describe the behaviour of the turbo and for this reason a mathematical comparison of the rate of pumping cannot be done. The solution to establish a good comparison is to overlap the function that perfectly fit ( $R^2=0.999$ ) the experimental data of our turbomolecular pump with the experimental one of "TSP".

Keeping fixed the value of the Fluence at  $4\text{J}/\text{cm}^2$ , it emerges from the plot that:

- at  $F=4\text{J}/\text{cm}^2$  the pressure drop with cleaning is higher respect the TMP
- at higher background pressure the performance of TSP is better. In Table 3.3 it can be seen in first approximation the percentage of pressure reduction of TSP at ablation time equal to 33 minutes changing with background pressure.

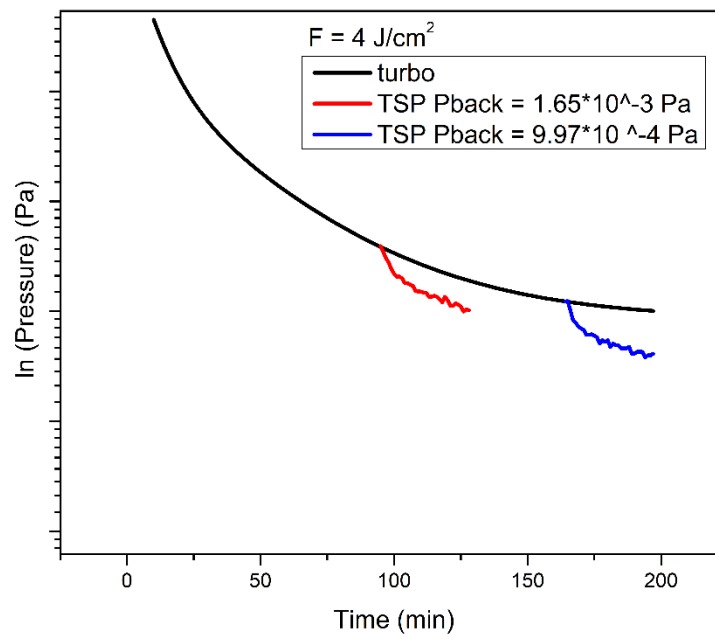


Figure 3.4: Comparison between the turbomolecular pumping curve and the "TSP" one at different background pressure. The pressure is plot in ln scale.

Table 3.3: Comparison of different performance of TSP at different background pressure, keeping fixed time to 33 minutes and fluence to 4J/cm<sup>2</sup>.

F=4J/cm <sup>2</sup> ; ablation time = 33minutes			
Initial background pressure [Pa]	7.75 *10 <sup>-4</sup>	9.97*10 <sup>-4</sup>	1.65*10 <sup>-3</sup>
Final background pressure [Pa]	4.90*10 <sup>-4</sup>	6.20*10 <sup>-4</sup>	9.20*10 <sup>-4</sup>
$\Delta P$ /Initial Pback	37%	38%	44%

Keeping fixed the background pressure, it can be thought to start the cleaning process at different fluences.

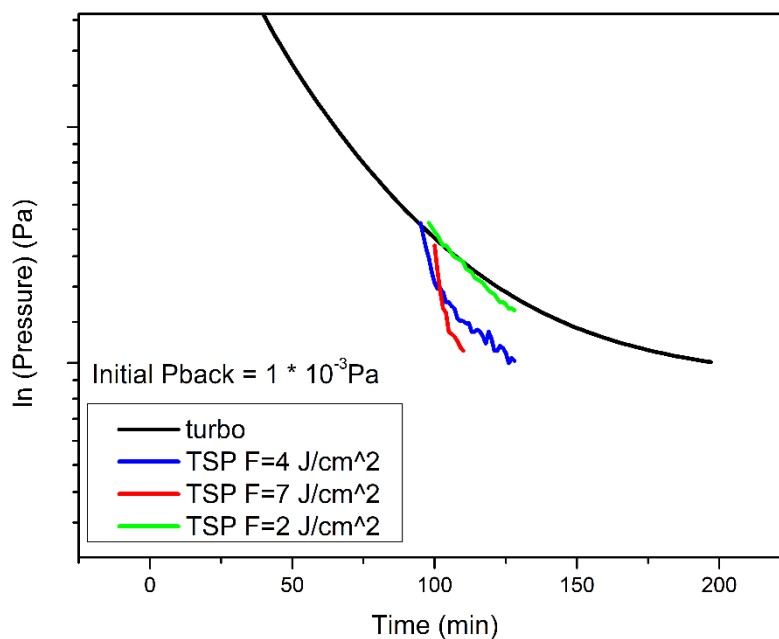


Figure 3.5: comparison of turbomolecular pumping rate with the “TSP” at different fluences.

The following plot compares the turbomolecular pumping performance with that of TSP at different fluences. From the following, it is possible to conclude that in the range of pressure (lower than  $1 \cdot 10^{-3} \text{Pa}$ ) in which turbo is reaching a plateau:

- the cleaning is always more performant than TMP, even at  $F=2 \text{J/cm}^2$ .
- the cleaning at higher fluences lead to stronger decrease in pressure. This is consistent with the fact that there is more titanium available to grab the oxygen in the chamber.

Now that it has been largely discussed the physical process of pressure variation due to getter function of titanium, it can be also elaborated an opportune strategy to obtain the desired level of vacuum in the chamber in less time, exploiting titanium getter function. The following plot represents the synthesis of the strategy: 65 minutes of turbomolecular pump and 35 minutes of TSP permits to achieve value of  $1 \cdot 10^{-3}$  in 95 minutes. A use of only turbo has been needed almost twice the time.

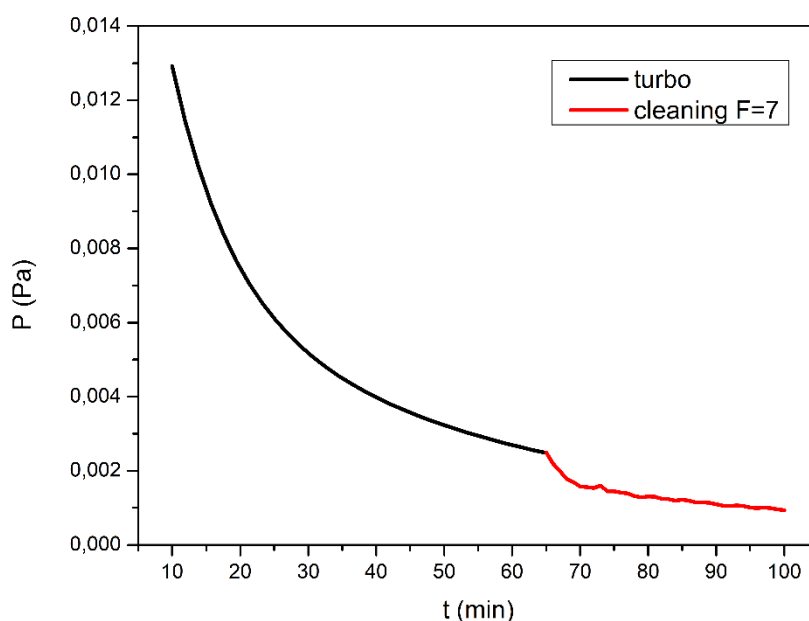


Figure 3.6: strategy to reduce the vacuum pressure exploiting the cleaning with a fluence rate of  $7 \text{J/cm}^2$ .

Table 3.4: comparison in term of time between the two different strategy to reach vacuum pressure of  $1 \cdot 10^{-3} \text{Pa}$ .

	P target [Pa]	Time [min]
<b>Only turbo</b>	$1 \cdot 10^{-3}$	170
<b>Turbo + TSP (cleaning)</b>	$1 \cdot 10^{-3}$	95

The reason for this brief excursion into chamber pressure values is driven by three key factors:

1. To experimentally demonstrate the getter functionality of titanium in this work.
2. To show that the parameter P background is a function of deposition time.
3. To formulate a strategy for accelerating chamber pressure reduction.

## 3.2. Morphological and thickness analysis

In this chapter will be investigated the morphology of deposited titanium films and the relative thickness thanks to the use of SEM. It permits to calculate the thickness profile of the film and to observe the morphology of the film, both in plane and in cross section. The thickness of the film obtained depends only on fluence and deposition time; since the values of background pressure in our experiments is of  $10^{-2}$  -  $10^{-4}$  Pa, the mean free path of the species ablated hasn't been affected and its effect can be considered negligible. Once measured the thickness of the film, it is possible to deduce the deposition rate and its variation according to the value of fluence adopted.

### 3.2.1. Fluence threshold

The first important analysis that can be done knowing the thickness of the film is the evaluation of threshold fluence. The threshold fluence is the value of fluence required to start the ablation of the target [65]. It will depend only on the target material.

Once measured the thickness, it can be calculated the deposition rate at a certain fluence rate. The deposition rate varies between 0.047 nm/s and 0.30 nm/s for respectively fluence value between 2 J/cm<sup>2</sup> and 10.57 J/cm<sup>2</sup>. Since the deposition rates calculated are very small values, they are very sensible to the conditions process and will possess a certain dispersion. The best method to overcome this issue is to plot a thickness vs time plot at a fixed fluence value. Thanks to a linear relation between thickness and time, it is possible to perform a linear fitting and calculate the slope of the curve; the physical meaning of the slope will be the deposition rate of titanium at that respective fluence.

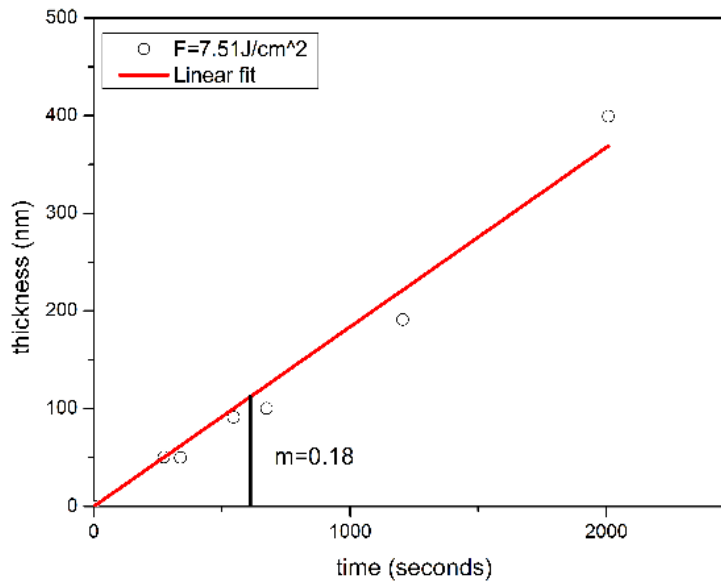


Figure 3.7: Thickness vs time fixed the fluence to 7.51J/cm<sup>2</sup>. The slope  $m$  is the deposition rate (nm/s) relative to the value of fluence adopted.

The same process has been repeated for different values of fluence. Once calculated the deposition rate for the different values of the fluence, it's possible to represent the following plot:

$$Dep\ rate = -0.03 + 0.028 F \quad (6)$$

The equation above is represented in Figure 3.8. The first observation to highlight is that the behaviour is almost linear and that the intercept with the x axis is a value different than 0. It means that that exist a value of fluence below which no deposition occurs. In the assumption that the ablation rate and the deposition rate are in linear relation, it is possible to consider this value as the threshold fluence. In this approximation the following value resulted to be around 1.07 J/cm<sup>2</sup>, being in pretty accordance with the values presented in literature [66], [67].

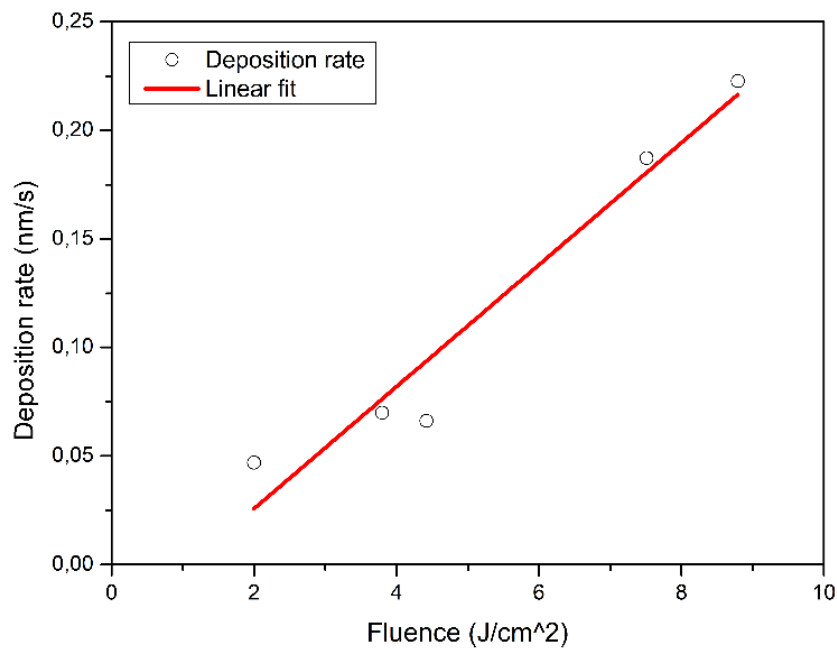


Figure 3.8: deposition rate vs fluence rate. It can be fitted with an almost linear behaviour ( $R^2=0.93$ ). The fluence rate results to be around  $1.07 \text{ J/cm}^2$ .

### 3.2.2. Thickness profile analysis

Despite the relative motion of target and substrate, the films deposited by PLD, as described in 2.1, have non uniform thickness due to the gaussian shape of the ablated species emission. In view of this, during the cross-section analysis has been measured the thickness profile to calculate the average value of the thickness and the distribution of the values.

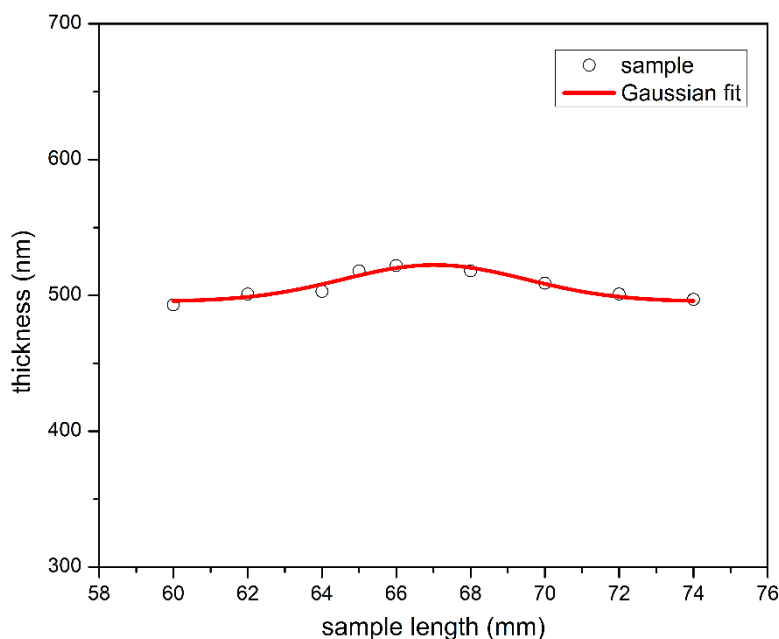


Figure 3.9: example of cross section thickness profile of our samples.

In Figure 3.9 is shown a cross section thickness profile of a random sample just to show that it confirms the theoretical shape expected from PLD films; the thickness measures have been taken every 2mm. This trend is confirmed irrespectively of the process parameters adopted and eventual variations in the shape may be symptom of the decrease in the window transmittance. From the following profile the resulting thickness that will be considered from now on will be the average value.

### 3.2.3. Morphology of Ti films

The aim of this subchapter is to characterize the morphology of thin films titanium (in cross and in plane view) comparing with that of other metal films obtained at PLD and with other titanium films obtained with different deposition techniques.

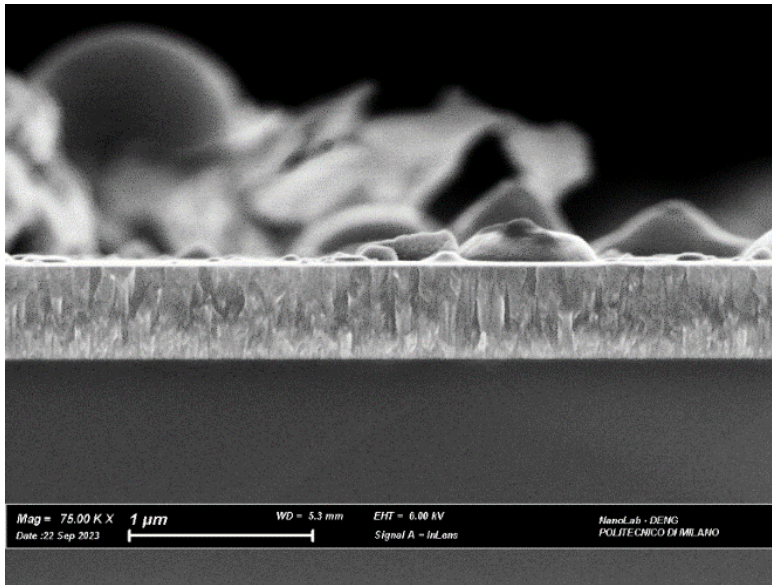


Figure 3.11: SEM cross section image of our titanium films by PLD. The following film is 507nm thick.

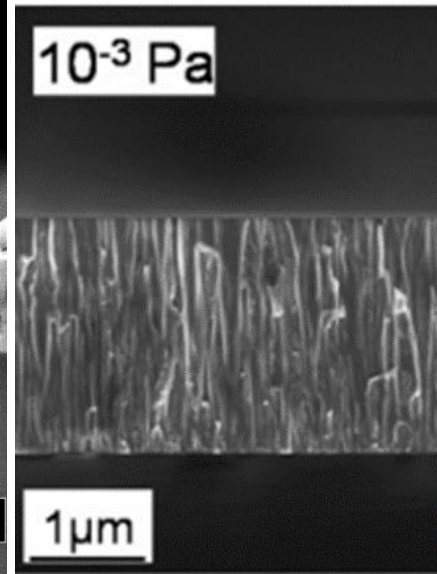


Figure 3.10: SEM cross section of W films deposited in vacuum by PLD [68].

As observed in the Figure 3.11 the morphological structure of the titanium film is columnar and oriented in accordance with the high energetic regime of PLD that in vacuum promotes compact and oriented films. Almost all the samples show the same morphology, irrespective of fluence, background pressure and deposition time.

The following morphology is not a typical feature of titanium films, but it is dictated by the strong tendency of PLD to form compact and columnar films in vacuum. This is demonstrated by a similar morphology of other metals, such as W [68]. The variation of the morphology can occur in presence of an important contribution of inert gas [50], [53], [68] that influence the value of L. Since the target to substrate distance hasn't been modified and all the deposition has been made under vacuum or with a small amount of Argon (1Pa) the following results do not show important variations.

The only sample of which is important to highlight the peculiar morphology is that with a sensible higher thickness respect the others. All the samples with the morphology of Figure 3.11, described until now, have thickness values between 50nm and 600nm and do not show relevant differences.

The sample of Figure 3.12 has a thickness of 1922 nm. It shows a less defined columnar morphology, with a more random growth, maybe related to the higher residual stresses formed for too high thickness values.

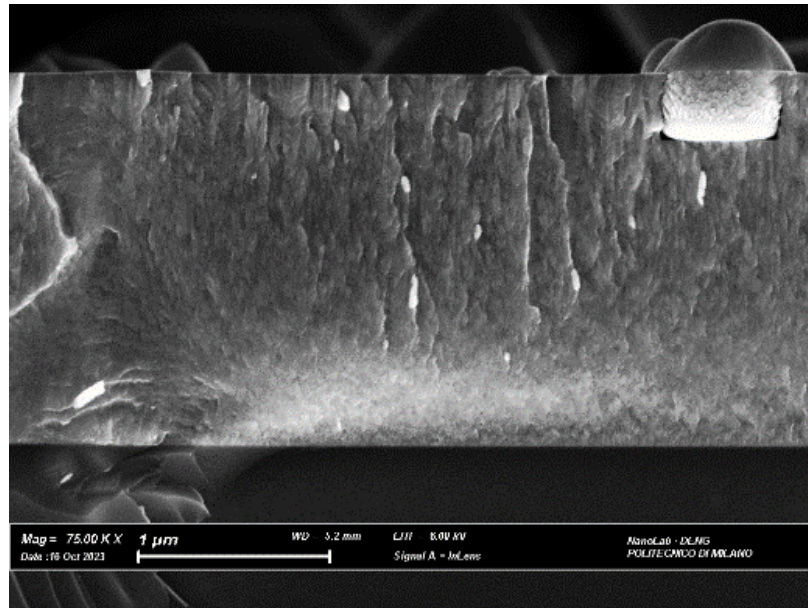


Figure 3.12: SEM cross section of high thickness (1922 nm) titanium film by PLD.

For what regard the differences with the morphologies with other deposition techniques, in the following will be analysed a comparison with DCMS and HiPIMS deposition performed by Dellasega et al in its work [7] .

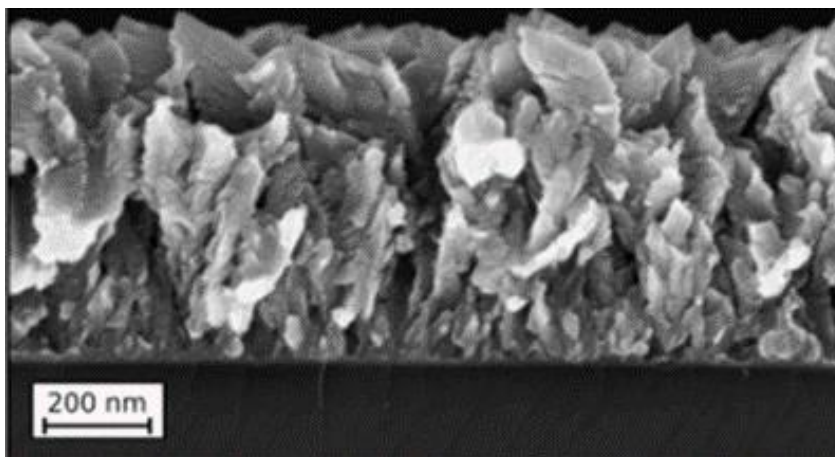


Figure 3.13: SEM cross section morphology of Ti films by DCMS [7].

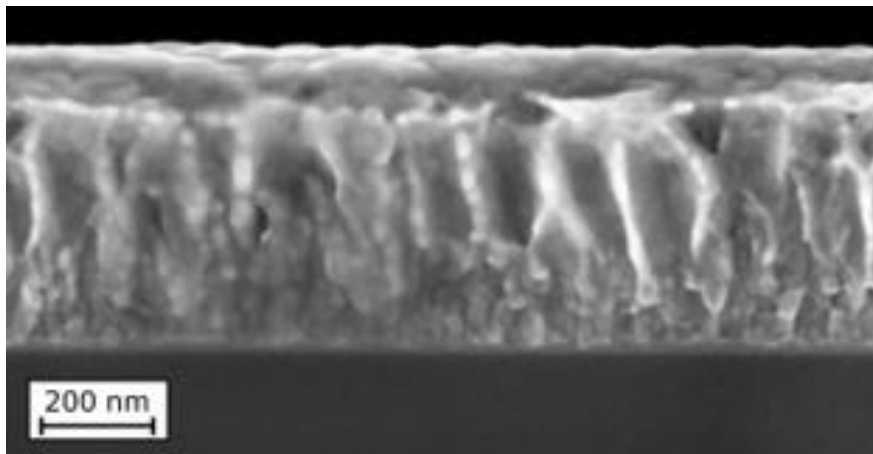


Figure 3.14: cross section morphology of Ti films in HiPIMS regime without an applied bias [7].

Despite the different scale, both the deposition techniques are characterized by a different morphology respect the PLD, but it is possible to observe some similarities between the columnar behaviour of HiPIMS and our samples at PLD. The reason may be related to the high energy range of the species of HiPIMS respect DCMS, thus building a morphology more like that of PLD samples.

Last part of the paragraph is devoted to the analysis of the plane view of our titanium films. Regarding that, it is clear the presence of droplets irrespective of the working condition adopted; they are constituted by Ti and O. From the figure it is evident that the dimension and the number of droplets is influenced only by the different fluence rate. Increasing the fluence and keeping fixed the other parameters the droplets increase in number and dimensions, as observed in Figure 3.15 and Figure 3.16.

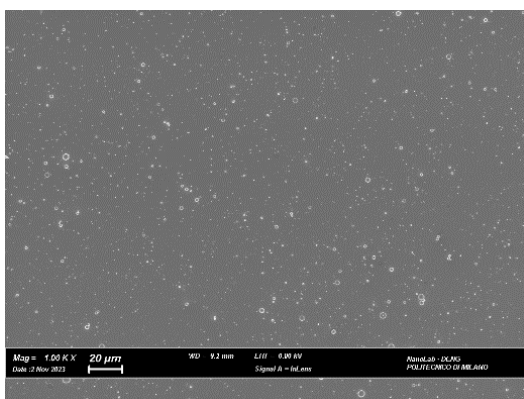


Figure 3.16: Ti films by PLD plane view  $F=2 \text{ J/cm}^2$

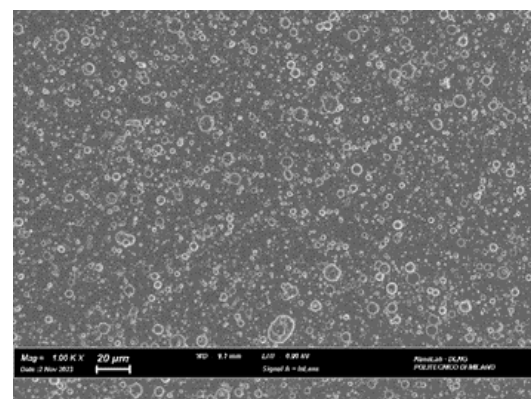


Figure 3.15: Ti films by PLD plane view  $F=7 \text{ J/cm}^2$

### 3.3. Chemical and compositional analysis

Chemical and compositional analysis have been performed thanks to EDXS software. The elements that have been detected are titanium, silicon and oxygen. Even if silicon is detected, it is not really present in the film, its presence is justified by the fact that the electron beam penetrates in the subsurface, in fact its quantity increases with the lowering of the thickness. To overcome this limit, the relative atomic concentrations of the elements are renormalized without considering silicon. This permit to calculate the real quantity of titanium and oxygen in the film. The quantity of oxygen in the film is higher than 30% in all the samples and it has been justified in paragraph 3.1 thanks to the getter action of Ti. Since the oxygen tend to stabilise the FCC structure, as reported in literature [23], it has been considered of crucial importance to study of the Ti/O ratio and an eventual correlation between the process parameters and atomic oxygen concentration.

Table 3.5: atomic concentration of elements (Ti, O) in the Ti films produced by PLD in vacuum.

Element	Atomic percentage
Ti	50%-68.97%
O	31.03%-50%

#### 3.3.1. Influence of process parameters on oxygen concentration

The reason why we are focusing on the concentration of oxygen is related to the fact that it seems to stabilise the metastable FCC phase of titanium according to literature [27] . In this chapter is analysed the influence of background pressure, fluence and deposition time on the atomic oxygen concentration in the film.

To show the effect of background pressure it has been plotted the concentration of oxygen at three different pressures keeping fixed both the fluence and the deposition time. As observed in Figure 3.18 the background pressure is not a relevant parameter in the variation of oxygen concentration in the film. This is consistent with the fact that, being a non-constant value during the deposition, its influence on the oxygen concentration cannot be considered reliable.

The same plot seems to give information also on the effect of fluence. We see that for decreasing of the fluence rate (at the same background pressure) the concentration of oxygen seems to increase. However, among the different sample analysed it emerges a contrasting effect of fluence, Figure 3.17. The contrasting effect of the fluence rate in the variation of oxygen present in the film may be related to the lost in transmittance of the windows that lead to non-coherent results.

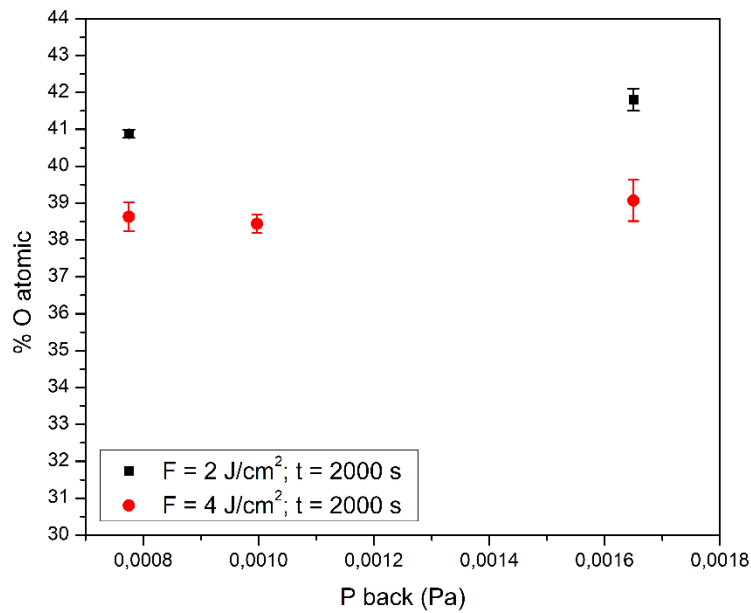


Figure 3.18: atomic oxygen concentration in titanium films as a function of background pressure keeping fixed the value of fluence and deposition time.

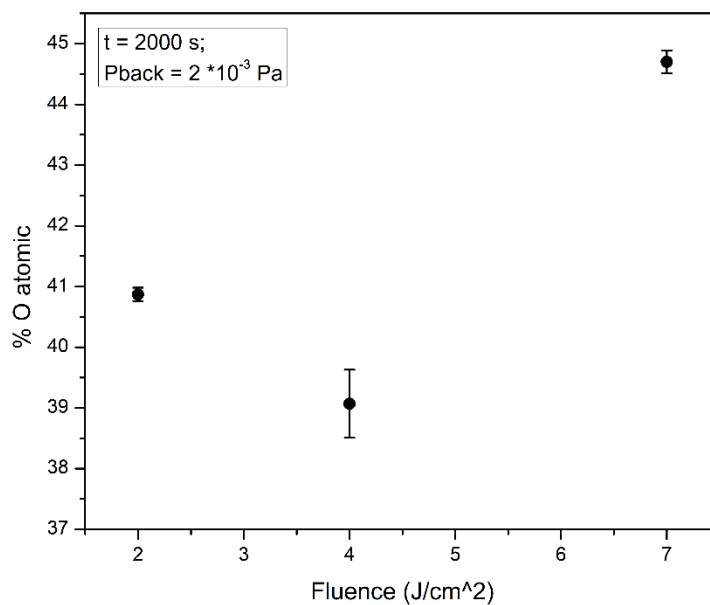


Figure 3.17: atomic oxygen concentration in titanium films as a function of fluence, keeping fixed the values of deposition time and background pressure.

Differently from the previous parameters, the deposition time seems to have a clear correlation with the quantity of oxygen detected in the film. From the plots below it is important to point out that the quantity increases with high speed in the first part of the deposition, while after long times the rate of oxygen intake decreases and tend to stabilize to an equilibrium value. The conclusion that can be derived is that depositing for “infinite” time the content of oxygen remains below 50% and the film looks metallic and non-oxidised. In Figure 3.19 we represented the data only for the same values of fluence and background pressure. Almost the same trend is confirmed also in Figure 3.20, where we plotted the variation of oxygen concentration with deposition time irrespectively of the difference in fluence and background pressure in each sample. This is the confirm that deposition time has a stronger influence in tuning the oxygen concentration respect the other two process parameters. The results are plotted until 2000s because with increasing of time the lost in transmittance of the window may affect the measure and may lead to less reliable results.

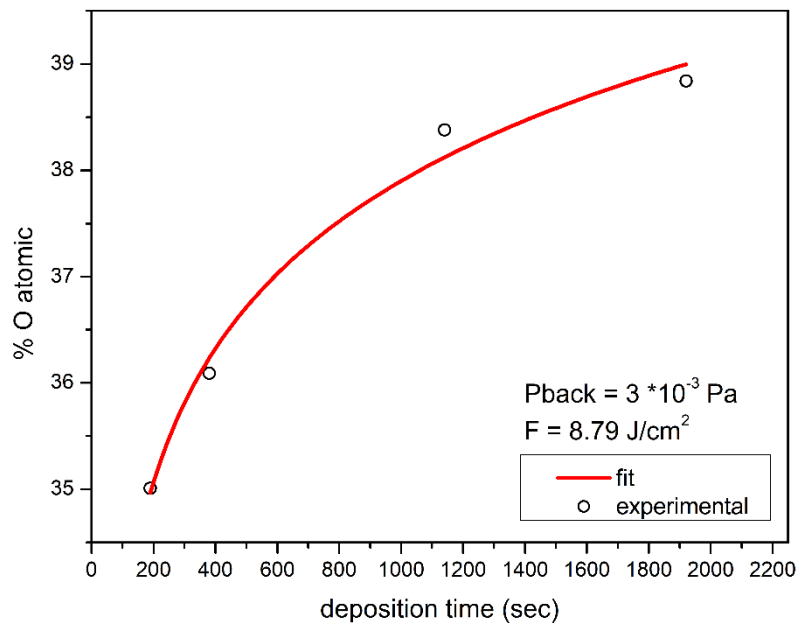


Figure 3.19 atomic oxygen concentration in titanium films as a function of deposition time keeping fixed the value of fluence and background pressure.

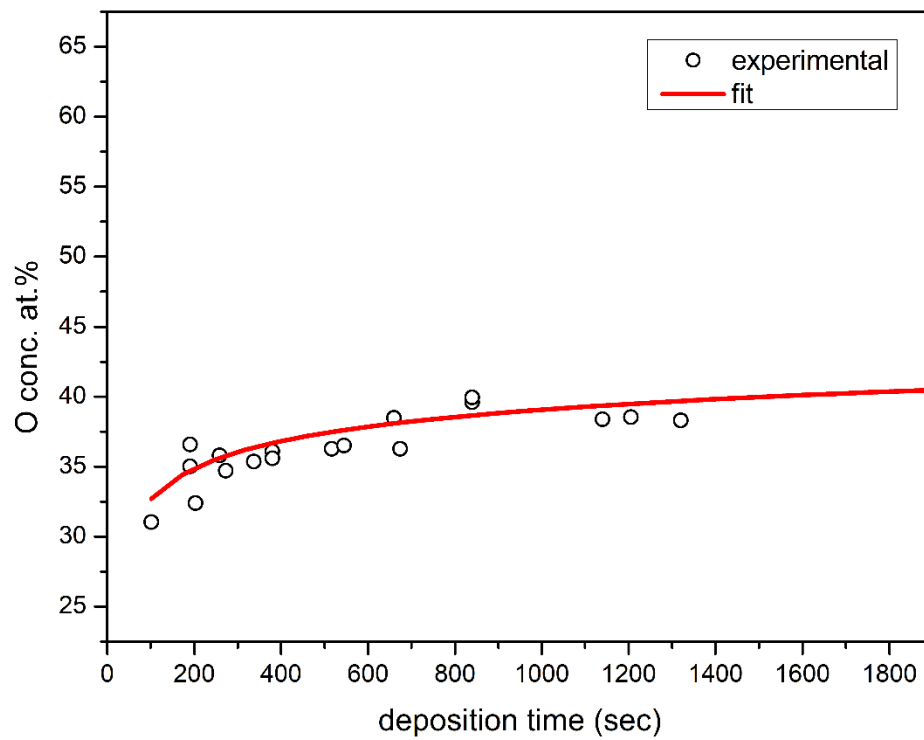


Figure 3.20: atomic oxygen concentration in titanium films as a function of deposition time without keeping fixed the value of fluence and background pressure.

## 4 Investigation on crystal phase stability

This chapter aims at concluding the characterization of Ti thin films investigating on the crystal structure present and on the stabilization of the non-thermodynamic FCC structure. In the following it will be exploited first the XRD analysis of as deposited films, both in  $\theta/2\theta$  and in grazing incidence configuration (GIXRD). Then it will be analysed also the XRD in  $\theta/2\theta$  configuration of the film in post annealing treatments, to see the effect of temperature on the crystal structure. The final part of the chapter will be devoted to the Raman analysis to determine the presence or not of some oxides.

### 4.1. GIXRD analysis

The first part of the analysis will be devoted to study only the GIXRD spectra, because it permits to:

1. Exclude the effect of substrate on the spectra.
2. Allow to detect all the planes families present in the film regardless of their orientation.

To perform an analysis as much as accurate, it will be divided in different steps:

1. Peaks assignment
2. Influence of process parameters on the stabilization of the phases
3. Cell lattice estimation
4. Influence of process parameters on the cell lattice parameters
5. Williamson-Hall analysis

#### 4.1.1. Peak assignment

Firstly, to understand which is the phase of the films it is suitable to compare the reference powder diffraction of known titanium phases with the experimental results. The reference powder diffraction has been extracted from the COD (Crystallography Open Database) for FCC pattern, HCP, Omega and BCC.[69]–[72]

Among the different phases described in the first section, the working conditions ( $T = 298$  K and  $P$  between  $10^{-2}$ - $10^{-4}$  Pa) seem to exclude the possibility of the presence of a BCC (stable at temperature above  $883^{\circ}\text{C}$ ) and Omega (stable at higher pressure) phases. Despite the high quantity of oxygen present in the films, it has shown that also

titanium oxides reference powder diffraction does not match the position of our peaks; it is coherent with the metallic aspect of the samples.

For this reason, we will plot in Figure 4.1 the most significant spectra of our samples and the reference powder of just HCP and FCC titanium phases.

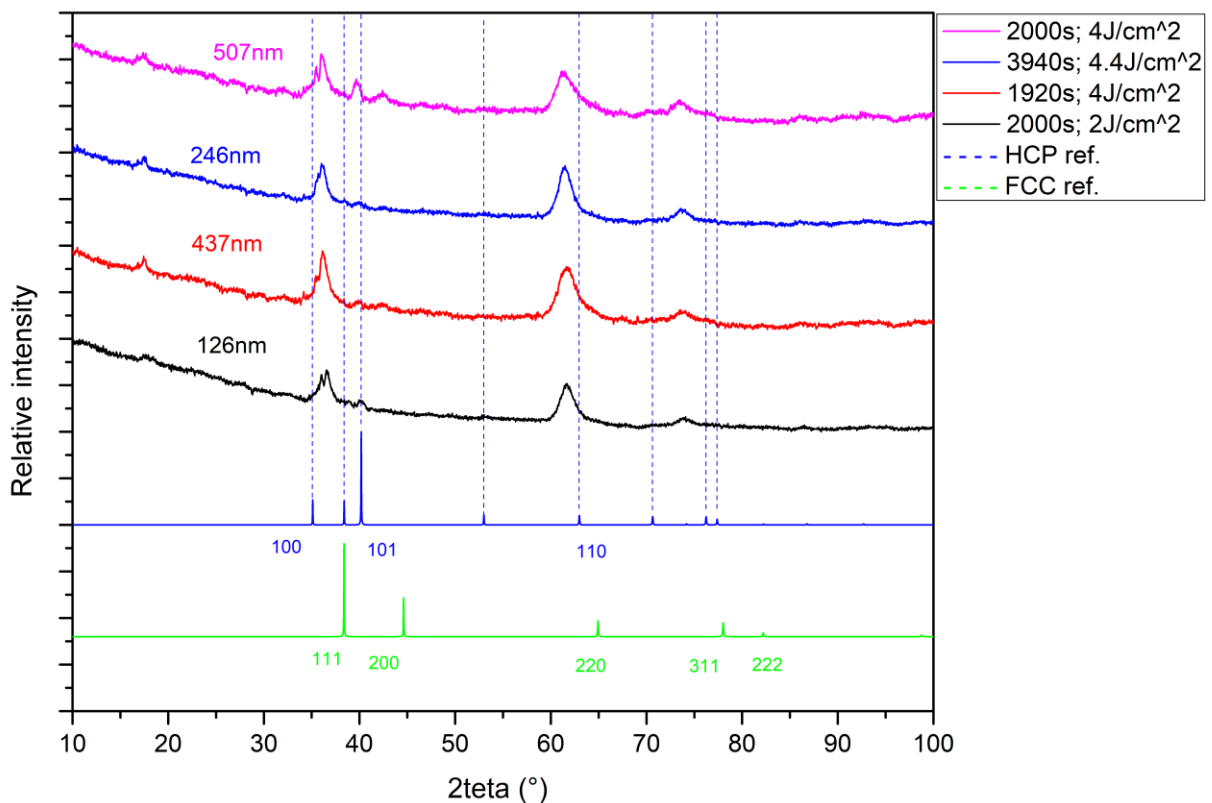


Figure 4.1: GIXRD patterns of titanium films and comparison with HCP and FCC reference powder diffraction. The initial background pressure is not reported, since not relevant.

Some of the peaks are easily attributable to that of HCP phase that almost match the position of our peaks. For what regard the remaining peaks, being in an out of equilibrium regime, dictated by PLD, it is logic to attribute to the presence of a metastable phase, the FCC.

However, as highlighted in the figure 4.2, the FCC pattern does not match the exact position of our peaks.

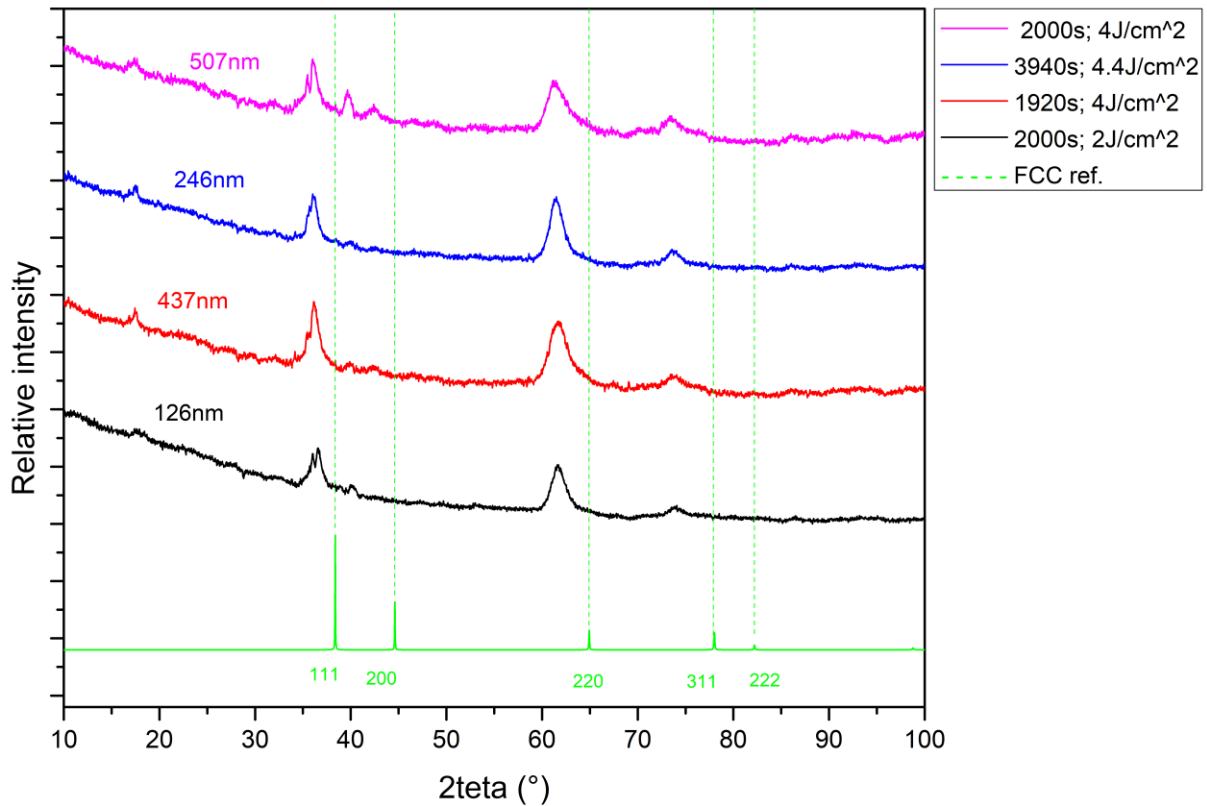


Figure 4.2: GIXRD patterns of titanium films highlighting the mismatch between FCC reference powder and experimental peaks position.

To justify the mismatch between the reference and our sample it can be hypothesised that it occurs due to the presence of impurities (H, O, N) that stabilise the FCC phase. Being present in our samples only oxygen, as impurity, and in large quantity, it is possible to conclude that its presence in the cell may increase its dimension promoting a shift of the peaks toward lower angles.

If the following assumptions hold true, the cell lattice parameter of the FCC titanium should converge to a unique value irrespectively of the peak considered. Applying the Bragg law  $2d\sin\theta = n\lambda$  for each  $\theta$  it is possible to extract the value  $d$  of the distance between planes  $(h,k,l)$  and consequently the value of  $a$ .

After having fitted all the peaks with the same function, it is possible to extract the exact peak position. Usually, the functions that fit better XRD peaks are Lorentz, Gaussian, Pearson 7 and Voigt; in this work, all the peaks have been fitted with the Voigt function.

For each peak position  $2\theta$ , it is possible to derive the interplanar distance.

$$d = \frac{\lambda}{2 \sin \theta} \quad (7)$$

Since the lattice cell is cubic it holds:

$$a = d \sqrt{h^2 + k^2 + l^2} \quad (8)$$

Here is reported the computation, as example, for the first peak of the red sample of Figure 4.2, that corresponds to  $2\theta = 36.18$  with relative plane (1,1,1).

$$2 d \sin \frac{36.18}{2} = n 1.54 \quad (9)$$

For the sake of simplicity  $n$  can be considered as unitary and  $d$  results equal to  $2.48 \text{ \AA}$ . Calculated the distance between plane it becomes straightforward the calculus of  $a$ .

$$a = 2.48 \sqrt{1^1 + 1^1 + 1^1} \text{ \AA} \quad (10)$$

$$a = 4.295 \text{ \AA} \quad (11)$$

Repeating the same calculus for the different peaks it can be obtained the average value of  $a$  and its relative standard deviation.

Table 4.1: scheme of lattice cell value for each peak of red sample (437nm) applying Bragg law

Peaks numeration	experimental peaks position $2\theta$ [°]	h	k	l	experimental a [Å]	a average [Å]	a standard deviation [Å]
1	36.18	1	1	1	4.295	4.264	0.021
2	42.37	2	0	0	4.261		
3	61.73	2	2	0	4.245		
4	73.78	3	1	1	4.254		

Since the values obtained for the different peaks in each sample converge almost to the same value (within the error) and present a very small standard deviation, it is possible to conclude that our initial assumption has been verified and that FCC phase is present in our titanium films.

This has been confirmed also thanks to VESTA, where it has been possible to extract the reference powder diffraction of the FCC titanium imposing the average value of

the lattice cell (4.264 Å), Figure 4.3 [73] . This confirms ulteriorly the presence of the metastable phase hypothesized.

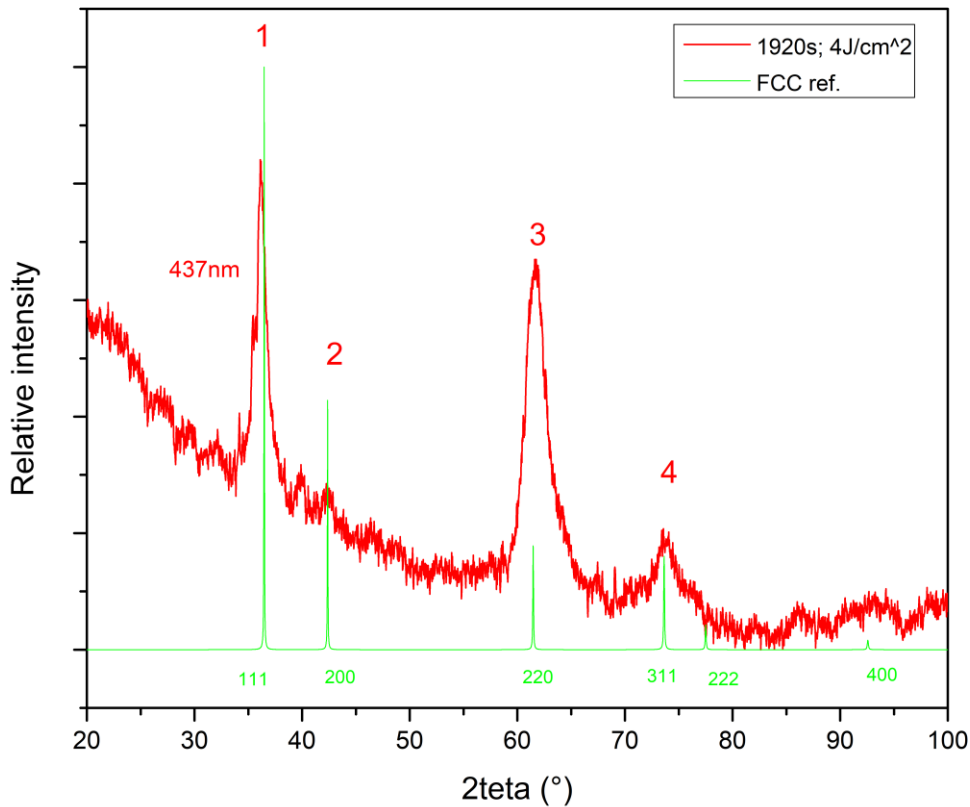


Figure 4.3: Comparison of reference powder spectra of titanium FCC with lattice parameter of 4.264 Å (extracted from vesta [73]) and our sample. The number of the peaks are related to that of Table 4.1.

Thus, it may be concluded that the spectra of our titanium films are characterized by the coexistence of both FCC and HCP phases. In general, the former present peaks with higher intensity and result shifted respect the theoretical pattern. The latter are less evident than FCC one and seem to almost match the theoretical pattern position of HCP phase. The consequence of this is that the main phase is the FCC one, but there is still the presence of a residual HCP phase in which oxygen seems to not be incorporated.

Given the complexity of the XRD spectrum, before to go into the details with the analysis, here is reported a table that resumes the peak assignment for the following sample. Next samples will present just slightly variations in the position of the peak and in the phases present, respect the following.

Table 4.2: peaks and subpeaks assignment of red sample (437nm) of Figure 4.3. The same peaks and subpeaks assignment can be attributed to others sample with slight variations.

Peaks numeration	2 $\theta$ peak experimental	2 $\theta$ peak ref.	Reflected plane	Relative intensity	Phase assigned
1	35.43	35.09	100	24.8%	HCP
	36.18	36.47	111	100	FCC (shifted)
	38.38	38.38	002	25.5	HCP
2	40	40.17	101	100	HCP
3	42.37	42.37	200	47.8	FCC (shifted)
4	61.73	61.47	220	28.4	FCC (shifted)
		62.96	110	15.5	HCP
5	73.78	73.64	311	31.4	FCC (shifted)
		76.20	112	16.8	HCP
		77.37	201	12.0	HCP

The peak 1 is constituted by the presence of a main peak at 36.18° that is FCC and two HCP subpeaks at respectively 35.09° and 38.38° that broaden the global peak with an irregular shape and form some humps. Differently from most of the HCP peaks, the subpeak at 35.09 is a little bit shifted to lower angle respect the reference pattern. The reason may be related to an anisotropic distortion of the HCP lattice cell. The peak 2 and 3 are separate and clearly defined; they are related respectively to the HCP and FCC phase. The peak 4 is constituted by two subpeaks HCP and FCC. The experimental position of the peak is in between the two theoretical reference patterns of HCP and FCC. Since the FCC phase seem to be predominant the peak is more shifted

toward the following. The presence of more than one peak is confirmed by the non-symmetric shape of the peak. The peak 5 is characterized by the presence of three contributions that make it very broad.

#### 4.1.2. Influence of process parameters on the stabilization of FCC phase

The aim of this subchapter is to assess the influence of thickness<sup>3</sup> and gas atmosphere in the stabilization of the metastable FCC phase.

##### 4.1.2.1. Effect of thickness

Since from literature [7], [8], [12], [18] it is noted that titanium films show an FCC phase only until a critical thickness, in Figure 4.4 we want to compare different samples obtained at different thickness.

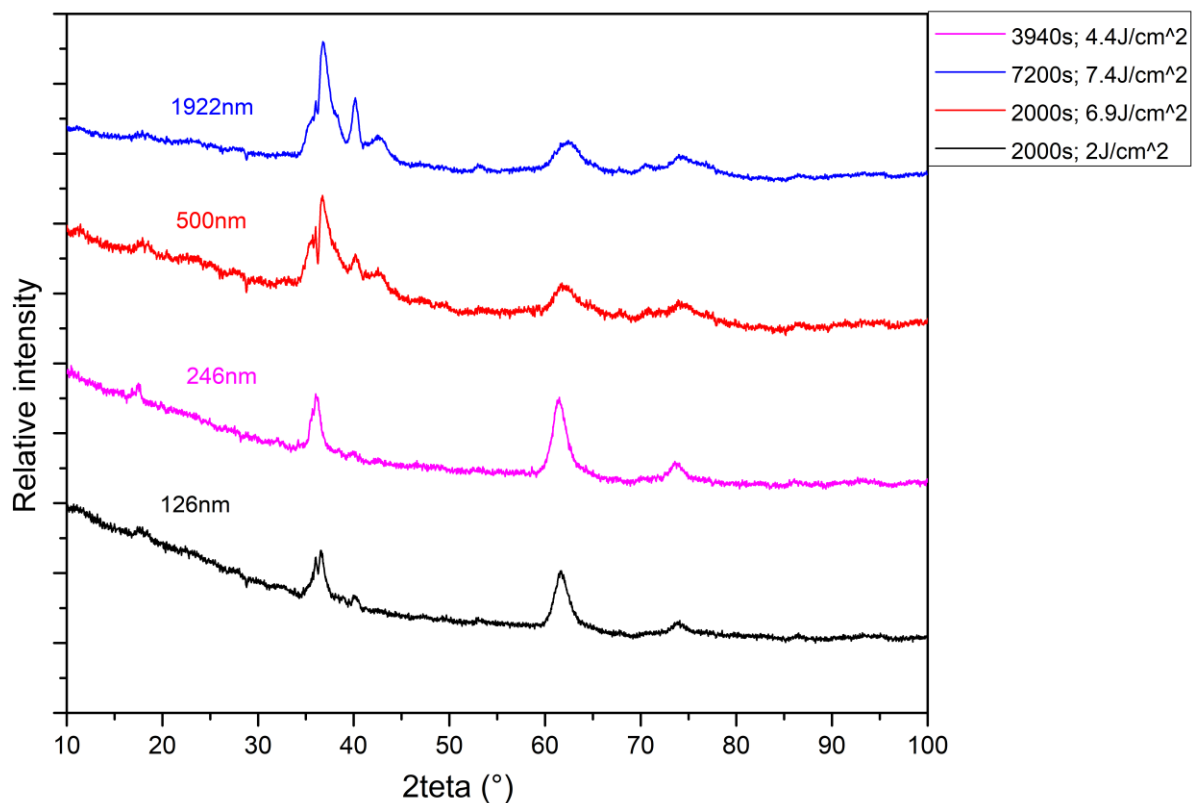


Figure 4.4: GIXRD patterns of titanium films as a function of thickness.

<sup>3</sup> The thickness is not a process parameter, but, as previously described, it depends on fluence rate and deposition time, thus it may be considered here as such.

From the following spectra emerges an important difference respect the samples obtained by other techniques: the titanium films made by PLD display an FCC phase until a thickness of 1922nm. The fact that the system does not come back to the more favorable thermodynamic phase means that the tendency of PLD to form metastable phase is stronger respect to other techniques.

Despite the FCC is shown to be stable until  $2\mu\text{m}$  it is important to note some variations in the spectra that also confirm the fact that the phase of titanium is sensible to the thickness differences. The peaks related to the HCP phase seem to grow in intensity with the increasing of the thickness. This is almost clear observing the increase of the peak around  $40^\circ$  and the decrease of that at  $61.73^\circ$ .

At this point, it becomes interesting to compare the ratio between the area underlined by the main peak of FCC and HCP of each sample. This will permit to calculate in a quantitative way the variation of HCP and FCC phase in each sample. To do it in the most accurate way a deconvolution of the first peak into the three contributing subpeaks is needed. Since our XRD spectra show a non-negligible background noise, we can appreciate the phase fraction variation only qualitatively from the plot.

### 4.1.2.2. Effect of gas

The last two samples have been deposited respectively with 1 Pa of Ar at fluence respectively of  $2.25\text{J}/\text{cm}^2$  and  $7.7\text{J}/\text{cm}^2$ . The introduction of the Ar gas is owed to the attempt to slow down the strong energy regime of PLD, trying to transform it in a closer to equilibrium technique.

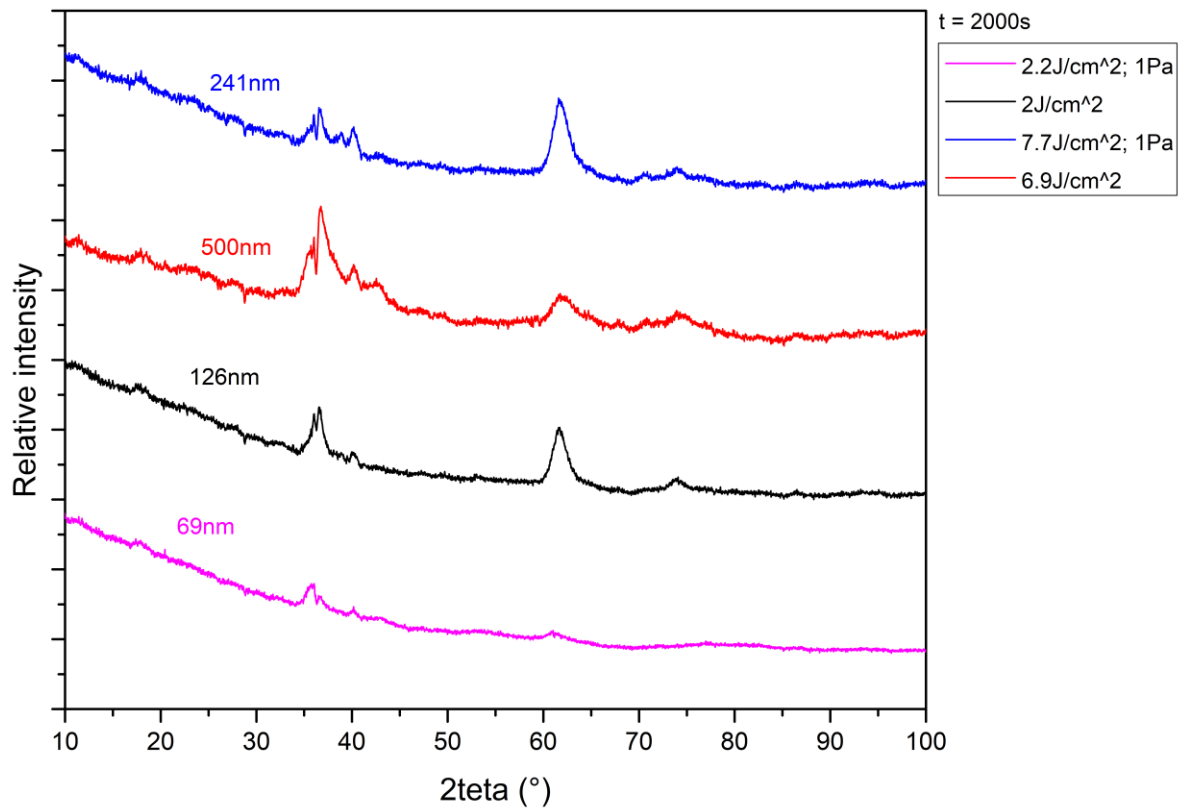


Figure 4.5: GIXRD pattern of titanium films highlighting the effect of Ar atmosphere at different fluences.

From the Figure 4.5 it is evident that at higher fluence rate the FCC phase is stable both in presence and absence of gas. It means that at the following value of fluence the species are highly energetic, and 1 Pa of Ar is almost insufficient to promote the formation of the thermodynamic favoured phase.

Differently, regarding the low fluence samples it is observed a predominance of the HCP peaks and the quasi absence of FCC phase. This permits to conclude that the FCC phase does not display when the energy of the deposited species is too low. It may be interesting to calculate the energy limit below which no metastable FCC phase shows up.

#### 4.1.3. Influence of process parameters in the cell dimensions

Repeating the calculus done it above, it is possible to compute the lattice parameters of FCC structure for each sample. First of all, it is important to point out that all the samples present a  $4.23\text{-}4.28\text{ \AA}$  lattice parameter (with a standard deviation that oscillates between 0.003 and 0.03) irrespectively of the values of deposition time,

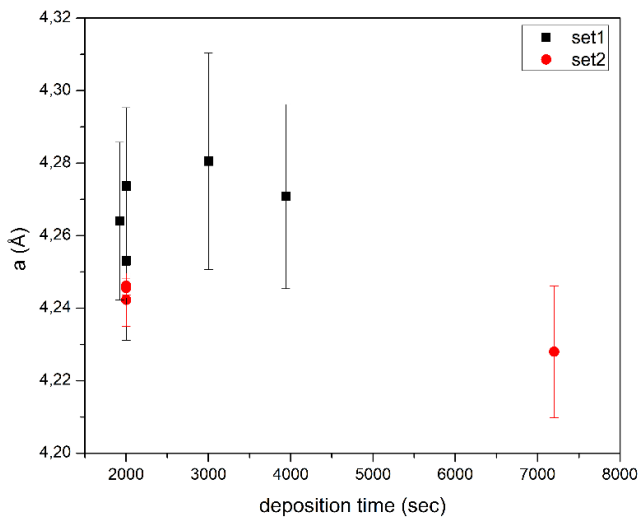
fluence and base pressure. It means that, if the metastable FCC forms, thus the cell will present almost the same dimensions with a certain reproducibility.

In the two set of deposition handled by me, it has been observed that the standard deviation of the first set is always around 0.03, while in the second it is almost in the range of 0.003. The reasons of this ununiformity may be related either to a more accurate diffraction analysis or to the variation of the window used in the deposition. In fact, in the second set of deposition has been employed a completely new window, probably less incline in the loss of transmittance, leading to a more accurate results. For this reason, it has been decided to show the variation of the influencing parameters in the dimension of lattice cell for respectively the first set and the second set of depositions.

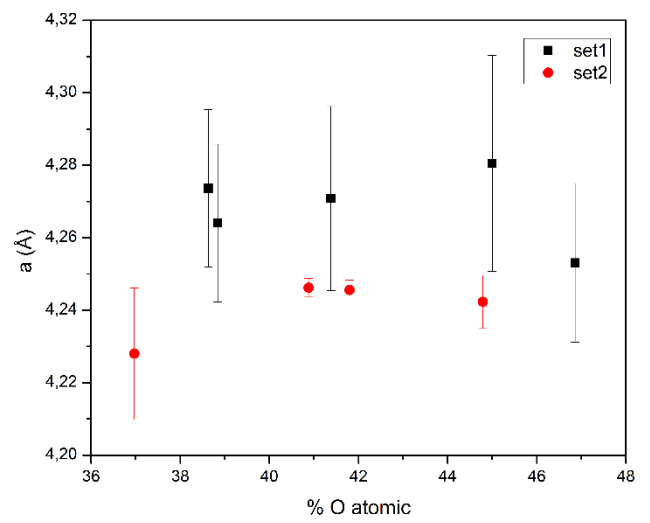
From Figure 4.6 (next page) it is possible to observe that variation of the lattice cell with respect the following parameters is almost negligible. Despite the strong reproducibility of the dimension of lattice cell it is possible to observe the slight influence of the parameters just in the second set. In particular it may be concluded that the lattice cell slightly decreases (almost within the error values) with the thickness of deposited film, fluence rate and deposition time; it is coherent with the fact that thickness is directly proportional to fluence and deposition time.

On the other hand, the effect of oxygen concentration is opposite respect the previous ones. This may be considered as a confirm of the fact that increasing the quantity of oxygen increase the dimension of the cell. However, after a certain value, the lattice cell seems to be constant with the increase of oxygen in the film. If the oxygen quantity does not promote an increase of the volume cell it may be mean that this excess of oxygen may be related to the segregation of oxides at the grain boundaries or at the surface of the film. For this reason, it will become crucial in the next chapter to investigate Raman spectra.

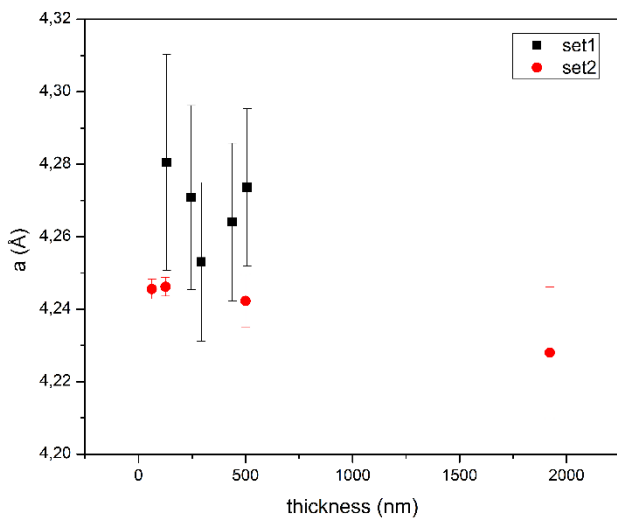
The effect of background pressure also here has not been reported since does not have a clear influence on the dimension of the cell.



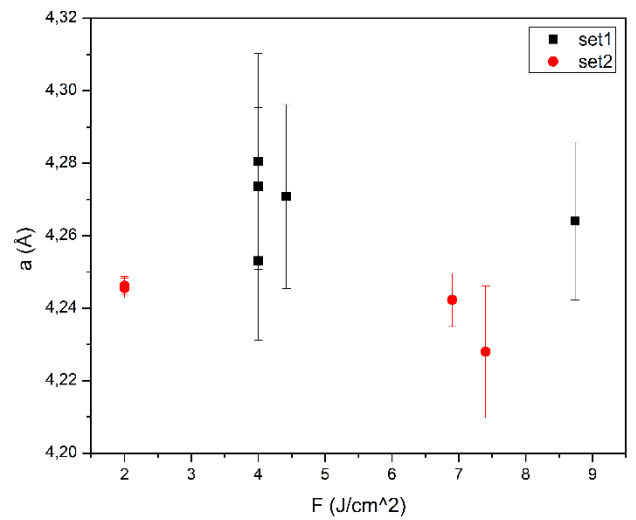
a)



b)



c)



d)

Figure 4.6: lattice parameter variation in the two set of deposition with respect:

- (a) deposition time.
- (b) atomic oxygen concentration in the film.
- (c) thickness of the films.
- (d) fluence rate.

#### 4.1.4. Williamson-Hall analysis

Since the GIXRD provide us lots of peaks for each sample it can be thought to perform a Williamson-Hall analysis. According to Scherrer formula the broadening of the peaks is related only to crystallite size, but it doesn't give any info regarding the microstructure of the lattice. Williamson-Hall is a method that aims to reconsider the broadening effect, considering also the microstrain present in the lattice cell. Among the different models, in this chapter we will focus on the Williamson-Hall under uniform deformation model. The following is based on the hypothesis of uniform strain along the crystallographic direction. [74]

The broadening  $\beta$  and the position of each peak are correlated by the following relation:

$$\beta \cos \theta = \frac{K \lambda}{\tau \cos \theta} + 4 \varepsilon \sin \theta \quad [74] \quad (12)$$

$\tau$  = crystallites size;

$\varepsilon$  = microstrain;

$\beta$  = FWHM;

$2\theta$  = peak position.

Imposing  $y = \beta \cos \theta$  and  $x = 4 \sin \theta$ , it turns out a linear relation that permit to calculate the microstrain  $\varepsilon$  as the slope of the line and the crystal domain  $\tau$  as intercept. The reason why the following method is adopted is because, differently from the Scherrer one, it can predict also the microstrain of the lattice film, that cannot be considered negligible in the PLD due to the high energy involved in the species deposited.

Thanks to the variation of position and FWHM of each peak, it may be estimated the size of the crystal domain and the microstrain of the lattice. Since the following method is based on a linear regression, the XRD spectra must present at least three clearly defined peaks for each specific phase present in the film. For this reason, in this subchapter, we will focus only on the crystallite's dimensions and microstrain related to FCC phase. The residual HCP phase present too few peaks and is difficult to be analysed with this method.

The procedure followed to extract the value of crystal domain and microstrain is:

1. Fit the FCC peaks with a Voight function.
2. Extract the FWHM and the centre position of the function.
3. Impose  $y = \beta \cos \theta$  and  $x = 4 \sin \theta$ .

4. Represent in a plot the  $(x,y)$  for each peak and extract the slope and the intercept with y axis.
5. The slope will give us information on the microstrain, the intercept on the crystal domain.

Among the different FCC peaks, below represented, the analysis has been performed only for the reflection plane (111), (220), (311) (described in Table 4.2) because they exhibit a more defined shape and can be fitted better.

The peaks related to the other reflections are excluded because cannot be fitted due to the small intensity and the low signal to noise ratio. To may perform an accurate fit XRD spectra with higher signal-to-noise ratio are required. For this reason, the deconvolution in multipeak has not been possible and all the peaks are fitted with a single peak approximation.

In the following we resume the procedure step by step for the calculus of microstrain and crystallites dimensions for the sample in red of 437nm of Figure 4.2.

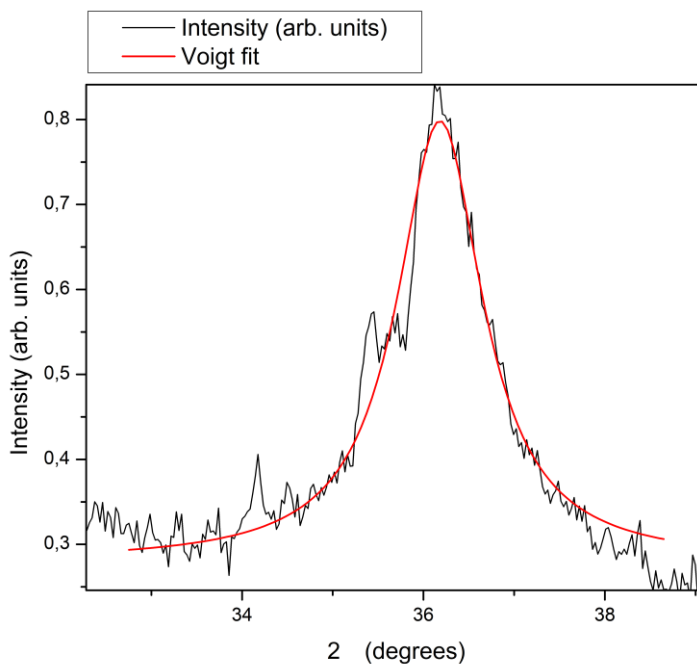


Figure 4.7: fit of the main peak at  $36.18^\circ$  (Table 4.2) of red sample in the assumption of single peak fit.

From the following fit the software provides us the following parameters: peak position,  $w_G$  (Gaussian width),  $w_L$  (Lorentzian width) and  $R^2$ . From  $w_G$  and  $w_L$  it is possible to compute the global width of the function at half height, known as FWHM.

Table 4.3: scheme of the calculus of (x,y) to perform Williamson-Hall analysis.

Peak position	$w_G$	$w_L$	$R^2$	$\beta$	x	y
36.18°	0°	1.31°	0.96°	1.31°	1.24	0.02

$$FWHM = 0,5346 * w_L + \sqrt{0.2166 w_L w_G + w_G w_G} \quad (13)$$

$$FWHM = \beta = 1.31^\circ$$

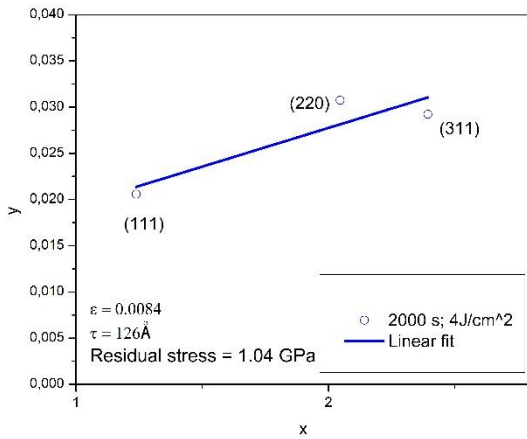
K expressed in the above equation is the Sherrer constant, equal to 0.9 [70];  $\lambda$  is the wavelength of X-ray equal to 1.541Å.

Calculated the values of the microstrain ( $\beta$ ) and of the crystallites dimension, it is possible to derive the residual stress to which each film is subjected, knowing the elastic modulus E of FCC phase. According to literature data [69] the elastic modulus is of 123.92GPa.

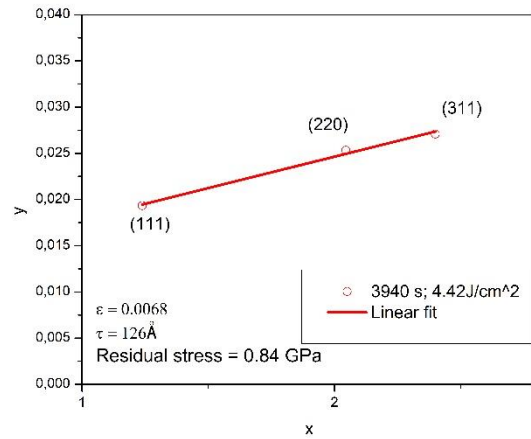
The residual stresses, in the elastic approximation, can be calculated as

$$\sigma = E \varepsilon \quad (14)$$

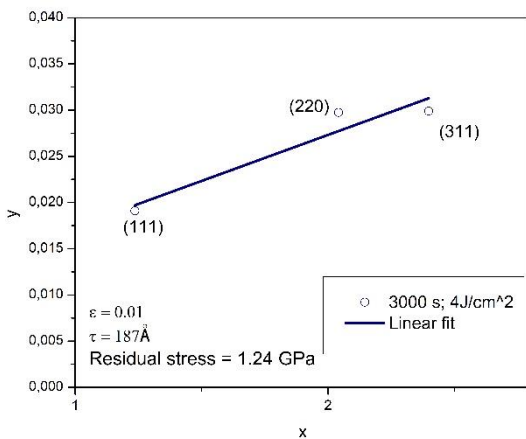
The same reasoning is repeated for all the sample obtaining the following results:



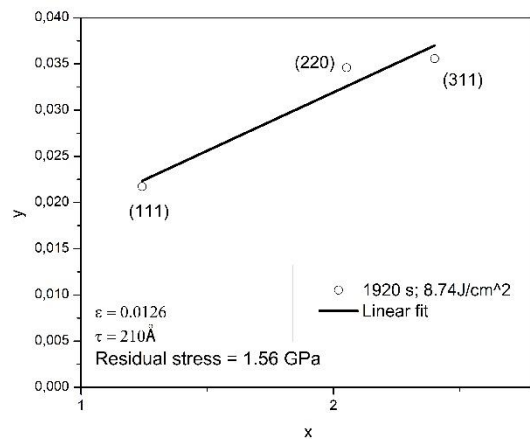
a)



b)



c)



d)

Figure 4.8: Williamson-Hall analysis for different samples at different conditions highlighting the values of microstrain  $\varepsilon$  and grain dimensions  $\tau$ .

In accordance with the previous results also the microstrain and crystallites do not show substantial differences in the different samples. The only small difference that can be observed is the microstrain variation with the fluence.

## 4.2. XRD in $\theta/2\theta$ configuration analysis

To have a more general view of the phase present in the titanium films, have been performed XRD in  $\theta/2\theta$  configuration of the samples before and after annealing.

Even if under this configuration the spectra obtained are strongly influenced by the presence of the substrate, the aim of this analysis is to confirm the presence or not of the phases previously discussed.

Since the main peak related to the FCC structure of titanium is around  $36^\circ$ , as previously seen in the 4.1, the following spectra have been analysed only between  $30^\circ$  and  $60^\circ$ .

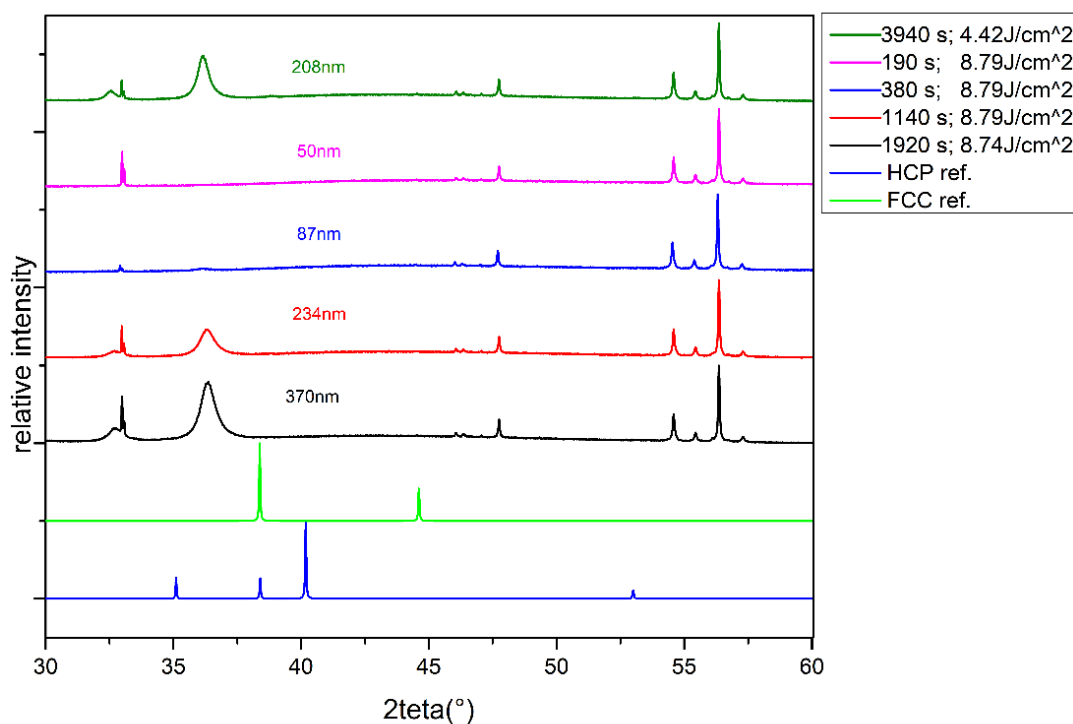


Figure 4.9: XRD pattern in  $\theta/2\theta$  configuration of most significant samples. The black and red spectra have been analysed also in Figure 4.1 by GIXRD analysis.

The XRD spectra of Figure 4.9, confirm the existence of a peak at  $36^\circ$  that, thanks to the analysis previously done, may be related to the FCC phase. The other peaks present are clearly not related to titanium films, but they are present due to the influence of

the Si (100) substrate, in fact they do not change neither in shape nor in intensity according to the different process conditions and thicknesses. The first important conclusion that can be derived from the spectra is the absence of HCP residual phase respect the previous GIXRD spectra. The first hypothesis that can be done is that the HCP crystallites present in the titanium films exist, but they are not detected in this configuration because of the orientation of the crystal plane is not parallel to the film geometrical surface. XRD in the Bragg-Brentano configuration is not able to detect the crystallites oriented randomly, but just that parallel to the film area. TEM analysis may permit to confirm the orientation and the distribution of the different phases present in the films.

The second important observation that can be done is that not all the samples show the FCC phase of Ti.

At first impact, from Figure 4.9, the reduced thickness appears to be the primary cause of the absence of peaks, as the XRD experiment performed in the given configuration may have some problems in investigating excessively thin film. However, Figure 4.10, where all samples lacking the FCC phase in the XRD  $\theta/2\theta$  are grouped, contradicts this eventuality. The sample of 400 nm, despite its non-reduced thickness, exhibits a much weaker FCC peak respect the other samples with the same thickness. The exceedingly low intensity suggests the presence of another parameter, in addition to the presence of gas at small fluence, that may hinder the formation of the following metastable phase.

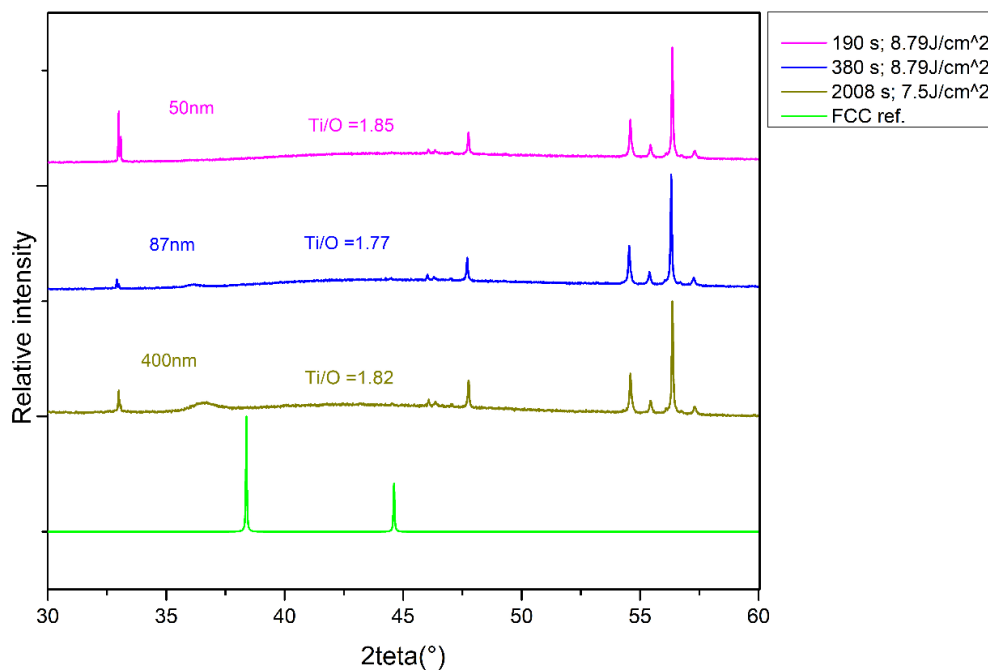


Figure 4.10 XRD patterns in  $\theta/2\theta$  that do not show evident FCC phase peaks.

#### 4.2.1. Influence of Ti/O ratio on stability of FCC phase

Since in literature [27] the Ti/O ratio have been shown to have influence on the stability of the described phase it may be considered the effect of the Ti/O ratio in the film.

According to Tshwane [27] FCC phase is stable for a  $0.77 < \text{Ti/O} < 1.66$ . Differently from the samples characterized by grazing in 4.1, that present a ratio included in the range, all the samples of Figure 4.10 present a Ti/O ratio out of range. If for samples of 50nm and 87nm the absence of FCC phase may be related to the low thickness, the same cannot be said for the sample of 400nm. Therefore, it is possible to assume that the absence of FCC peaks is owed to an out of range of Ti/O ratio, experimentally confirming those results that were based only on first principle calculations[27].

Now that we have verified that the samples above the range of validity proposed by Tshwane do not show FCC crystal structure it becomes interesting to observe if there occur any variation in the fraction of FCC crystallites within the range of validity and if the lower limit value is confirmed too. For the study of the phase fraction variation as a function of Ti/O ratio will be considered only the sample in  $\theta/2\theta$ , because respect that in grazing configuration, can be fitted with higher accuracy due to the presence of more defined peak and a high signal to noise ratio. However, the presence of a single peak and only a single phase does not permit to make a ratio of the intensity of the FCC peak respect the HCP with the variation of Ti/O. Taking into account this fact, to see among the samples which one has a predominant FCC phase it has been calculated the ratio between the integral area underlying the peak and the thickness of the sample. The reason why of this normalization is related to the fact that, higher thickness implies higher signal and larger peaks. Actually, the normalization should take into account also the density, but since the samples are deposited in similar conditions and PLD forms compact film with high reproducibility, it may be neglected. Unfortunately, being not present samples with a concentration of oxygen between 0.77 and 1.30, we limited our analysis to range between 1.33 and 1.60.

Figure 4.11 shows that the trend is not monotonic but seems to reach a maximum around 1.57 and then rapidly decreasing approaching the upper limit. Since also toward lower Ti/O ratio it is visible an important decrease, the following plot may let us assume that the experimental range for titanium films produced by PLD has a lower limit around 1.3 and an upper one around the position proposed by Tshwane. It means that, in the assumption that the quantity of oxygen present inside HCP cell is negligible due to the non-shift of the peaks, the Ti/O calculated represents the ratio between the number of atoms of Ti and of oxygen in the FCC crystal structure. Since the number of atoms of Ti in an FCC cell is 4, the relative number of oxygen atoms that stabilise the non-thermodynamic phase should be of 2.5-3. It is possible to conclude that 3 atoms of oxygen are required to stabilise FCC phase of titanium.

Therefore, it may be attempted to tune the quantity of oxygen (knowing its dependence with time, paragraph 3.3.1) to obtain different values of Ti/O ratio in the interval between 0.77 and 1.30, and so verifying the same in the other part of the interval.

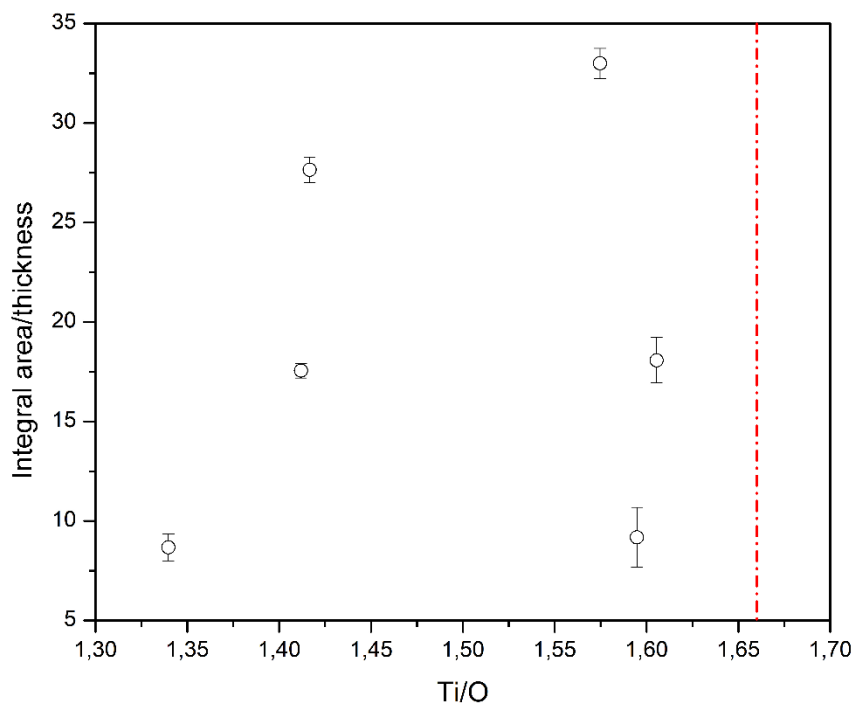


Figure 4.11: Fraction of FCC phase in the film according to different Ti/O ratio. In red the upper limit proposed by Tshwane [27] over which no FCC phase is expected

#### 4.2.2. Influence of parameters in the cell dimension and Scherrer

The presence of only a single peak in the in  $\theta/2\theta$  spectra makes the analysis less reliable respect that performed before for grazing incidence in 4.1.3. Despite the calculation of the cell dimension is based only on a single peak and therefore the

absence of error bars, all the samples present a lattice parameter between 4.27-4.30 Å, confirming the high reproducibility previously seen.

To complete the analysis of the following spectra it should be calculated also the grain dimensions. Differently from the spectra obtained in grazing, in this case Williamson-Hall analysis cannot be performed due to the presence of a single peak only. Even if less accurate, it is still possible to adopt the Scherrer formula.

$$\beta \cos \theta = \frac{K \lambda}{\tau \cos \theta} \quad [74] \quad (15)$$

$\tau$  = crystallites size;

$\beta$  = FWHM;

$2\theta$  = peak position.

In the assumption to not consider the strain present in the lattice, it is possible to estimate the value of the grain dimensions according just to the intensity and shape of the peak, equation xx.

Table 4.4: grains dimensions and cell dimensions of peaks obtained at different conditions.

Deposition time (s)	Fluence J/cm <sup>2</sup>	a (Å)	$\tau$ (grain dimension) (Å)
1920	8.74	4.273	121
1140	8.79	4.279	125
3940	4.42	4.297	160

From a parallel work it has been calculated that the dimensions of the grains of FCC Ti films deposited with HiPIMS is of 50-60Å. Therefore, it may be concluded from this analysis that PLD seems to promote the growth of bigger grains respect HiPIMS.

### 4.3. Crystal structure investigation post annealing

After having performed an accurate XRD analysis both in grazing and in  $\theta/2\theta$  we have concluded that PLD stabilize the non-thermodynamic FCC phase in most of the cases thanks to its high energy regime and to its pulsed nature.

However, in the attempt to restore the system to a thermodynamic equilibrium condition, it was decided to analyse XRD spectra in  $\theta/2\theta$  configuration after the increase of temperature in vacuum, annealing.

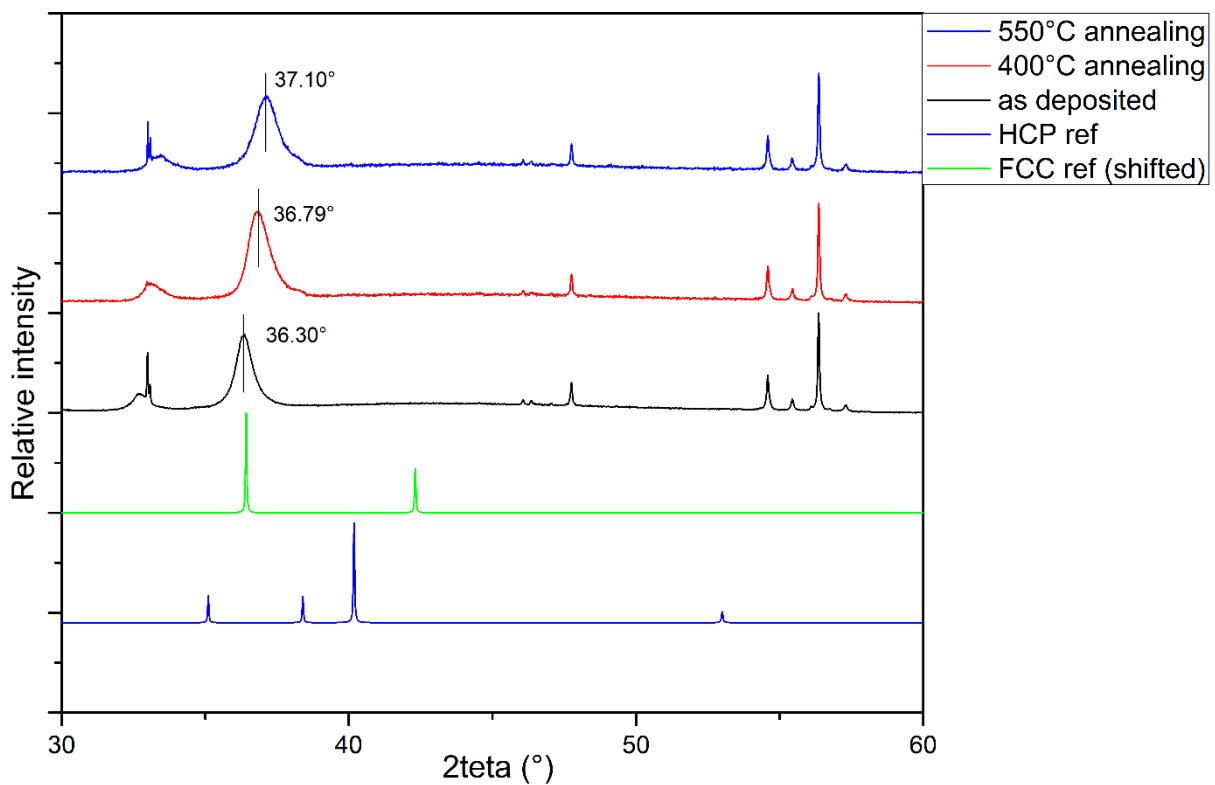


Figure 4.12: XRD patterns of annealed samples, highlighting the variation of crystal structure at different annealing temperature.

From Figure 4.12 it emerges that the FCC peaks is preserved also after the annealing at higher temperature. However, it is important to highlight the shift toward higher angle, and the relative decrease in the cell dimensions, according to higher

temperature. The reason for this may be attributed to release of residual stresses and the possible migration of oxygen from the cell leading to a redistribution in the film.

#### 4.4. Raman analysis

The aim of this chapter is to confirm the metallic evidence of our films, despite the relevant quantity of oxygen present.

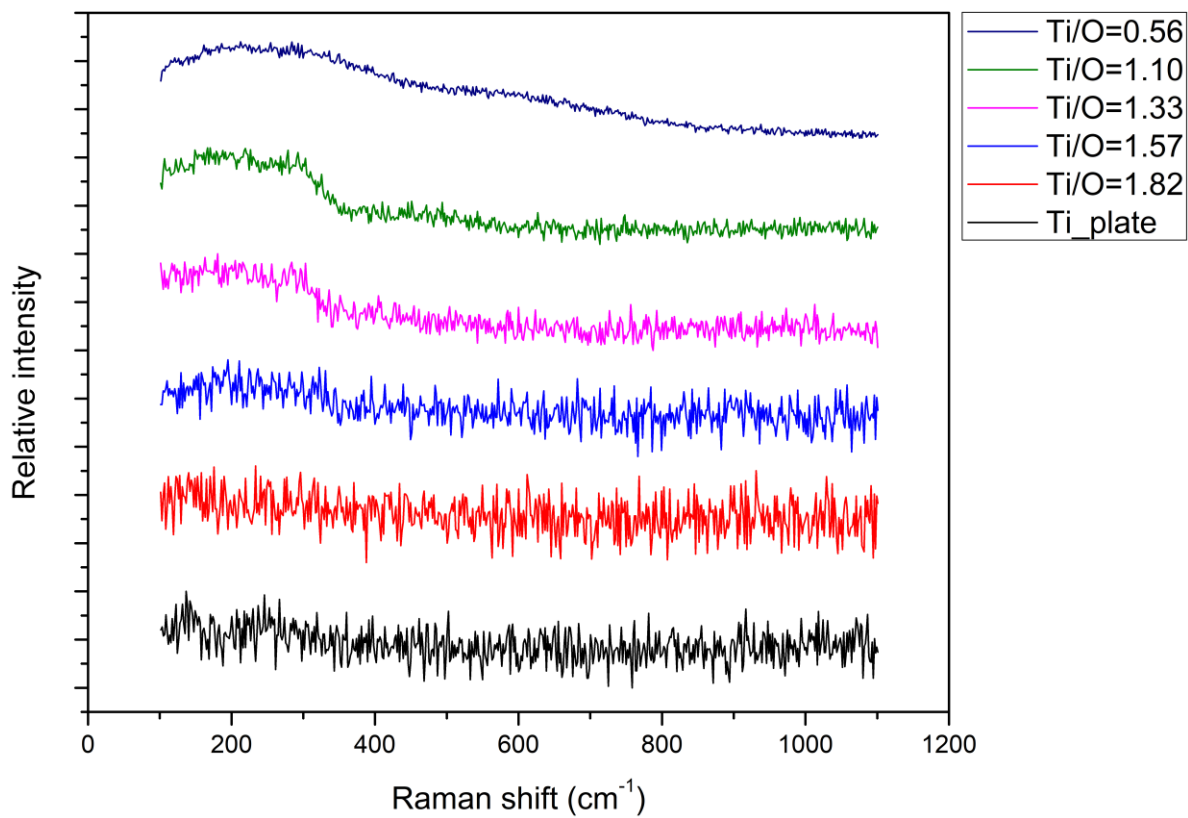


Figure 4.13: Raman analysis of samples with different ratio of Ti/O. All the measurements are normalized to 1.

The titanium plate is displayed to confirm that no signal is present, as in all the metal films. From the bottom part of the Figure 4.13 toward the upper one it has been highlighted the gradual variation of the signal according to an increase of oxygen concentration. The samples that present a Ti/O ratio lower than 1.33 show the presence of a broad band below  $400\text{ cm}^{-1}$ . This seems to be a peculiar feature of PLD films, due to the possible presence of amorphous oxide. Furthermore, from Figure 4.13 it is important to point out also that the band of the sample in blue with a Ti/O ratio equal to 0.56 shows a completely difference shape respect the other. The following sample has been produced in oxygen atmosphere (3 SCCM  $\text{O}_2$ ) to expressly promote its relative oxidation; the sample is visibly oxidised with a non-metal chromatic appearance. The oxidised sample seems therefore to be characterized by a different amorphous oxide respect the previous ones, it is highlighted better in Figure 4.14.

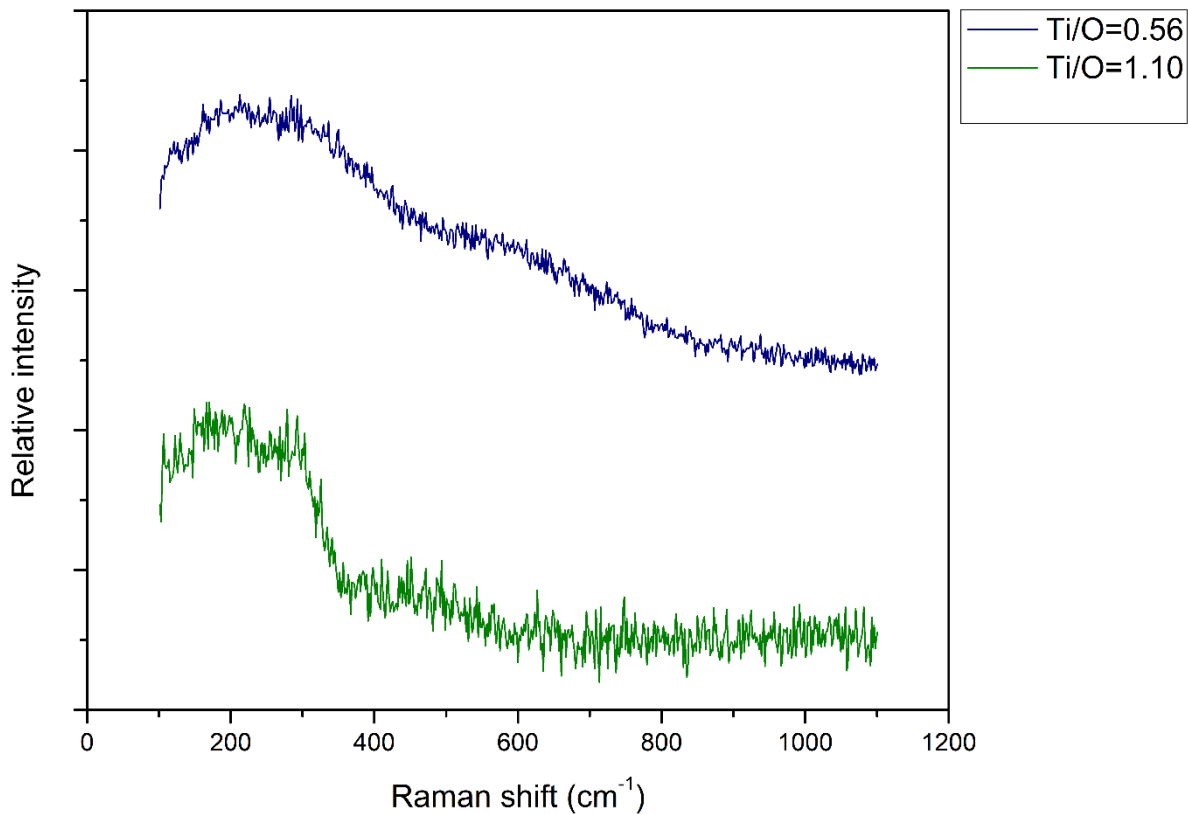


Figure 4.14: magnification of Figure 4.13, highlighting the different behaviour of the oxidized sample respect the non-oxidized one.

Despite the different working conditions, a similar band formation has been put in evidence by the work of Bricchi and Mascaretti [75], [76] who deposited oxynitride

films by PLD. In view of this results, it is possible to conclude that Raman does not display the typical peaks of  $\text{TiO}_2$ , but a broad band below  $400\text{ cm}^{-1}$ , symptom of amorphous oxides presence and of vibrations of Titanium-Oxygen atoms

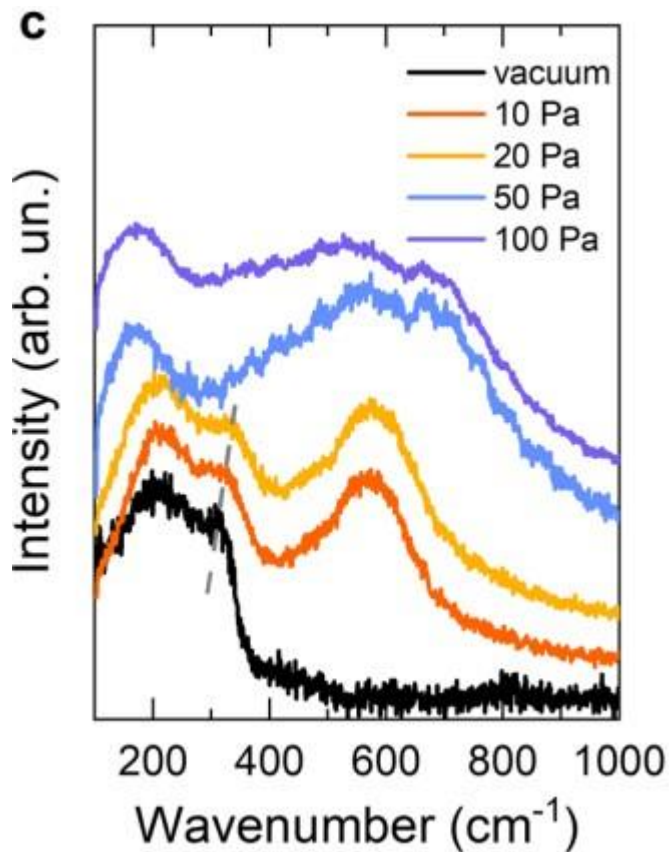


Figure 4.15: Raman spectra of oxynitride films deposited in vacuum and at 10–100 Pa of  $\text{N}_2/\text{H}_2$ . [75]



## 5 Conclusions and future developments

This thesis has focused on the synthesis and characterization of metastable FCC phase of thin titanium films by PLD. In the research scenario about the stabilization of non-thermodynamic phases of titanium obtained by DC [18],[7], HiPIMS [7], vacuum arc discharge [8] and epitaxial growth [12], the following work contributes with important conclusions that can be exploited as the starting point for future developments.

Based on a XRD analysis, both in grazing and in  $\theta/2\theta$ , the first important conclusion of this thesis work is that, differently from other high techniques, previously cited, where the FCC phase has been stabilised until 700nm, the PLD plays an important role in the stabilization of the following phase until 2 $\mu$ m irrespective of the values of fluence rate (2-10 J/cm<sup>2</sup>), initial background pressure ( $5 \cdot 10^{-4}$ - $1.20 \cdot 10^{-2}$  Pa) and deposition time (100-7200 sec). Even if the metastable phase is always accompanied by the presence of the thermodynamic favoured HCP phase, the samples show to be sensible to thickness variation. It has been illustrated that increasing the thickness, diffraction signals originating from HCP phase has become more intense but without suppressing the metastable one.

The effect of the stabilization of FCC phase at also higher thickness is owed to the higher tendency of PLD, compared to other high deposition energy techniques, to form metastable phase. In 4.1.2.2 has been demonstrated the vanishing of the FCC phase when the fluence rate is small (2 J/cm<sup>2</sup>) with a simultaneously presence of Ar gas (1Pa). The following working conditions has been defined with the aim of reducing the energy regime of the species and to transform PLD in a closer to equilibrium technique. It means that below a certain energy threshold the metastable phase does not form. Furthermore, it has been investigated any possible crystal structure modification for samples that undergone post deposition annealing process with the aim to carry the system at the thermodynamic equilibrium. However, from XRD analysis of the annealed samples do not emerge evident phase transformations, but only a slight variation of the cell dimension due to the release of residual stresses and possible migration of oxygen from the cell and a consequent redistribution in the film.

PLD dynamic is not the only influencing factor on the stabilization of the phase, but it is important to also highlight the role of oxygen concentration in the film and the relative Ti/O ratio. It has been demonstrated in 4.2.1 that, in accordance with theoretical studies [27], the metastable phase is evident for a specific range of Ti/O

ratio. For this reason, the concentration of oxygen in the film becomes of crucial importance in the stabilization of FCC phase and in the expansion of lattice cell. Differently from the theoretical values, around  $4.10 \text{ \AA}$  [26], the dimension of the lattice parameter in this work has been observed to be of  $4.22\text{-}4.30 \text{ \AA}$ , in pretty accordance with the experimental values reported in Table 1.2 [27].

Another important result related to the oxygen concentration in the film has been obtained from EDXS that show a considerable amount of oxygen, above 30% in all the samples. Despite the high quantity present, it has been checked both visually and at Raman that the titanium films are metallic.

Regarding the effect of the different process parameters on the chemical, morphological and microstructural properties (cell dimension, grain size, residual stress) it is concluded that they do not strongly affect the following film properties confirming the high reproducibility of PLD. To reach coherent results and to avoid any undesirable loss in transmittance it must be performed a cleaning of the window after each deposition.

After the XRD analysis in different configurations, this thesis work can be taken as a starting point for future developments. The new prospective advancements concern both depositions in new working conditions and also more accurate characterization analysis.

In the first case it can be interesting to:

- Deposit titanium on different substrates with different crystal structures to observe if this may influence the growth modes. The epitaxial growth is usually favoured in presence of a heated substrate and only for small thickness values (lower than 100nm).
- Deposit titanium at different Ar pressure to observe the variation of the film properties.
- Deposit titanium on top of a heated substrate at different temperatures, to compare the results with that of annealing and to observe if the temperature variations have some influence in the transformation of the crystal structure from FCC to HCP and in the cell dimensions.
- Deposit other HCP metals with a similar electronic configuration of Ti, such as Zn, in order to spot possible differences.
- Calculate the exact kinetic energy of the deposited particles with variation of working conditions to permit to define an almost exact value of energy below which FCC phase does not form.

For what regard the characterization analysis it can be:

- Performed a Rietveld analysis to obtain more phase crystal properties and with high accuracy.
- Performed a TEM analysis observing the formation and growth of the different phases.
- Perform XPS to obtain additional chemical information.
- Performed resistive/optical measurements at different oxygen concentrations in the film to evaluate the loss of metallic properties.
- Performed an accurate Raman analysis on a larger set of samples aimed at clearly defining the cause of the broad band formation and its variation according to the different process parameters.

To conclude, even if a complete understanding of the subject has not been achieved, the following work thesis has led to important results that can be considered as a starting point for the synthesis and characterization of FCC metastable phases titanium films.



## Bibliography

- [1] C. Leyens and Peters, *Titanium and Titanium Alloys: Fundamentals and Applications*.
- [2] A. Aguayo, G. Murrieta, and R. de Coss, "Elastic stability and electronic structure of fcc Ti, Zr, and Hf: A first-principles study," *Phys Rev B Condens Matter Mater Phys*, vol. 65, no. 9, pp. 921061–921064, Mar. 2002, doi: 10.1103/PhysRevB.65.092106.
- [3] M. Geetha, A. K. Singh, R. Asokamani, and A. K. Gogia, "Ti based biomaterials, the ultimate choice for orthopaedic implants – A review," *Prog Mater Sci*, vol. 54, no. 3, pp. 397–425, May 2009, doi: 10.1016/J.PMATSCI.2008.06.004.
- [4] P. Wang, M. Todai, and T. Nakano, "Beta titanium single crystal with bone-like elastic modulus and large crystallographic elastic anisotropy," *J Alloys Compd*, vol. 782, pp. 667–671, Apr. 2019, doi: 10.1016/j.jallcom.2018.12.236.
- [5] S. K. Sikka, Y. K. Vohra, and R. Chidambaram, "OMEGA PHASE IN MATERIALS," 1982.
- [6] B. S. Hickman, "The Formation of Omega Phase in Titanium and Zirconium Alloys: A Review," 1969.
- [7] D. Dellasega, F. Mirani, D. Vavassori, C. Conti, and M. Passoni, "Role of energetic ions in the growth of fcc and  $\omega$  crystalline phases in Ti films deposited by HiPIMS," *Appl Surf Sci*, vol. 556, Aug. 2021, doi: 10.1016/j.apsusc.2021.149678.
- [8] M. Fazio, D. Vega, A. Kleiman, D. Colombo, L. M. Franco Arias, and A. Márquez, "Study of the structure of titanium thin films deposited with a vacuum arc as a function of the thickness," *Thin Solid Films*, vol. 593, pp. 110–115, Oct. 2015, doi: 10.1016/j.tsf.2015.09.015.
- [9] S. Banerjee and P. Mukhopadhyay, *Phase Transformations - Examples from Titanium and Zirconium Alloys*. 2007.

- [10] K. Hofmann, B. Spangenberg, M. Luysberg, and H. Kurz, "Properties of evaporated titanium thin films and their possible application in single electron devices," 2003.
- [11] C. O'mahony, M. Hill, P. J. Hughes, and W. A. Lane, "Titanium as a micromechanical material INSTITUTE OF PHYSICS PUBLISHING JOURNAL OF MICROMECHANICS AND MICROENGINEERING Titanium as a micromechanical material," 2002. [Online]. Available: <http://iopscience.iop.org/0960-1317/12/4/316>
- [12] F. E. Wawner and K. R. Lawless, "Epitaxial Growth of Titanium Thin Films," *Journal of Vacuum Science and Technology*, vol. 6, no. 4, pp. 588–590, Jul. 1969, doi: 10.1116/1.1315691.
- [13] S. Guadagnini, "Characterization of exotic crystal structures of titanium thin films through Brillouin spectroscopy Tesi di Laurea Magistrale in Engineering Physics-Ingegneria Fisica."
- [14] S. K. Kim, F. Jona, and P. M. Marcus, "Growth of face-centred-cubic titanium on aluminium," 1996.
- [15] Y. Sugawara, N. Shibata, S. Hara, and Y. Ikuhara, "Interface structure of face-centered-cubic-Ti thin film grown on 6H-SiC substrate," 2000.
- [16] D. Josell, D. Shechtman', and D. Van Heerden, "fee titanium in Ti/Ni multilayers," 1995.
- [17] D. Van Heerden', D. Josell', and D. Shechtman', "THE FORMATION OF F.C.C. TITANIUM IN TITANIUM-ALUMINUM MULTILAYERS," 1996.
- [18] J. Chakraborty, K. Kumar, R. Ranjan, S. G. Chowdhury, and S. R. Singh, "Thickness-dependent fcc-hcp phase transformation in polycrystalline titanium thin films," *Acta Mater*, vol. 59, no. 7, pp. 2615–2623, Apr. 2011, doi: 10.1016/j.actamat.2010.12.046.
- [19] A. S. Bolokang, M. J. Phasha, D. E. Motaung, F. R. Cummings, T. F. G. Muller, and C. J. Arendse, "Microstructure and phase transformation on milled and unmilled Ti induced by water quenching," *Mater Lett*, vol. 132, pp. 157–161, Oct. 2014, doi: 10.1016/j.matlet.2014.06.063.
- [20] C. Chen *et al.*, "The microstructure and formation mechanism of face-centered cubic Ti in commercial pure Ti foils during tensile deformation at room temperature," *Mater Charact*, vol. 136, pp. 257–263, Feb. 2018, doi: 10.1016/j.matchar.2017.12.031.
- [21] D. H. Hong, T. W. Lee, S. H. Lim, W. Y. Kim, and S. K. Hwang, "Stress-induced hexagonal close-packed to face-centered cubic phase transformation in commercial-purity titanium under cryogenic plane-strain compression," *Scr Mater*, vol. 69, no. 5, pp. 405–408, Sep. 2013, doi: 10.1016/j.scriptamat.2013.05.038.

- [22] J. X. Yang, H. L. Zhao, H. R. Gong, M. Song, and Q. Q. Ren, "Proposed mechanism of HCP  $\rightarrow$  FCC phase transition in titanium through first principles calculation and experiments," *Sci Rep*, vol. 8, no. 1, Dec. 2018, doi: 10.1038/s41598-018-20257-9.
- [23] L. Li, W. Jia, and V. Ji, "Phase transformations mechanism in commercially pure titanium subjected to multiple laser shock peening," *Surf Coat Technol*, vol. 450, Nov. 2022, doi: 10.1016/j.surfcoat.2022.129010.
- [24] I. Manna, P. P. Chattopadhyay, P. Nandi, F. Banhart, and H. J. Fecht, "Formation of face-centered-cubic titanium by mechanical attrition," *J Appl Phys*, vol. 93, no. 3, pp. 1520–1524, Feb. 2003, doi: 10.1063/1.1530718.
- [25] M. J. Phasha, A. S. Bolokang, and P. E. Ngoepe, "Solid-state transformation in nanocrystalline Ti induced by ball milling," *Mater Lett*, vol. 64, no. 10, pp. 1215–1218, May 2010, doi: 10.1016/j.matlet.2010.02.054.
- [26] V. L. Sliwko, P. Mohn, K. Schwarz, and P. Blaha, "The fcc-bcc structural transition: I. A band theoretical study for The fcc-bcc structural transition: I. A band theoretical study for Li, K, Rb, Ca, Sr, and the transition metals Ti and V," 1996. [Online]. Available: <http://iopscience.iop.org/0953-8984/8/7/006>
- [27] D. M. Tshwane, R. Modiba, and A. S. Bolokang, "Surface analysis of the stress-induced, impurity driven face centered cubic titanium phase and the ranging lattice parameter sizes," *Mater Today Commun*, vol. 24, Sep. 2020, doi: 10.1016/j.mtcomm.2020.101168.
- [28] P. Chatterjee and S. P. Sen Gupta, "An X-ray diffraction study of nanocrystalline titanium prepared by high-energy vibrational ball milling."
- [29] A. S. Bolokang, D. E. Motaung, C. J. Arendse, and T. F. G. Muller, "Formation of the metastable FCC phase by ball milling and annealing of titanium-stearic acid powder," *Advanced Powder Technology*, vol. 26, no. 2, pp. 632–639, Mar. 2015, doi: 10.1016/j.appt.2015.01.013.
- [30] P. E. Vullum, M. Pitt, J. Walmsley, B. Hauback, and R. Holmestad, "Observations of nanoscopic, face centered cubic Ti and TiH<sub>x</sub>," *Appl Phys A Mater Sci Process*, vol. 94, no. 4, pp. 787–793, 2009, doi: 10.1007/s00339-008-4929-9.
- [31] I. Manna, P. P. Chattopadhyay, P. Nandi, and P. M. G. Nambissan, "Positron lifetime studies of the hcp to fcc transformation induced by mechanical attrition of elemental titanium," *Physics Letters, Section A: General, Atomic and Solid State Physics*, vol. 328, no. 2–3, pp. 246–254, Jul. 2004, doi: 10.1016/j.physleta.2004.06.029.
- [32] L. Niu *et al.*, "Mechanical behavior and deformation mechanism of commercial pure titanium foils," *Materials Science and Engineering: A*, vol. 707, pp. 435–442, Nov. 2017, doi: 10.1016/j.msea.2017.09.080.

- [33] X. Zheng *et al.*, "Deformation induced FCC lamellae and their interaction in commercial pure Ti," *Scr Mater*, vol. 162, pp. 326–330, Mar. 2019, doi: 10.1016/j.scriptamat.2018.11.037.
- [34] H. Zhang, X. Ou, B. Wei, S. Ni, and M. Song, "Strain direction dependency of deformation mechanisms in an HCP-Ti crystalline by molecular dynamics simulations," *Comput Mater Sci*, vol. 172, Feb. 2020, doi: 10.1016/j.commatsci.2019.109328.
- [35] H. C. Wu *et al.*, "Rolling-induced face centered cubic titanium in hexagonal close packed titanium at room temperature," *Sci Rep*, vol. 6, Apr. 2016, doi: 10.1038/srep24370.
- [36] Z. Zhao, G. Zhu, Y. Kang, X. Li, and L. Peng, "The observation of the orthorhombic  $\alpha''$  and fcc titanium in deformed commercially pure titanium compressed at elevated temperature," *J Alloys Compd*, vol. 815, Jan. 2020, doi: 10.1016/j.jallcom.2019.152298.
- [37] Q. Yu *et al.*, "In situ TEM observation of FCC Ti formation at elevated temperatures," *Scr Mater*, vol. 140, pp. 9–12, Nov. 2017, doi: 10.1016/j.scriptamat.2017.06.033.
- [38] H. Shahmir and T. G. Langdon, "An evaluation of the hexagonal close-packed to face-centered cubic phase transformation in a Ti-6Al-4V alloy during high-pressure torsion," *Materials Science and Engineering: A*, vol. 704, pp. 212–217, Sep. 2017, doi: 10.1016/j.msea.2017.07.099.
- [39] Y. Chang *et al.*, "Could face-centered cubic titanium in cold-rolled commercially-pure titanium only be a Ti-hydride?," *Scr Mater*, vol. 178, pp. 39–43, Mar. 2020, doi: 10.1016/j.scriptamat.2019.11.010.
- [40] R. Traylor, R. Zhang, J. Kacher, J. O. Douglas, P. A. J. Bagot, and A. M. Minor, "Impurity and texture driven HCP-to-FCC transformations in Ti-X thin films during in situ TEM annealing and FIB milling," *Acta Mater*, vol. 184, pp. 199–210, Feb. 2020, doi: 10.1016/j.actamat.2019.11.047.
- [41] Harra D.J., "Predicting and Evaluating Titanium Sublimation Pump Performance," 1974.
- [42] G. I. Grigorov, "Apparent and real values of common gas sticking coefficients on titanium films and application to getter pump devices with periodic active film renovation."
- [43] G. I. Grigorov and K. K. Tzatzov, "Theory of getter pump evaluation. Sticking coefficients of common gases on continuously deposited getter films."
- [44] B. Singh *et al.*, "Thin solid films," 1974.

- [45] C. Benvenuti *et al.*, "A novel route to extreme vacua: the non-evaporable getter thin film coatings," 1999.
- [46] Georgii L. Saksaganskii, *Getter And Getter-Ion Vacuum Pumps*.
- [47] C. Benvenuti, P. Chiggiato, F. Cicoira, and Y. L'Aminot, "Nonevaporable getter films for ultrahigh vacuum applications," *Journal of Vacuum Science & Technology A: Vacuum, Surfaces, and Films*, vol. 16, no. 1, pp. 148–154, Jan. 1998, doi: 10.1116/1.580963.
- [48] J. Kamiya, K. Takano, H. Yuza, and K. Wada, "Evaluation of Titanium Vacuum Chamber as Getter Pump," *e-Journal of Surface Science and Nanotechnology*, vol. 20, no. 2, pp. 107–118, 2022, doi: 10.1380/ejssnt.2022-017.
- [49] J. Kamiya, K. Takano, and H. Yuza, "SOME METHODS OF MAKING TITANIUM VACUUM CHAMBER ACT AS GETTER PUMP FOR UHV/XHV," 2021, doi: 10.18429/JACoW-IPAC2021-WEPAB337.
- [50] W. T. Arkin, Casari Carlo, and Li Bassi Andrea, *Advances in laser and optics research. Volume 7*. Nova Science, 2012.
- [51] B. Roberta Bricchi Advisor, A. Li Bassi, C. S. Casari, and V. Dossena, "Engineering of titanium oxide and nitride nanostructures for plasmonic applications Tutor: The Chair of the Doctoral Program: Year 2020 Cycle XXXIII."
- [52] Robert Eason, *Pulsed Laser Deposition of Thin Films: Applications-Led Growth of Functional Materials*. 2007.
- [53] Ferrario Monforte Arianna, "Synthesis and Characterization of Manganese Oxides Thin Films."
- [54] C. R. Brundle, Charles A. Evans, and Shaun Wilson, *Encyclopedia of Materials Characterization: Surfaces, Interfaces, Thin Films*. 1992.
- [55] K. Akhtar, S. A. Khan, S. B. Khan, and A. M. Asiri, *Handbook of Materials Characterization*. 2018.
- [56] Surender Kumar Sharma, Ed., *Handbook of Materials Characterization*. Springer Cham.
- [57] A. Li Bassi Co-Supervisor and B. Roberta Bricchi, "Development of plasmonic gold nanostructures with tunable optical and electrical properties," 2018.
- [58] W. C. H. Kuo, M. Briceno, and D. Ozkaya, "Characterisation of catalysts using secondary and backscattered electron in-lens detectors," *Platin Met Rev*, vol. 58, no. 2, pp. 106–110, 2014, doi: 10.1595/147106714X680113.
- [59] O. Instruments NanoAnalysis, "Silicon Drift Detectors Explained."
- [60] A. Li Bassi, "Durham E-Theses X-ray and light scattering from nanostructured thin films." [Online]. Available: <http://etheses.dur.ac.uk>

- [61] Peter Brüesch, *Phonons: Theory and Experiments II: Experiments and Interpretation of Experimental Results*. 2012.
- [62] T. Matteo, A. Lucotti, and A. Macrelli, "Development of Paper-Based SERS Sensors for the Detection of Drugs," 2019.
- [63] S. Garattoni, "Synthesis of titanium nitride thin films with tunable optical and electrical properties," 2018.
- [64] P. Dutta, "Grazing incidence X-ray diffraction," 2000. [Online]. Available: <https://about.jstor.org/terms>
- [65] Chrisey Douglas and Hubler Graham, *Pulsed Laser Deposition of Thin Films*, 1st ed., vol. June 7, 1994. Wiley-Interscience, 1994.
- [66] J. J. Beltrano, L. Torrisi, A. M. Visco, N. Campo, and E. Rapisarda, "Pulsed Laser Deposition (PLD) Technique to Prepare Biocompatible Thin Films," in *Materials in Clinical Applications VII*, Trans Tech Publications Ltd, Oct. 2006, pp. 56–61. doi: 10.4028/www.scientific.net/ast.49.56.
- [67] O. Albert *et al.*, "Time-resolved spectroscopy measurements of a titanium plasma induced by nanosecond and femtosecond lasers," *Appl Phys A Mater Sci Process*, vol. 76, no. 3, pp. 319–323, Mar. 2003, doi: 10.1007/s00339-002-1815-8.
- [68] D. Dellasega, G. Merlo, C. Conti, C. E. Bottani, and M. Passoni, "Nanostructured and amorphous-like tungsten films grown by pulsed laser deposition," *J Appl Phys*, vol. 112, no. 8, Oct. 2012, doi: 10.1063/1.4761842.
- [69] R. W. G. Wyckoff, "Body centered cubic, bcc, structure," *Crystal Structures*, vol. 1, pp. 7–83, 1963.
- [70] J. Haglund, F. Fernandez Guillermet, G. Grimvall, and M. Korling, "Theory of bonding in transition-metal carbides and nitrides," *Physical Review, Serie 3. B - Condensed Matter (18,1978-)*.
- [71] R. W. G. Wyckoff, "Hexagonal closest packed, hcp, structure," *Crystal Structures*, vol. 1, pp. 7–83, 1963.
- [72] E. S. Chebotareva and S. G. Nuzhdina, "Observation of omega-titanium in a composite hard facing alloy based on fine-grain diamonds," *Fizika Metallov i Metallovedenie*, vol. 36, pp. 200–202, 1973.
- [73] K. Momma and F. Izumi, "VESTA: A three-dimensional visualization system for electronic and structural analysis," *J Appl Crystallogr*, vol. 41, no. 3, pp. 653–658, Apr. 2008, doi: 10.1107/S0021889808012016.
- [74] D. Nath, F. Singh, and R. Das, "X-ray diffraction analysis by Williamson-Hall, Halder-Wagner and size-strain plot methods of CdSe nanoparticles- a comparative study," *Mater Chem Phys*, vol. 239, Jan. 2020, doi: 10.1016/j.matchemphys.2019.122021.

- [75] B. R. Bricchi *et al.*, "Nanoporous Titanium (Oxy)nitride Films as Broadband Solar Absorbers," *ACS Appl Mater Interfaces*, vol. 14, no. 16, pp. 18453–18463, Apr. 2022, doi: 10.1021/acsami.2c01185.
- [76] B. R. Bricchi *et al.*, "Supporting Information Nanoporous titanium (oxy)nitride films as broadband solar absorbers."
- [77] P. di Milano, L. Mascaretti Supervisors, A. S. Li Bassi Carlo Casari Tutor, M. Passoni, and C. E. Bottani, "Hydrogen-treated titanium dioxide hierarchical nanostructures for water splitting applications The Chair of the Doctoral Programme: Year 2017-Cycle XXX."
- [78] Peter E. J. Flewitt and Robert K. Wild, *Physical Methods for Materials Characterisation Series in Materials Science and Engineering*.



## List of Figures

Figure 1.1: Titanium's (a) hcp $\alpha$ phase and (b) bcc $\beta$ phase. Highlighted the most densely packed planes and directions [1] .....	4
Figure 1.2: influence of alloying elements on phase diagrams [1] .....	5
Figure 1.3: experimentally determined temperature-pressure phase diagram for Ti[9]. .....	7
Figure 1.4: XRD spectra of titanium films deposited in (a) DCMS regime, (b)HiPIMS in the condition of 0V [7]. .....	9
Figure 1.5: XRD spectra of titanium, showing evolution of FCC and HCP phase with milling time [24]......	12
Figure 1.6: The sticking coefficient $s$ for $H_2$ on Ti as a function of relative concentration of incident particles $c$ [43]......	14
Figure 1.7: Initial sticking coefficient of following active gas as a function of the surface temperature $T_s$ [43]. .....	15
Figure 1.8: Roughness factor $R$ dependence on film thickness [42], [44] .....	15
Figure 1.9: Pressure drop according to the heating temperature and material used [47]. .....	17
Figure 1.10: diagram of the two methods for removing surface titanium oxide [48] .	18
Figure 1.11: comparison of sputtering, baking and turbomolecular pump performances in the reduction of pressure with time [49]. .....	19
Figure 2.1: experimental set-up for Pulsed Laser Deposition (PLD) experiments [53] .....	21
Figure 2.2: picture of the PLD used for this work thesis [77]......	22
Figure 2.3: SEM apparatus [53]......	26
Figure 2.4: Principle of SE signal detection[58] .....	27
Figure 2.5: Schematic representation of a Silicon Drift Detector [59] .....	28
Figure 2.6: Raman spectroscopy setup with the highlighting of the beam path [78].	30
Figure 2.7: stokes (left) and antistokes process (right) scheme [53] .....	30
Figure 2.8: Scheme of XRD in $\theta/2\theta$ configuration [53] .....	32

Figure 2.9: scheme of diffraction process[53] .....	32
Figure 2.10: furnace for annealing in vacuum.....	34
Figure 3.1: trend of pumping of turbomolecular pump when active. Variation of pressure and of the first derivative with time.....	37
Figure 3.2: Chamber pressure variation with time during ablation of the target at different background pressure. Trend fitted with allometric function. ....	38
Figure 3.3: First derivative of the chamber pressure variation with time during the ablation of target at different background pressure. ....	38
Figure 3.4: Comparison between the turbomolecular pumping curve and the "TSP" one at different background pressure. The pressure is plot in ln scale.....	40
Figure 3.5: comparison of turbomolecular pumping rate with the "TSP" at different fluences. ....	41
Figure 3.6: strategy to reduce the vacuum pressure exploiting the cleaning. ....	42
Figure 3.7: Thickness vs time fixed the fluence to 7.51J/cm <sup>2</sup> . The slope m is the deposition rate relative to the value of fluence adopted. ....	44
Figure 3.8: deposition rate vs fluence rate. It can be fitted with an almost linear behaviour (R <sup>2</sup> =0.93). The fluence rate results to be around 1.07 J/cm <sup>2</sup> .....	45
Figure 3.9: example of cross section thickness profile of our samples. ....	46
Figure 3.10: cross section of W films deposited in vacuum by PLD [68] .....	47
Figure 3.11: Cross section image. Morphology of our titanium film samples. The following film is 507nm thick. ....	47
Figure 3.12: Cross section of 2 μm titanium film by PLD.....	48
Figure 3.13: cross section morphology of Ti films by DCMS [7] .....	48
Figure 3.14: cross section morphology of Ti films in HiPIMS regime without an applied bias [7]. ....	49
Figure 3.15: Ti films by PLD plane view .....	49
Figure 3.16: Ti films by PLD plane view .....	49
Figure 3.17: atomic oxygen concentration in titanium films as a function of fluence, keeping fixed the value of deposition time and background pressure.....	51
Figure 3.18: atomic oxygen concentration in titanium films as a function of background pressure keeping fixed the value of fluence and deposition time. ....	51
Figure 3.19 atomic oxygen concentration in titanium films as a function of deposition time keeping fixed the value of fluence and background pressure.....	52

Figure 3.20: atomic oxygen concentration in titanium films as a function of deposition time without keeping fixed the value of fluence and background pressure.....	53
Figure 4.1: XRD of most significant spectra and comparison with HCP and FCC reference powder diffraction. The background pressure is not reported.....	55
Figure 4.2: mismatch between FCC reference powder and experimental peaks of our titanium films.....	56
Figure 4.3: Comparison of reference powder spectra of titanium FCC with lattice parameter of 4.264 Å (extracted from vesta [73]) and our sample. The number of the peaks are related to that of Table 4.1. ....	58
Figure 4.4: GIXRD spectra variation with thickness .....	60
Figure 4.5: effect of gas (1Pa of Ar) at high and low fluence with a deposition time fixed to 2000s.....	62
Figure 4.6: dimension of the cell variation with the influencing parameters in the two set of depositions (first and second). ....	64
Figure 4.7: fit of the main peak at 36.18° (Table 4.2) with the assumption of single peak fit.....	66
Figure 4.8: Williamson-Hall analysis for different samples at different conditions....	68
Figure 4.9: XRD in $\theta/2\theta$ of most significant samples. The black and red spectra have been analysed also in Figure 4.1 by GIXRD analysis. ....	69
Figure 4.10 XRD spectra in $\theta/2\theta$ that do not show evident FCC phase peaks. ....	70
Figure 4.11: Fraction of FCC phase in the film according to different Ti/O ratio. In red the upper limit proposed by [27] over which no FCC phase is expected .....	72
Figure 4.12: variation of the crystal structure according to the difference values of annealing temperature.....	74
Figure 4.13: Raman analysis of samples with different ratio of Ti/O. All the measurements are normalized to 1.....	75
Figure 4.14: magnification of Figure 4.13, highlighting the different behaviour of the oxidized sample respect the non-oxidized one.....	76
Figure 4.15: Raman spectra of oxynitride films deposited in vacuum and at 10–100 Pa of N <sub>2</sub> / H <sub>2</sub> . [75].....	77



## List of Tables

Table 1.1: properties of $\alpha$ , $\alpha+\beta$ , $\beta$ Ti alloys [1].	5
Table 1.2: values of the lattice parameter of FCC titanium [27]	11
Table 1.3: initial sticking coefficient for different active gas at room temperature[41], [42]	14
Table 1.4: Initial sticking coefficient for N <sub>2</sub> at T=300K and variation with thickness. [42]	16
Table 3.1: process condition of work thesis samples.	35
Table 3.2: different values of parameters of allometric functions	39
Table 3.3: Comparison of different performance of TSP at different background pressure, keeping fixed time to 33 minutes and fluence to 4J/cm <sup>2</sup> .	41
Table 3.4: comparison in term of time between the two.	42
Table 3.5: range of atomic concentration of elements (Ti, O) in the Ti film produced in vacuum	50
Table 4.1: computation of lattice cell for each peak of each sample.	57
Table 4.2: peaks and subpeaks assignment of red sample (437nm) of Figure 4.3. The same peaks and subpeaks assignment can be attributed to others sample with slight variations.	59
Table 4.3: scheme of the calculus of (x,y) to perform Williamson-Hall analysis.	67
Table 4.4: grains dimensions and cell dimensions of peaks obtained at different conditions.	73







## Acknowledgments

Ringrazio il professor David Dellasega per avermi dato la possibilità di lavorare a questo progetto, per aver seguito il mio percorso sempre con grande disponibilità, attenzione, entusiasmo ed interesse. Ringrazio il dottorando Andrea Macrelli per avermi seguito durante gli esperimenti, mostrando sempre massima disponibilità e pazienza illimitata a rispondere ad ogni mio dubbio e necessità. Ringrazio Alessio Lamperti per l'analisi delle misure XRD avute sempre con grandissima rapidità.

Intendo ringraziare infine la mia famiglia e tutti i miei amici per avermi sempre sostenuto nei momenti sia facili sia difficili.

